Development of a novel balloon-borne optical sonde for the measurement of ozone and other stratospheric trace gases

Entwicklung einer ballongestützten optischen Sonde zur Messung von Ozon und anderen stratosphärischen Spurengasen

---

Mareile Wolff

Ber. Polarforsch. Meeresforsch. xxx (2006)
ISSN 1618-3193

Dr. Mareile Wolff
Atmospheric Physics Group
Department of Physics
University of Toronto
60 St. George Street
Toronto, ON, Canada M5S 1A7

Die vorliegende Arbeit ist die inhaltlich unveränderte Fassung einer Dissertation, die im September 2005 dem Fachbereich 2 (Biologie/Chemie) der Universität Bremen vorgelegt wurde.

Eine elektronische Farbversion dieses Dokumentes kann bezogen werden unter:
http://nbn-resolving.de/urn:nbn:de:gbv:46-diss000101100

Contents

Abstract

In the frame of this work, a new small-size balloon-borne sonde was developed. A miniature grating spectrometer in the sonde measures simultaneously the solar spectral irradiance at a wide wavelength range from 200 to 850. As a first application, ozone profiles have been determined by measuring the changes in the spectral irradiance, caused by ozone absorption in the Huggins band. The wide spectral coverage of the spectrometer offers the possibility for measurements of other trace gases which absorb within the wavelength range, e.g. NO_2 and BrO. The low weight of the new sonde (1.7 kg), the moderate price, and the autonomous portable telemetry system makes it a very versatile tool for satellite validation and for case studies, which requires a high number of launches.

The newly developed sonde works well without temperature stabilisation, even so the spectrometer experiences rather large temperature changes (15 - 20 K) during the ascent through the atmosphere. Laboratory measurements were performed in order to quantify the temperature induced wavelength shift, the absolute irradiance changes, and the dark current behaviour. Based on the laboratory characterisation, inflight corrections could be applied, which compensate the effects of temperature changes.

The system was tested in twelve flights and continuously improved. A technical status could be achieved, which guarantees for reliable measurements.

For the retrieval of ozone profiles of the irradiance measurements, the analysis algorithm of the ground-based Dobson spectrometer was adapted. The determined ozone profiles were compared to ozone profiles measured by electrochemical sondes and LIDAR. The comparsion shows good agreement within 10% to 20% for altitudes above 15 km. For low solar zenith angles, reliable agreement with comparison measurements even at lower altitudes (8 and 15 km) were achieved. A quality criterion was developed, which allows the evaluation of the calculated ozone profile, independent from the comparison to other measurements.

Absorption structures due to NO_2 could be identified in the irradiance spectra measured at different altitudes (15 and 35 km). This demonstrated the feasibility of the new instrument to measure other trace gases beside ozone.

Zusammenfassung

Im Rahmen dieser Arbeit wurde eine kleine, optische Ballonsonde entwickelt. Mit einem Miniatur Spektrometer können gleichzeitig solare spektrale Bestrahlungsstärken auf einem Wellenlängenbereich von 200 bis 850 nm gemessen werden. In einer ersten Anwendung wurden aus den Messungen der Bestrahlungsstärken im UV, die sich aufgrund der Ozonabsorption im Hugginsband mit der Höhe ändern, Ozonprofile bestimmt. Der weite Spektralbereich des Spektrometers bietet die Möglichkeit, auch andere Spurengase, die in diesem Bereich absorbieren (z.B. NO_2 and BrO) zu messen.

Durch das geringe Gewicht der neuen Sonde (1.7 kg), einem moderaten Stückpreis und einem unabhängigen tragbaren Telemetrie-System ist die neue Sonde ein vielseitiges Instrument. Es bietet sich an zur Satellitenvalidation und für den Einsatz bei Fallstudien, die eine hohe Anzahl von Aufstiegen erfordern.

Die neue Sonde funktioniert einwandfrei ohne eine aktive Stabilisierung der Temperatur, obwohl das Spektrometer während des Ballonaufstieges relativ großen Temperaturänderungen (15 - 20 K) ausgesetzt wird. In Labormessungen wurde der Einfluss von Temperaturänderungen auf das Spektrometer untersucht: Temperaturabnahme verursacht eine Zunahme des Dunkelstroms, eine Verschiebung der Wellenlängenzuordnung der Spektrometerkanäle und eine Abnahme des gemessenen Signals einer unveränderten Lichtquelle. Es wurden Methoden entwickelt, um diese Effekte während des Aufstiegs zu korrigieren.

Das neue System wurde in zwölf Flügen getestet und kontinuierlich verbessert. Der erreichte technische Status der neuen Sonde garantiert zuverlässige Messungen.

Die Methode für die Berechnung von vertikalen Ozonsäulen aus Wellenlängenmessungen des Dobson Spektrometers wurde für die Auswertung der Messungen der neuen Sonde angepaßt. Mit dem Algorithmus wurden aus den spektralen Bestrahlungsstärken Ozonprofile abgeleitet. Der Vergleich der Ozonprofile mit Ozonprofilen, die mit elektrochemischen Sonden gemessen wurden, zeigte eine gute Übereinstimmung von 10% bis 20% in Höhen über 15 km. Für die Messungen, die während großer Sonnenzenitwinkel durchgeführt wurden, konnten Ozonprofile berechnet werden, die schon ab etwa 8 km eine verlässliche Übereinstimmung mit den Ozonprofilen der elektrochemischen Sonden zeigten. Ein Qualitätskriterium wurde entwickelt, dass die Beurteilung der berechneten Ozonprofile unabhängig von weiteren Vergleichsmessungen erlaubt.

Absorptionsstrukturen von NO_2 konnten in den gemessen Spektren aus zwei verschiedenen Höhen (15 und 35 km) identifiziert werden. Das demonstriert die Möglichkeit der neuen Sonde, neben Ozon auch weitere Spurengase messen zu können.

Chapter 1

Introduction

After the discovery of the springtime Antarctic ozone hole in the 1980s, two decades of intensified atmospheric monitoring and basic research in atmospheric chemistry and physics followed. And an enormous progress in our understanding of the impact of human activities on the chemistry and physics of the global stratosphere has been achieved in the meantime.

In the recent *Scientific Assessment of Ozone Depletion* (WMO 2003) the actual scientific knowledge has been summarised. It is stated that the chloroflourocarbons and other stable halogen compounds have been the main cause of the past stratospheric ozone depletion. The stratospheric concentrations of these compounds were increasing until recently due to anthropogenic activities as well as their long life time. The production of most of the known ozone depleting compounds was banned by the Montreal protocol 1987. Therefore, their stratospheric burden is expected and partly began to decrease. Accordingly, the stratospheric ozone concentration is expected to return to the 1980 values in the next decades. Analysis of ground-based and satellite ozone measurements (e.g. REINSEL et al. (2005) and FIOLETOV et al. (2002)) already show a sligthly smaller global ozone depletion during the past few years. The significance of this trend is the topic of an ongoing scientific discussion (ZEREFOS 2004), (FIOLETOV 2004), and (WEATHERHEAD et al. 2004). It may be the beginning of the expected ozone recovery. However, the observation series also emphasise the raising influence of climate change on the future development of the ozone concentration (WMO 2003). The coupling processes between climate change and the future ozone development are complicated by feedback processes that are currently not sufficiently understood. This impacts the possibility of making reliable predictions for the future (IPCC (2001) and EUROPEAN COMMISSION (2003)). Some of the current key topics are:

- The increasing amount of greenhouse gases causes a warming of the troposphere and a cooling of the stratosphere. The latter enhances the effectivity of the heterogeneous chemical ozone depletion in the polar regions (e.g. PITARI et al. (2002)). The additional ozone loss due to stratospheric cooling was recently quantified by REX et al. (2004). It is larger than previously calculated. The severe ozone loss caused by the record low temperatures in the arctic stratosphere during spring 2005 supports that a strong relation exists between the stratospheric temperatures at the altitude of the ozone layer and ozone depletion (SCOUT PROJECT OFFICE 2005). However, further investigations are needed to develop a theoretical understanding of this relation (REX et al. 2004).

- Temperature changes may lead to changes in the stratospheric circulation and transport processes and thus affecting the global ozone distribution. At present it is not possible to predict these changes and the size of this effect on the ozone concentration (WMO 2003).
- The future trends of trace gases such as N_2O, CH_4, and H_2O will have an important impact on future stratospheric ozone amounts. These compounds are sources for NO_x and HO_x, which are involved in catalytical reaction cycles controlling the production and destruction of ozone (SIORIS et al. (2003); STENKE and GREWE (2005)). For a reliable determination of the trends, measurements of other trace gases than ozone in the stratosphere are indispensable.

The continuation and extent of ozone and other trace gas measurements with global coverage and good time resolution is necessary in order to observe the future development of the stratospheric ozone layer. First signs of ozone recovery are expected to occur in the upper stratosphere, in about 40 km altitude (SINGH and FABIAN 2003). Consequently, precise ozone measurements with high vertical resolution in this altitude range are important. Furthermore, detailed case studies of specific situations will help to complete and confirm the understanding of the chemical and dynamical processes controlling the stratospheric ozone chemistry. Various systems for ozone and other trace gas measurements already exist.

- The global distribution of ozone and other relevant atmospheric trace gases are monitored by remote sensing instruments aboard satellites, like GOME and SCIAMACHY on ENVISAT (e.g. BERTAUX et al. (2004) and ROHEN et al. (2005)) or TOMS operated on various spacecraft, which provides measurements of column ozone since 1978.
- With ground-based instruments detailled measurements of local situations with a high temporal resolution can be performed. Such local measurements are coordinated in global networks (e.g. the Network for Detection of Stratospheric Change: NDSC), which cover a wide latitudinal range.
- Validations campaigns for space borne sensors are performed from international starting sites with stratospheric balloons, rockets, and aircrafts equipped with highly sophisticated optical instruments for trace gas measurements (WURSTEISEN 2003).

- For routine ozone profile measurements a simple and less expensive measurement system is well established: the electrochemical (ECC) balloon-borne ozone sonde. About 20 ECC-sondes per week are launched worldwide, measuring in situ the local vertical ozone profile up to altitudes of about 30 km.

The global monitoring of changes in the ozone concentration is provided excellently by instruments on satellites and at ground based measurement stations. These instruments need regular validations for all their data products. Furthermore, the understanding of the future ozone development will also need flexible measurement methods for ozone and other trace gases suitable for case studies of phenomena, which demand measurements over a longer period or in an extended area.
There are the ECC-sondes, which offer a cheap and simple method for measuring reliable ozone profiles up to 30 km altitude. However, highly accurate and synchronously measurements of ozone and other trace gases can only be performed by optical sensors carried by large size balloons. Due to the necessary elaborate logistics, these experiments are very expensive and thus very limited in number. An instrument combining the advantages of both systems was so far missing:

> an air-borne sonde, which can measure simultaneously different trace gases by means of an optical method, allowing measurements from the ground up to the upper stratosphere. Especially in this altitude range reliable measurements are very important for satellite validation, but they are still very sparse. The sonde should be easy to use and independent from specially equipped launching sites or additional instrumentation. The costs for such a sensor should be moderate, which would allow for case studies, which require a higher number of launches.

1.1 Aims of this work

The main goal of this work was the development of a new balloon-borne sonde which fills the gap between the existing balloon borne methods. The more detailed aims of this study are:

Technical objectives:

- Conceptual design of a balloon borne sonde for trace gas measurements using a miniature optical spectrometer

- Technical realisation of the sonde regarding the demand of high versatility:
    - small size
    - low weight

  - easy to use
  - moderate price
  - modular concept of the soft- and hardware

- Performing measurements with the sonde in order to demonstrate the reliability of the system

Scientific objectives:

- Optical characterisation of the sonde, considering the conditions during a balloon ascent
- Development of a retrieval algorithm for ozone number density profiles
- Application of the retrieval algorithm and calculation of ozone number density profiles
- Comparison of the obtained ozone profiles with independent measuring systems

1.2 Synopsis

Chapter 2 deals with the basics of stratospheric chemistry. It focuses on ozone, which plays an important role in the global climate system and prevents the harmful ultraviolett (UV) radiation from reaching the Earth's surface. An overview of the complex interactions between stratospheric chemistry and the climate system is given and current questions are outlined.

In chapter 3 the most common measurement systems for ozone and other trace gases are described. The description of the optical methods for trace gas measurements includes an introcuction into the basic equations for trace gas retrieval using radiation measurements. As an example for a non optical method the common electrochemical ozone sonde is described.

The newly developed sonde is presented in chapter 4. The used components are detailed, followed by an overview of the complete sensor design. The procedure for a launch of the new sonde is also described.

In chapter 5 the optical sensor of the sonde, a miniature grating spectrometer, is characterised. The main aspect is the behaviour of this sensor under the difficult thermal conditions of an ascent through the atmosphere. The developed inflight correction methods regarding the effect of the changing temperature of the spectrometer are presented.

A short overview about the three campaigns and their locations are given in chapter 6. The technical aspects of each campaign and the subsequent continuous optimisation of the new sonde are described, resulting in a discussion of the present technical state of the sonde.

In chapter 7 the computing algorithm for the retrieval of ozone profiles is described. The vertical resolution of the obtained profiles is derived from the measurements, which allows an evaluation of the quality of the calculated profiles.
In chapter 8 results of the measurement campaigns are presented. The radiation changes detected during an ascent through the atmosphere are shown. Ozone profiles are calculated for 9 flights and are compared to other ozone measurements. Also, the applicability of the sonde for measurements of other trace gases is discussed.
Chapter 9 assesses the objectives of this work by summarising the findings and results. Finally, conclusive remarks and suggestions for possible future research are given.

Chapter 2

Stratospheric chemistry in the climate system

One of the most important chemical species in the stratosphere is ozone (O_3), because it absorbs ultraviolet (UV) solar radiation. Therefore it protects human beings, animals, and plants from exposure to harmful radiation Dessler (2000). Ozone was discovered by C. F. Schönbein in 1839 and was named after the greek word ozein (to smell) because of its pungent smell, (Schmidt 1988). Observations of the solar UV spectrum in 1920 led to the discovery of ozone in the atmosphere. The absolute amount of ozone is not very high. If one could collect all stratospheric and tropospheric ozone molecules and uniformly distribute them as a surface gas layer around the globe, the resulting layer would be about 0.3 centimeter thick under standard pressure and temperature Seinfeld and Pandis (1998).

Beginning with the discovery of the ozone hole in the 1980s, two decades with intense ozone research began. This has improved the understanding of chemical processes in the atmosphere enormously. Today, the main processes of the past ozone destruction are well understood. The Montreal protocol, which bans the ozone depleting substances, shows its success by a beginning decrease in the atmospheric concentration of the banned halogen compounds Solomon (2004).

It is under current scientific discussion whether the identified decrease of the ozone depletion during the last seven years is a signal for a beginning ozone recovery, or if it is just a non significant variation (Reinsel et al. 2005) and (Fioletov 2004). No doubt exists, however, about the fact, that the climate change will have an effect on the future ozone development and may rather slow down the expected recovery annd vice versa, also the changes in the stratospheric ozone are expected to influence the climate IPCC (2001).

In this chapter an introduction to today's knowledge on stratospheric chemistry, focussing on its most important compound ozone is given. The Montreal protocol and its effects are discussed, followed by a description of the actual ozone situation. The chapter will end with an outlook on the expected development of the stratospheric ozone concentration under a changing climate. The role of stratospheric chemistry in the complex climate system is yet not totally understood, which gives a motivation for the necessity of ongoing measurement activities.

2.1 Stratospheric ozone chemistry

In this section today's knowledge about the past changes in the ozone layer is summarised. The fundamental chemical reactions are presented and the main processes of ozone destruction are explained, regarding the special aspects of the polar regions. Finally, the Montreal protocol, which internationally regulates the ban of the main ozone depleting substances, is described.

2.1.1 Vertical structure of the atmosphere

The atmosphere can be divided into different layers (spheres), based on the variations in the average temperature profile with altitude (see Figure 2.1.1). The borders between the spheres are called pause, (e.g. SEINFELD and PANDIS (1998)). The troposphere is the lowest layer, extending from the Earth's surface to an altitude of about 8 km in the polar regions and to about 15 km in the tropics. It is characterised by a decreasing temperature with altitude, high turbulence, and rapid vertical mixing processes. The average lapse rate in the troposphere is 6.5 K km^{-1}. The temperature decrease is primarily due to the fact that the troposphere is heated from the Earth's surface. The troposphere contains about 90% of the total mass of the atmosphere. Because of the strong vertical mixing, an air parcel can be vertically transported through the entire troposphere in less than a day. The troposphere is the layer where cloud formation and precipitation takes place. The water content of the troposphere is characterised by high variability in space and time, depending on the local climate and the actual weather situation. The tropopause is the top of the troposphere. The thermal tropopause is defined as the lowest level at which the temperature lapse rate decreases to 2 K km^{-1} and remains at or below that rate for the next 2 km, WMO (1957). Another definition of the tropopause uses the abrupt change in the ozone concentration with altitude, WMO (1986) and BETHAN et al. (1996).

The layer above is referred to as the stratosphere, located between the tropopause (8 - 15 km) and the stratopause in about 50 km. Within the first kilometers of the stratosphere the temperature remains constant with altitude and then increases to a temperature of about 0° C at the stratopause. This vertical increase of temperature is caused by ozone, which absorbs solar ultraviolet radiation. About 90% of the total atmospheric ozone is located in the so called ozone layer in the stratosphere. In contrast to the well mixed troposphere, the thermal conditions lead to a static stability throughout the stratosphere, which prevents any strong vertical motion. The time for air parcels to circulate through the stratosphere amounts to several months on average. In contrast to the troposphere, the water content in the stratosphere is very low.

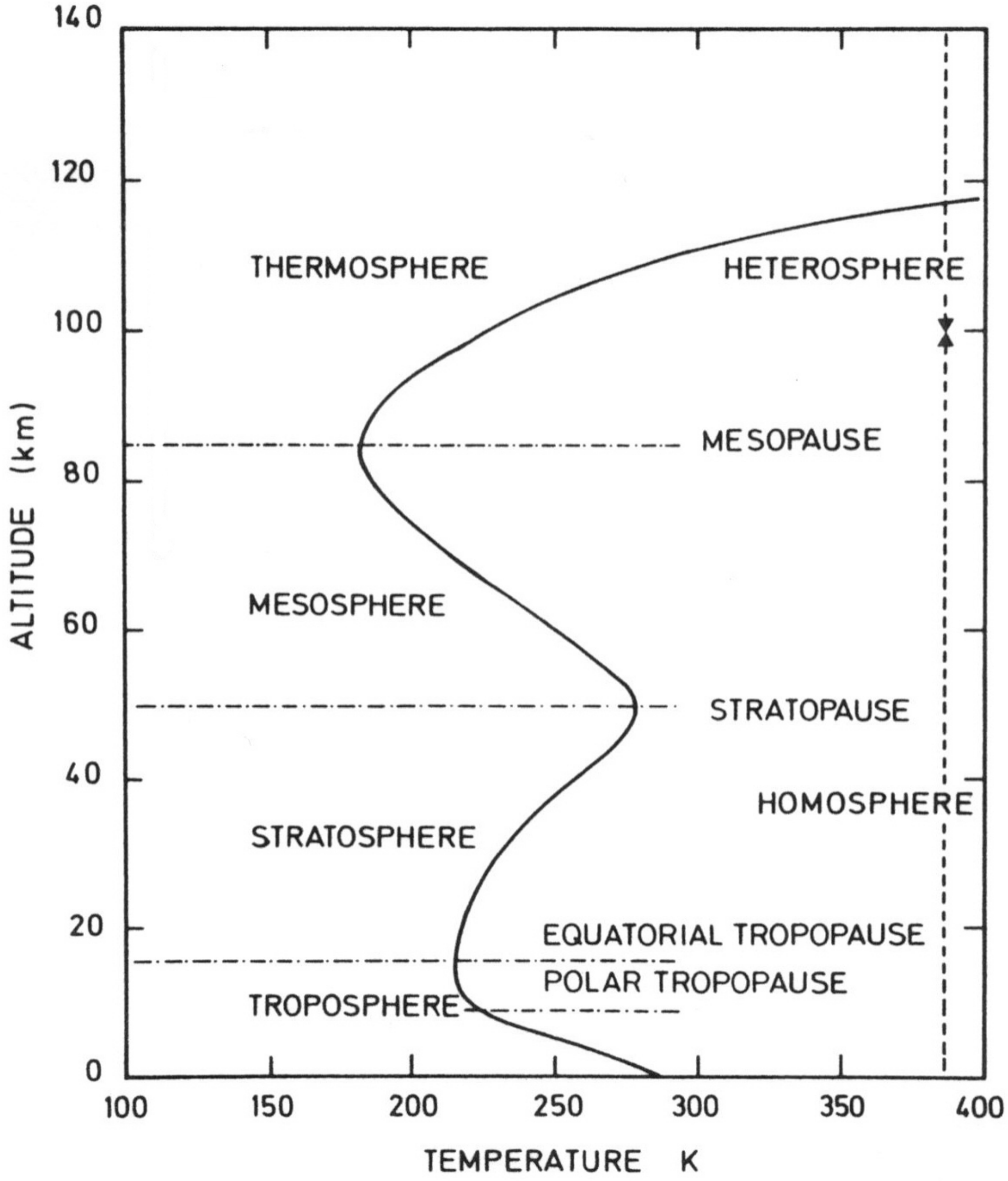

Figure 2.1: Mean vertical temperature profile of the atmosphere. Based on the variations in the average temperature profile the atmsophere is divided into different spheres: troposphere, stratosphere, mesosphere and thermosphere. Within the homosphere, the molecular weight of air varies little with altitude. In the heteorosphere the molecular weight changes with altitude primarily due to photodissociation of the major air constituents oxygen and nitrogen. After Brasseur and Solomon (1986)

The mesosphere extends from the stratopause at about 50 km to the mesopause between 80 and 90 km altitude. Within the mesosphere the temperature decreases again with altitude and the mesopause is the coldest point in the atmosphere.
Above the mesopause, in the thermosphere, the absorption of short wavelength radiation by atmospheric molecules, such as nitrogen (N_2) and oxygen (O_2) leads again to increasing temperatures.
Throughout the lower three layers (troposphere, stratosphere, and mesosphere) the major constituents of air are nitrogen and oxygen, with about 78% and 21% of the total number density, respectively. The mean molecular weight of air varies little with altitude. Therefore these three layers are referred to as the homosphere. Above the homosphere, the mean molecular weight of air varies with altitude and is called the heteorosphere. In this layer the abundances of nitrogen and oxygen decrease with height as a result of rapid photodissociation, while the abundance of atomic oxygen increases.
At about 500 km altitude, molecules can escape the Earth's gravitational force. The region where atoms and molecules shoot off into space is referred to as the exosphere, which represents the upper limit of our atmosphere.

2.1.2 Ozone chemistry

In this section the fundamental chemical reactions for producing and consuming the stratospheric ozone are presented.

The Chapman mechanism

The current understanding of stratospheric ozone (e.g. Solomon (1999)) is based on the theoretical concept of Chapman (1930). The following four reactions (illustrated in Figure 2.2) describe the production and comsumption of ozone in the stratosphere:

1. Molecular oxygen (O_2) is photolysed in the stratosphere (Reaction 2.1). To break up the $O = O$ bond of an oxygen molecule, a bond energy of $498\,\mathrm{kJmol^{-1}}$ is needed. The energy of a photon amounts to $E = \mathrm{h}\nu$, where $\mathrm{h}=6.6256\cdot10^{-34}$ Js is Planck's constant and ν is the frequency of the photon. Shortwave UV radiation with a wavelength of $\lambda \leq 240$ nm is sufficient to break the $O = O$ bond.

$$\mathrm{O_2 + h\nu \rightarrow 2\ \ O\bullet} \tag{2.1}$$

2. The produced oxygen radicals are highly reactive due to their 2 unpaired electrons and react in the presence of a third body M with an oxygen molecule to form ozone, see Reaction 2.2:

$$\mathrm{\bullet O + O_2 + M \rightarrow O_3 + M} \tag{2.2}$$

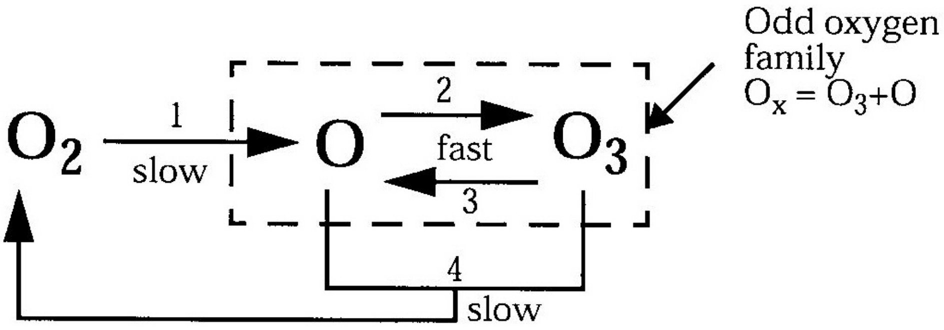

Figure 2.2: Scheme of the Chapman mechansim. The dashed line frames the rapid cycling reactions (2 and 3) between atomic oxygen and ozone, referred to as odd oxygen. The slower production and consumption of odd oxygen are marked with 1 and 4.

3. Ozone can be photolysed by solar radiation as well (Reaction 2.3):

$$O_3 + h\nu \rightarrow O_2 + O\bullet \tag{2.3}$$

4. A part of the atomic oxygen will react with an ozone molecule to form molecular oxygen (Reaction 2.4):

$$O_3 + O\bullet \rightarrow 2\ O_2\,. \tag{2.4}$$

Another part of the atomic oxygen produced in Reaction 2.3 will react with molecular oxygen to an ozone molecule, according to Reaction 2.2.
The two Reactions 2.2 and 2.3 are very fast reactions, thus describing the cycling between ozone and atomic oxygen. They are often referred to as the chemical family of odd oxygen $O_x = O + O_3$. The production (Reaction 2.1) and consumption (Reaction 2.4) of odd oxygen happens more slowly. The Chapman mechanism is illustrated in Figure 2.2, after Jacob (1999).
Assuming only the Chapman mechanism for the production and consumption of ozone, the resulting vertical ozone distribution shows the right altitude and extension of the ozone maximum, but overestimates the total amount of ozone by a factor of 2 (Jacob 1999).

Catalytical loss cycles

After the fundamental work of Chapman (1930), additional reactions contributing to the destruction of ozone were found later in the 20th century. They are referred to as catalytical loss cycles, because they are consuming ozone, while the initialising molecule is conserved. In this way a large number of ozone molecules can be destroyed by a single initialising molecule cycling through the destroying reactions until a termination process transforms the initialising molecule into a less reactive form. The catalytical loss cycles, and their termination processes are listed in Table 2.1.

Bates and Nicolet (1950) describe the HO_x-cycle, initiated by the production of hydroxyl radicals (OH) from water vapor in the stratosphere $H_2O + O \rightarrow 2OH$. Water in the stratosphere is either transported from the troposphere or produced by the oxidation of methane (CH_4) in the stratosphere. The hydroxyl radical and HO_2 are commonly referred to as the HO_x chemical family.

Crutzen (1970) presented the catalytical loss cycle based on a reaction with nitrogen oxide. The source for stratospheric NO_x is nitrous oxide (N_2O). Natural sources for N_2O in the troposphere are the oceans and tropical soils. Anthropogenic sources, which are smaller than the natural sources, are biomass burning and chemical industry. Since nitrous oxide has no significant sinks in the troposphere it can be transported into the stratosphere.

During daytime a part of the nitrogen dioxide (NO_2), produced in the first reaction of the NO_x-cycle is photolysed to nitrogen oxide (NO) and atomic oxygen (O). The oxygen radical reacts with molecular oxygen (O_2) to ozone. This alternative reaction chain is called a null cycle, because no effective ozone loss takes place.

The NO_x-cycle is terminated during day time through the oxidation of nitrogen dioxide by the hydroxyl radical to nitric acid (HNO_3). During nighttime, when the hydroxyl radical OH is absent, nitrogen dioxide is oxidised by ozone to form the nitrate radical (NO_3), which is subsequently converted into dinitrogen pentoxide (N_2O_5). Both products of the NO_x termination reactions, $HNO_3$and N_2O_5, are non-radicals and have long lifetimes in the stratosphere. Since they are eventually converted back into active NO_x, they act as reservoir gases.

These three processes, the Chapman mechanism and the catalytical loss cycles of HO_x and NO_x described the atmospheric ozone distribution prior 1970 sufficiently. Before the first signals of an ozone depletion were measured Molina and Rowland (1974) pointed out the ozone depleting potential of chlorine with a further catalytical loss cycle. As a source for chlorine in the atmosphere the raising amount of anthropogenically produced chloroflourocarbons (CFCs) were identified. CFCs are inert in the troposphere, because of their extremely low solubility in water, and their low reactivity towards other atmospheric chemicals. Therefore, CFCs have long life-times in the troposhere, where they are well mixed. A fraction finally crosses the tropopause and is spread out in the entire stratosphere by the mean stratospheric transport. UV radiation in the stratosphere photolyses the CFCs and chlorine is released.

The Cl_x cycle mainly occurs in the upper stratosphere, because the concentration of atomic oxygen increases with height (Brasseur and Solomon 1986).

A second chlorine cycle, which does not depend on atomic oxygen, was presented by Molina and Molina (1987). This cycle is named Cl_x-dimer-cycle in Table 2.1, because the dimer Cl_2O_2 is produced. It is also temperature-dependent, because the Cl_2O_2 dissociates easier into two ClO with higher ambient temperatures.

Both Cl_x cycles are terminated by the conversion of chlorine and chlorine monoxide (ClO) to non-radical chlorine reservoirs like hydrogen chloride (HCl) and chlorine nitrate ($ClNO_3$).

The ozone depleting potential of the chlorine molecules depends on the partioning between the chlorine available from active ClO_x and the chlorine existing in the non-reactive reservoirs HCl and $ClNO_3$.

The fifth ozone depleting cycle is initialised by bromine radicals (Br). Halons are strong sources for bromide radicals in the stratosphere. Similar to the CFCs halons are inert in the troposphere and photolyse in the stratosphere, releasing $Br\bullet$ radicals.

The $O - Br$ bond in $BrNO_3$ is weaker than the $O - Cl$ bond in $ClNO_3$. $BrNO_3$ photolyses and reacts rapidly with a hydroxyl radical and the amount of bromine tied up in inactive reservoir gases is very low. Therefore bromine is a very effective ozone depleting gas. Nevertheless, bromine does not dominate the ozone destruction process, since its stratospheric abundance is about 200 times smaller than that of chlorine (e.g. Wamsley et al. (1998)).

Heterogeneous chemistry

The described gas phase theory predicts that the strongest impact of chlorine on ozone occurs in the upper stratosphere near an altitude of 40 km. The ozone depletion was expected to be a gradual process. Therefore, the discovery of the extreme Antarctic ozone loss in the maximum of the ozone layer at abot 20 km by Chubachi (1984) and Farman et al. (1985), the ozone hole, was surprising.

The occurance of polar stratospheric clouds (PSCs), as well as observations of very high ClO-concentrations in the region of the maximum ozone loss, affirmed the assumption that heterogeneous processes on aerosol-surfaces lead to the activation of reactive chlorine (e.g. De Zafra et al. (1987) and Anderson et al. (1989)).

A layer of liquid aerosols exists at all latitudes between the tropopause and 30 km altitude. The aerosols are principially composed of sulfuric acid (H_2SO_4) and water. The layer is referred to as Junge layer (e.g. Junge et al. (1961) and Carslaw et al. (1997)).

The sulfuric acid in the stratosphere originates from the chemical transformation of tropospheric sulfur-containing compounds such as carbonyl sulfide, which is emitted from the oceans, and sulfur dioxide, which is produced for example emitted in large amounts during volcanic eruptions.

On the surface of the sulfuric acid aerosol, heterogeneous reactions can occur, which influence the ozone chemistry. These reactions are enhanced after the reload of the Junge-layer by a volcanic eruption, but occur also under background conditions.

Two reactions take place:

1. The aerosol surfaces support chemical reactions leading to the formation of active chlorine ClO_x

catalytical loss cycles	net reaction	termination
HO$_x$-cycle $OH + O_3 \rightarrow HO_2 + O_2$ $HO_2 + O_3 \rightarrow OH + 2O_2$	$2O_3 \rightarrow 3O_2$	$OH + HO_2 \rightarrow H_2O + O_2$
NO$_x$-cycle $NO + O_3 \rightarrow NO_2 + O_2$ $NO_2 + O \rightarrow NO + O_2$	$O_3 + O \rightarrow 2O_2$	D: $NO_2 + OH + M \rightarrow HNO_3 + M$ N: $NO_2 + O_3 \rightarrow NO_3 + O_2$ $NO_3 + NO_2 + M \rightarrow N_2O_5 + M$
Cl$_x$-cycle $Cl + O_3 \rightarrow ClO + O_2$ $ClO + O \rightarrow Cl + O_2$	$O_3 + O \rightarrow 2O_2$	$Cl + CH_4 \rightarrow HCl + CH_3$ $ClO + NO_2 + M \rightarrow ClNO_3 + M$
Cl$_x$-dimer-cycle $2 * (Cl + O_3 \rightarrow ClO + O_2)$ $ClO + ClO + M \rightarrow Cl_2O_2 + M$ $Cl_2O_2 + h\nu \rightarrow 2Cl + O_2$	$2O_3 \rightarrow 3O_2$	see Cl$_x$-cycle
Br$_x$-cycle $Br + O_3 \rightarrow BrO + O_2$ $Cl + O_3 \rightarrow ClO + O_2$ $BrO + ClO \rightarrow Br + Cl + O_2$	$2O_3 \rightarrow 3O_2$	$BrO + NO_2 \rightarrow BrNO_3$ $Br + CH_4 \rightarrow HBr + CH_3$

Table 2.1: Catalytical ozone loss reactions, their net ozone destruction and termination processes.

2. N_2O_5 can hydrolyse at the sulfuric acid water aerosols, thus reducing the NO$_x$ abundance. That process is referred to as denitrification.

On one hand, the denitrification reduces the ozone loss by the catalytical NO-cycle. On the other hand, it dramatically enhances the effect of the Cl$_x$- and Br$_x$-cycle, because the transformation of active chlorine into the reservoir gas $ClNO_3$ is decreased by the lack of NO_2, as described in the second termination reaction of the Cl$_x$-cycle. The related reaction converting bromine oxide into the reservoir gas $BrNO_2$ is also reduced.
The production rate of activated chlorine at the aerosol surfaces is strongly enhanced at low temperatures. Therefore, it is a major effect in the high-latitudes as described below. It may also occur in the mid-latitudes in regions with locally increased water content and at low temperatures under background aerosol conditions. In situations with high aerosol loading resulting from a volcanic eruption, the chlorine activation in mid-latitudes is enhanced, Keim (1996). It is not clear,

however, how often such situations occur and how large the total effect on ozone is.

Beside the background aerosol load of the Junge-layer, polar stratospheric clouds (PSC) are formed in polar regions during the winter seasons. At the surfaces of the PSC-particles the above described processes, chlorine activation and denitrifaction, are dramatically enhanced.

Three different types of PSCs are defined, depending on the type of particles of which they form:

1. Stratospheric ice clouds form when the temperature drops below the freezing point of water, which is at 191 K for a typical water partial pressure of $4{\cdot}10^{-4}$ hPa between 15 and 20 km altitude. These clouds are referred to as type 2 PSCs and are optically thick and brilliant in colour.
2. Above the frost point temperature, type 1 PSCs can form. Type 1a PSCs consist of solid particles of nitric acid trihydrate $HNO_3 \cdot 3H_2O$ (NAT).
3. Type 1b PSCs contain liquid particles of water (H_2O), nitric acid (HNO_3), and sulfuric acid (H_2SO_4).

The chlorine activation on the solid water-ice particles of type 2 PSCs is highly effective. Laboratory studies have demonstrated that also the type 1a and type 1b PSC particles are also very effective for activating chlorine, showing different efficiencies and different dependencies on temperature, water vapor abundance, and pressure (Carslaw et al. 1997).

2.1.3 The main ozone depletion processes

In this section, it will be focused on the processes and conditions which led to the observed ozone loss of the last twenty years. With the chemical reactions of the previous section in mind, the different regional aspects will be explained:

- The enormous ozone loss in Antarctica: the ozone hole
- The complex dynamical situation and the ozone loss in the Arctic
- The ozone loss in mid-latitudes.

Antarctica

The most dramatic ozone losses have occurred over Antarctica. The unusual low spring-time ozone values over Antarctica were observed and described for the first time by Farman et al. (1985) (British station Halley Bay) and Chubachi (1984) (Japanese station Syowa) in the 1980s of the last century. Satellite measurements showed that the area with extreme low ozone values extended over roughly the entire continent (Stolarski et al. 1986).

For the yearly observed springtime ozone loss above Antarctica, the term *ozone hole* became popular. It is defined as the area whith total ozone columns below 220 DU, (WMO 2003).

The absence of solar illumination during the dark winter period leads to a cooling over Antarctica and a large temperature gradient near the polar terminator. This temperature gradient drives a strong westerly wind around the polar area: the polar vortex. This very stable circular flow exists during winter between 12 km and 20 km altitude in the stratosphere. It seperates the air inside the vortex from the air of the surrounding mid-latitude regions. Therefore, the winter cooling is not disturbed by mixing with warmer air masses. Temperatures below the PSC threshold values are reached.

PSCs of type I and type II can develop. On their surfaces the transformation of chlorine from the reservoir gases (HCl and $ClONO_2$) to reactive species Cl_2 and HOCl starts. In spring when the sun returns, Cl_2 and HOCl are photolysed and the chlorine radicals start the ozone depletion following the catalytical loss cycles as described in section 2.1.2. In addition, denitrification of the stratosphere through the reaction of HNO_3 on the PSC surfaces enhances the ozone depletion process.

The Arctic

During the dark winter period a polar vortex is formed above the Arctic as well. The almost opposite continent-ocean distribution in the northern high latitudes compared to the Antarctic region causes a more disturbed polar vortex. As in Antarctica the stratospheric temperatures cool down in the dark winter period, but warmer air from the mid latitudes can still be mixed into the polar air masses, thus preventing the very low temperatures as observed in the Antarctic polar vortex. The more complicated dynamic situation with interannual differences made it difficult to detect and quantify the long-term Arctic ozone depletion.

With the Match campaign coordinated by the Alfred Wegener Institute for polar and marine research (REX et al. (1998) and SCHULZ et al. (2001)), the Arctic ozone destruction could be described and a better understanding of the major mechanisms was gained. During the campaigns air parcels and their history (concerning their exposure to light conditions) are followed and by this the chemical and dynamical aspects of the ozone depletion can be identified.

In the Arctic, the dynamic situation is very important and variations in the circular patterns are displayed in the year-to-year changes of the ozone situation. As in the Antarctic, the ozone depletion is strongly connected to the occurance of PSCs.

The ozone depletion process in the Arctic can be influenced by the dynamical situation in two opposite ways:

1. The greater wave structure of the polar vortex can enhance ozone losses even in winter by increasing the exposure of polar air to sunlight in the distortions of the polar vortex.

2. The same wave activity allows warm air from mid latitudes to mix into the polar region, preventing the formation of PSCs and thus reducing the ozone depletion.

Mid-latitudes

Mid-latitude ozone column trends were found to be much smaller than those of the polar regions, but greater than predicted by gasphase chemistry models Singh and Fabian (2003).

The eruption of Mount Pinatubo in June 1991 occured near the peak loading of atmospheric chlorine (Solomon 1999). This geophysical event provided evidence that heteorogeneous chemical reactions on sulphate aerosols play a key role in ozone chemistry and depletion. Gleason et al. (1993) were the first to report the record low northern mid-latitude ozone abundances in the following year.

However, also for background aerosol conditions, heteorogeneous ozone depletion takes place in the mid-latitude stratosphere (Solomon 1999). The hydrolysis of N_2O_5 reduces NO_x and its impact on ozone in the lower stratosphere, and indirectly enhances the effect of ClO through its control of the ratio of reactive and non-reactive chlorine, as described in section 2.1.2. This reaction take place at all stratosperic conditions, thus also influencing the mid-latitude ozone chemistry Hanson et al. (1996).

Also dynamical aspects play a role for mid-latitude ozone trends. The break up of the polar vortex at the end of the winter may transport air masses with unusual low ozone concentrations into the mid-latitudes (e.g. Wauben et al. (1997) and Tuck and Proffitt (1997)). Especially the northern polar vortex, which is characterised by high dynamic activity can also spread of polar filaments to midlatitudes (Singh and Fabian 2003).

2.2 The present ozone situation

The discovery of the ozone hole in the mid 1980s brought the role of atmospheric chemistry in the global climate into the focus of meteorological research. The following two decades of intense research raised the understanding of stratospheric ozone chemistry to a much higher level. The anthropogenic chloroflourocarbons were identified as the main drivers for the observed ozone depletion and the main chemical and dynamical processes causing the ozone depletion were understood. An international agreement (the Montreal Protocol) banned the ozone depleting substances. Nowadays the point is reached that the atmospheric concentration of the banned species is decreasing and due to that a slow recovery of the ozone layer can be expected.

It is not clear, however, how the ozone layer will develop in a changing climate, which is expected due to the increase of greenhouse gases in the atmosphere. Observations exist where a clear interaction between changed climatic conditions and the ozone chemistry could be identified (IPCC 2001). But many aspects concerning the interactions of the development of the ozone layer and the changing climate are not yet understood.

2.2.1 Ozone distribution before 1970

The global distribution of O_3 is controlled by a combination of production, loss, and transport. The undisturbed global total ozone distribution before 1970 is plotted versus latitude and time in Figure 2.3. It shows the smallest total ozone abundance of ozone at the equatorial region. For latitudes higher than 30° seasonal variations become apparent. At 80° N the relative ozone variation over six months is 50%.

In the northern hemisphere, a maximum of the total ozone columns is observed between 70° and 75° N at the end of March. The southern hemisphere maximum occurs between 50° - 60° S at the end of October. It reaches smaller ozone values, and is located at lower latitudes than that of the northern hemisphere. Both hemispherical maxima occur in the late winter / early spring.

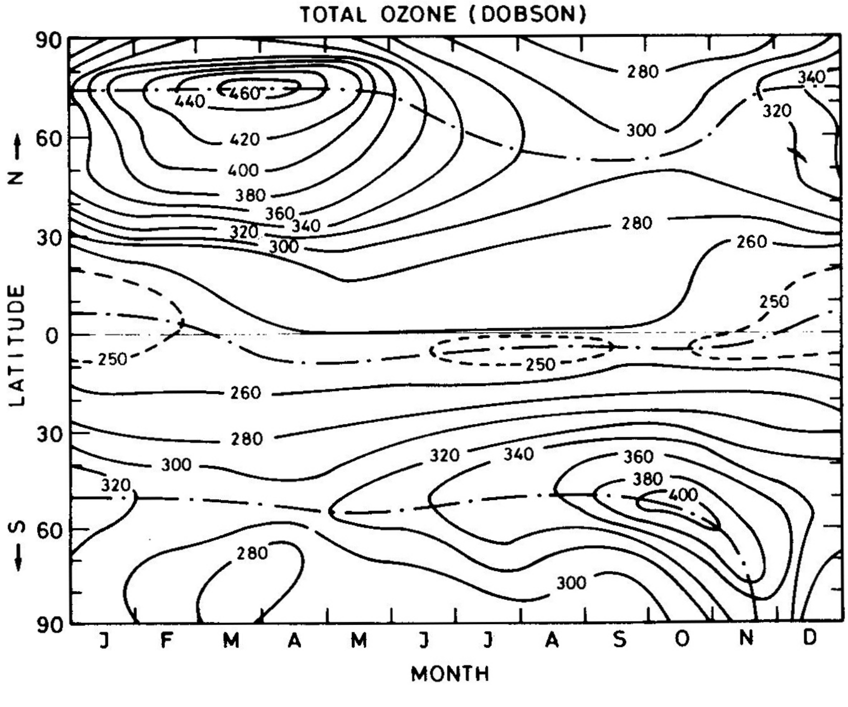

Figure 2.3: The latitudinal distribution and seasonal changes of total ozone before 1970. From London (1990).

Ozone is predominately produced near the equator. The air ascends in the tropics and is transported towards higher latitudes by the natural stratospheric ciruculation, referred to as the Brewer-Dobson-circulation after Brewer (1949) and Dobson (1956). In Holton et al. (1995) our present understanding of the stratospheric circulation and the stratosphere-troposphere exchange is reviewed in detail. The magnitude of the transport has a seasonal cycle in mid and high latitudes with a maximum in winter, thus leading to the build up of O_3 during the darkness of high latitudes winter. The asymmetry in the hemispheric ozone cycles is due to differences in the dynamics of the two hemispheres caused by the different land-sea distributions.

For altitudes above 30 km the lifetime of odd oxygen with respect to production and loss is much shorter than the transport lifetimes. As a result, the distribution of O_3 is controlled entirely by chemical production and loss in these altitudes.

2.2.2 Ozone destruction since the 1980s

Global and hemispheric-scale variations in stratospheric ozone can be quantified from extensive observational records covering the past 20-30 years. Fioletov et al. (2002) analysed six observation series of monthly averaged zonal total ozone for estimating latitudinal and global total ozone temporal variations and trends. Figure 2.4 shows the area weighted deseasonalised total ozone variations in percent for the 60°S – 60°N latitude belt (top), and for the global mean, 90°S – 90°N (bottom). All datasets indicate very similar ozone variations. The global ozone amount shows overall decreasing values between the late 1970s to early 1990s, a relative minimum during 1992-1994, a slight increase during the late 1990s, and very low global ozone values in 2000 and 2001.

For the tropical region between 25°S and 25°N a strong decadal variation of total ozone can be found, with maxima approximately in phase with the 11-year solar cycle. Besides a small decline during 1992-1993 of 1-2%, and a following increase back to former values no significant long-term trend has been observed for the period 1979-2001 (Fioletov et al. 2002).

The midlatitude ozone deviations in Figure 2.5 show clear differences between the Northern (top) and the Southern (bottom) hemisphere. On both hemispheres the overall decrease begins in the early 1980s. For the Northern hemisphere very low values are observed between 1992 and 1996. In 2001 the Northern hemispheric values are about 3% smaller than the pre 1980s values. The decrease on the Southern hemisphere show a more consistent and gradual decline than in the Northern hemisphere. The large negative anomalies observed in the Northern hemisphere between 1992-1996 are almost not visible in the Southern data set. In 2001 the Southern hemispheric values are about 6% smaller than the ozone values before 1980.

A meridional cross section of the trends derived from the combined SAGE I and SAGE II version 6.1 data from the years 1979-2000 is shown in Figure 2.6. The largest percentage changes are observed in the upper stratosphere around 35-45 km, with a magnitude of about -7 to -9% per decade in the middle-high latitudes

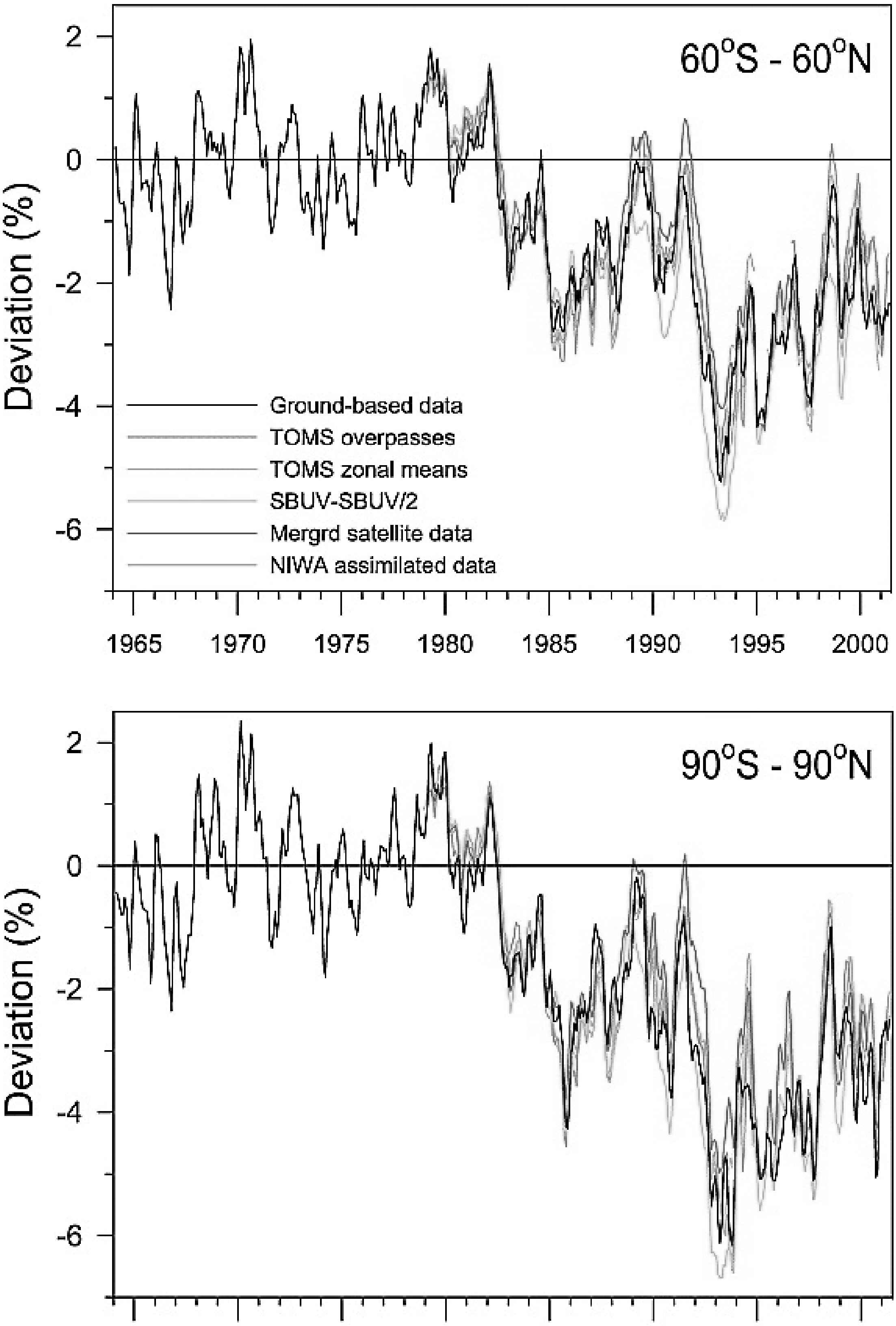

Figure 2.4: Total ozone deviations from the pre-1980 level in percent for the 60°S-60°N zone and for the 90°S-90°N zone. The data are smoothed by 3-month running means. From Fioletov *et al.* (2002).

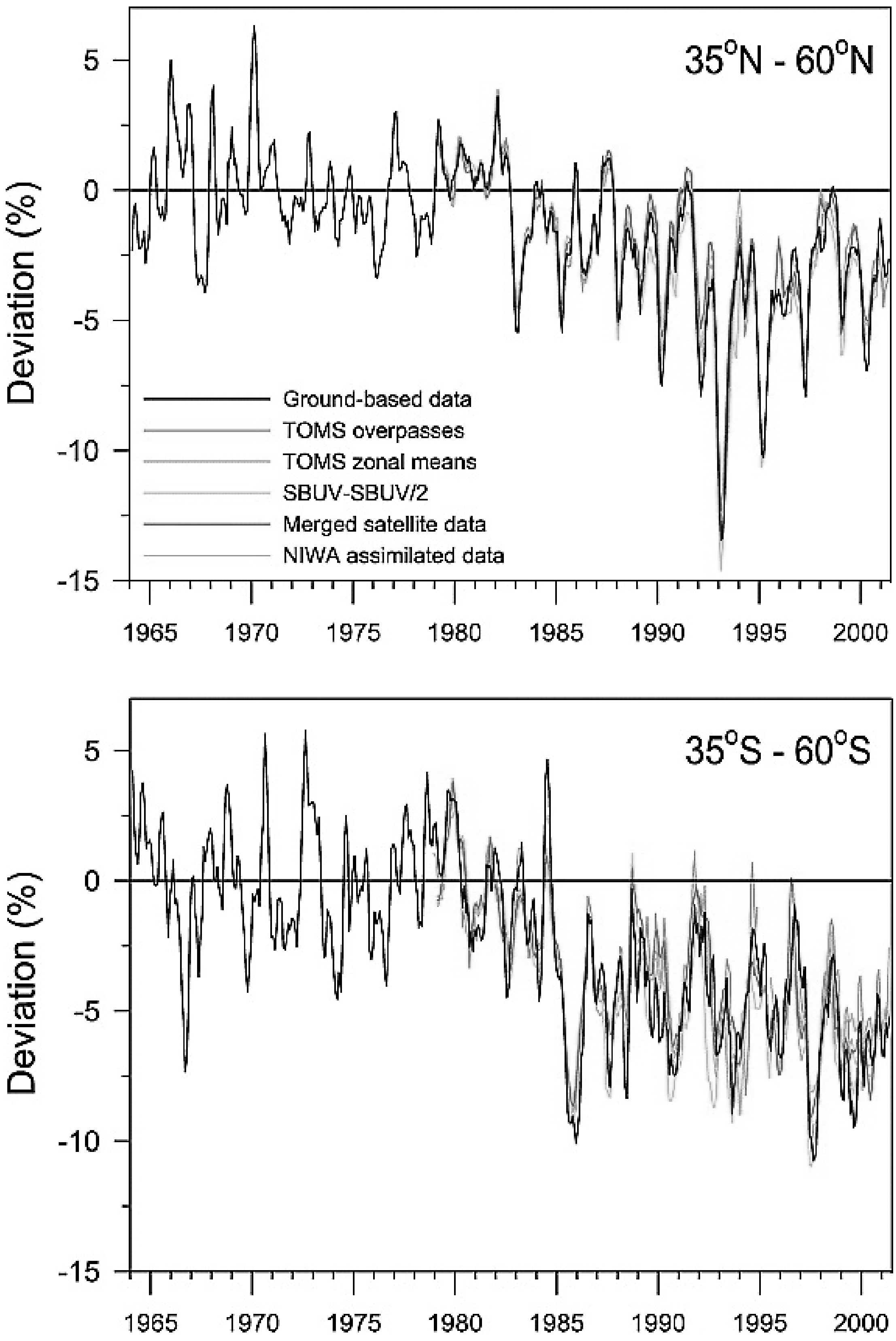

Figure 2.5: Total ozone deviations from the pre-1980 level in percent for the Northern (35°-60°N) and Southern (35°-60°S) midlatitudes. The data are smoothed by 3-month running means. From FIOLETOV *et al.* (2002).

and of about -4% per decade in the tropics. Significant negative trends over the 20 to 25 km altitude region are observed in the extratropics of both hemispheres, with magnitudes of about -2% per decade.

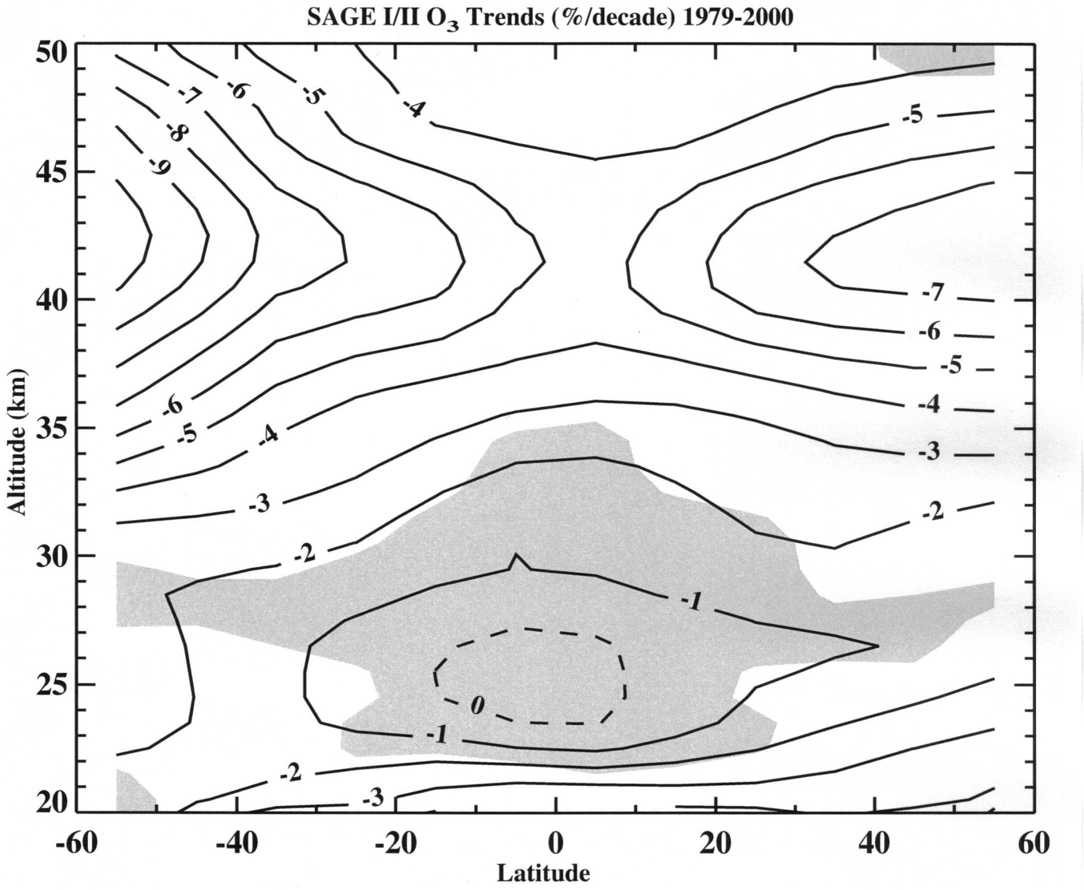

Figure 2.6: Meridional cross section of the ozone trends in percent for altitudes between 20 and 50 km. The trends are derived from the combined SAGE I and SAGE II data from 1979 to 2000, from WMO (2002).

Trends for altitudes below 25 km are derived from data of 14 ozone sonde stations at the Northern midlatitudes by LOGAN (1999). All stations show significant decreases between 1970 and 1996 in ozone, with a range of -3 to -10% per decade near 100 hPa (17 km). For the trends starting in 1980, the decrease in ozone is more negative by 1-2% per decade. The additional inclusion of 4 additional years (1980-2000) results in a smaller maximal decrease of -5% per decade at 80 hPa WMO (2003).

The largest percentage changes in the vertical profiles are observed about 42 km altitude and about 17 km altitude. Because of the vertical distribution of ozone with a maximum at about 20 km altitude, the absolute change is larger in the lower stratosphere (-8.2 DU per decade for 10 to 25 km), while the absolute change in the upper stratosphere is smaller (-1.7 DU per decade for 25 to 50 km).

The region of the Antarctic ozone hole has reached nearly twice the area of the Antarctic continent in recent years. Minimum values of total ozone inside the ozone hole have fallen as low as 100 Dobson Units (DU) compared with normal springtime values of about 300 DU. Balloon measurements show that between 14 and 20 kilometer the ozone is destroyed completely. The data in Figure 2.7 were measured over South Pole and in Sodankyla, Finland WMO (2003).

The Arctic ozone layer is still present in spring as shown by the average March profile over Finland between 1988 and 1997 in Figure 2.7. However, March Arctic ozone values are in some years often below normal average values as shown here for 30.3.1996. In years with extremly low temperatures in the arctic stratosphere as 1999/2000 and the recent winter 2004/2005, the observed Arctic ozone loss is even larger than in Figure 2.7. Chemical processes led to a 70% reduction in a ≈ 1 km layer near 18 km altitude in 2000. (Rex et al. 2002).

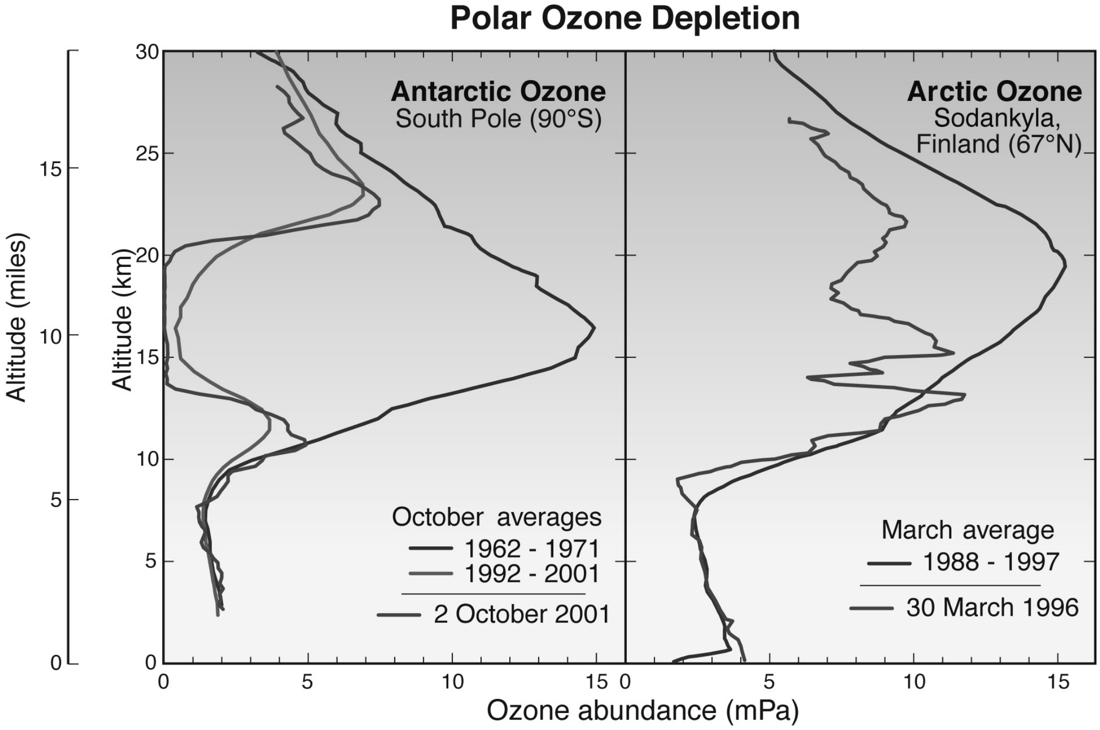

Figure 2.7: Antarctic (left) and Arctic (right) ozone distribution (WMO 2002). The profiles are averaged (blue and green) or show single ECC-sonde measurements (red).

2.2.3 The Montreal protocol

After Molina and Rowland (1974) pointed out the possible ozone destruction by man-made CFCs in the atmosphere, the United Nations Environmental Programme (UNEP) strengthened the efforts for the protection of the ozone layer. In 1985 the Vienna Convention was signed by 28 countries who agreed to cooperate in research and monitoring of the ozone layer and its destroying substances by sharing information on CFC production and emission and controlling the further development. Beyond this agreement on passive controlling further negotiations on the active protection of the ozone layer were continued. The discovery of the ozone hole in the 1980s pushed these negotiations. On 16th September 1987, 46 countries signed the Montreal Protocol. The Protocol required parties to cut the production and the consumption of the main five CFCs by 50% on the levels at 1986. Production and consumption of the three main halons was frozen at 1986 levels starting from 1993. An important feature of the Montreal Protocol was the flexibility designed into it to allow for adaption considering the growth of scientific knowledge and technological developments. Several adjustments and amendments have been added so far. By May 2000 175 countries had ratified the 1987 Montreal Protocol. By the end of 1998 the production of the originally controlled CFCs had fallen by 95% in industrialised countries. The production of the controlled halons had fallen by 99%. Since the Montreal Protocol permits longer phase-out periods for development countries, the overall world production has declined by about 88% (CFCs) and 84% (halons) from the base year 1986. The increase of the atmospheric concentration of the major ozone depleting chemicals has clearly slowed down (see Figure 2.8). The ozone loss due to ozone depleting substances is expected to decrease in the future. But the total ozone depletion may behave different with a raising impact of a changing climate on ozone chemistry.

2.3 Stratospheric chemistry and climate change

The observed stratospheric ozone depletion over the past two decades was largely due to the described chemical depletion by chlorine- and bromine containing substances (CFCs). These ozone changes have a subsequent impact on climate. The climate change, induced by the enhanced concentration of greenhouse gases (GHG), will vice-versa have an impact on the future ozone situation. As pointed out in the *Scientific Assessment of Ozone Depletion (2002)* of the World Meteorological Organisation (WMO), the *Third Assessment Report on Climate Change (2001)* of the International Panel of Climate Change (IPCC), and Hassol (2004) the closed coupling between ozone and climate happens through many interacting chemical and dynamical processes, operating in either direction. The complexity of the feedback processes makes it difficult to quantify the impact of single processes. Some of the areas where strong coupling between climate change and ozone can be found are summarised here.

The enhanced abundances of GHGs like CO_2, CH_4, and others, cause a cooling in the stratosphere, in contrary to the induced warming of the troposphere. Additionally, the ozone depletion by itself contributes to a cooling effect in the stratosphere, since ozone is the major heat source in the stratosphere. Furthermore, the indirect effect of changes in the dynamical structure of the stratosphere, also related to enhanced concentrations of GHGs, may also have an impact on the stratospheric temperatures. Lower temperatures in the lower polar stratosphere will increase the occurance of PSCs, thus leading to enhanced ozone depletion. Rex et al. (2004) quantified the relation between winter-spring loss of Arctic ozone and changes in stratospheric temperatures. They expect $\approx$ 15 DU additional ozone loss per Kelvin cooling of the Arctic lower stratosphere. In the upper stratosphere the colder temperatures are expected to work against the ozone depletion due to a slowdown of the gas-phase chemical loss reactions.

The observed warming of the troposphere influences the dynamics in the troposphere and in the stratosphere. That effects the atmospheric transport and the stratosphere-troposphere exchange of trace gases. One example is the dynamic interaction between tropospheric weather systems and the ozone of the lower stratosphere. Low values of ozone are related to tropospheric anticyclones and a high tropopause. Measurements at the meteorological observatory Hohenpeißenberg, Germany show that the tropopause height has increased about 120 m per decade and was strongly correlated to the column ozone (Steinbrecht et al. 1998).

Besides their direct and indirect radiative effects some of the GHGs, such as CH_4 and N_2O, have an additional direct influence on atmospheric chemistry.

Unclear is the effect of water vapor in the lower stratosphere. There are some hints about a recent water vapor increase in the stratosphere (Rosenlof et al. (2001) and Oltmans et al. (1995)). Changes of water vapor in the stratosphere are related to CH_4-increase and to changed dynamics. For Polar regions higher water concentrations may decrease the treshold temperatures for PSC-formation.

The effects of aerosols are difficult to predict. Aerosols have a positive and a negative effect on radiation and of course their chemical composition will also effect the chemical processes, Dameris (2005).

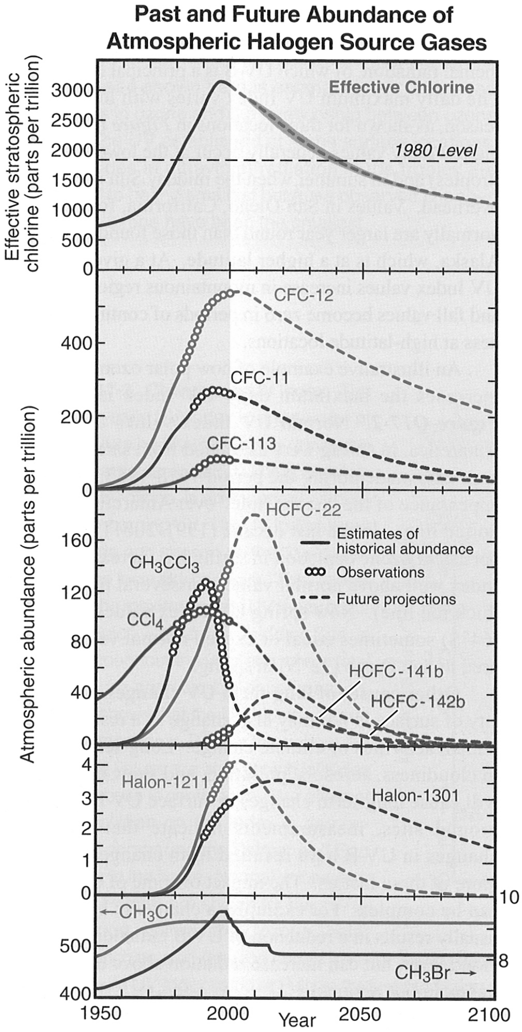

Figure 2.8: Past and Future Abundances of Atmospheric Halogen Source Gases. The total combined abundance of ozone depleting species peaked before 2000 and now slowly declines. Effective chlorine values combine the abundances of chlorine-containing gases with those of bromine-containing gases. The atmospheric increases of the CFC have slowed down, and CFC-11, and CFC-113 abundances have decreased slightly. Because of longer lifetimes, CFC abundances decrease more slowly than methyl chloroform (CH_3CCl_3), which showed the largest reduction. The Montreal Protocol allows for the use of hydrochloroflurocarbons (HCFCs) as shortterm substitutes for CFCs. As a result their abundances continue to grow. The shown halons are bromine-containing source gases. Although their production in developed countries is nearly zero since 1994, they continue to grow. This is due to the fact that substantial amounts are currently stored in fireextinguishing equipment and are only gradually released. Furthermore, the consumption and production are still allowed in developing nations. Methyl bromide and methyl chloride have substantial natural sources. Methyl chloride is not regulated and will remain constant, whereas methyl bromide will decrease because of the regulation of the Montreal Protocoll and will then remain constant in balance with its natural sources. From the Scientific Assessment of Ozone Depletion, 2002

Chapter 3

Measurement methods for stratospheric ozone and other trace gases

Because chemical atmospheric constituents play an important role in the climate system a complete knowledge about the horizontal and vertical distribution and its changes (by chemical and dynamical processes) of the chemical compounds is necessary.
Since the beginning of the 20th century ozone monitoring instruments have been developed and widely used. A first measurement network for total column ozone measurements was established by Dobson in 1926 Labitzke (1999).
One of today's important networks is the Network for detection of Stratospheric Change (NDSC), which monitors the temporal and spatial variability of the stratospheric composition and structure in order to provide early detection and long-term monitoring of changes in the chemical and physical state of the stratosphere and upper troposphere. Ozone and key ozone-related chemical compounds and parameters are targeted for measurement from 20 sites worldwide (plus a large number of complementary stations). So the links between changes in stratospheric ozone, UV radiation at the ground, atmospheric chemistry and climate can be established (http://www.ndsc.ncep.noaa.gov/).
Backbone of the network are various groundbased instruments, which measure total column ozone as well as concentration profiles using different optical techniques. The ground based measurements are completed with airborne measurements, such as balloon-borne sondes or other, which offer in situ measurements of ozone concentration profiles.
The NDSC sites are excellent places for the validation of space-based sensors. Satellite instruments for measuring atmospheric parameters offer the possibility of global coverage within a few days.
Most of these instruments measure by means of optical methods. The theoretical background is presented for the retrieval of atmospheric trace gas abundances of electromagnetic radiation measurements. Then, the main instruments will be

shortly presented.
As an example for a non optical method, the electrochemical ozone sonde is described.

3.1 Optical methods

Optical measurements of trace gas abundances are based on the optical properties of chemical gaseous species and their interaction with electromagnetic radiation passing the atmosphere.
Trace gases have absorption and emission lines in the ultraviolett (UV), the visible (vis), the infrared (IR), or the microwave range of the radiation spectrum.
Each species has its characteristic spectral line or bands, where it attenuates light by absorption. By measuring the attenuation of light passing through a defined part of the atmosphere, the amount of the absorbing trace gas can be determined. Figure 3.1 shows some important trace gases and their absorption band or lines in the solar spectrum, illustration after *http://www.iup.physik.uni-bremen.de/sciamachy*.

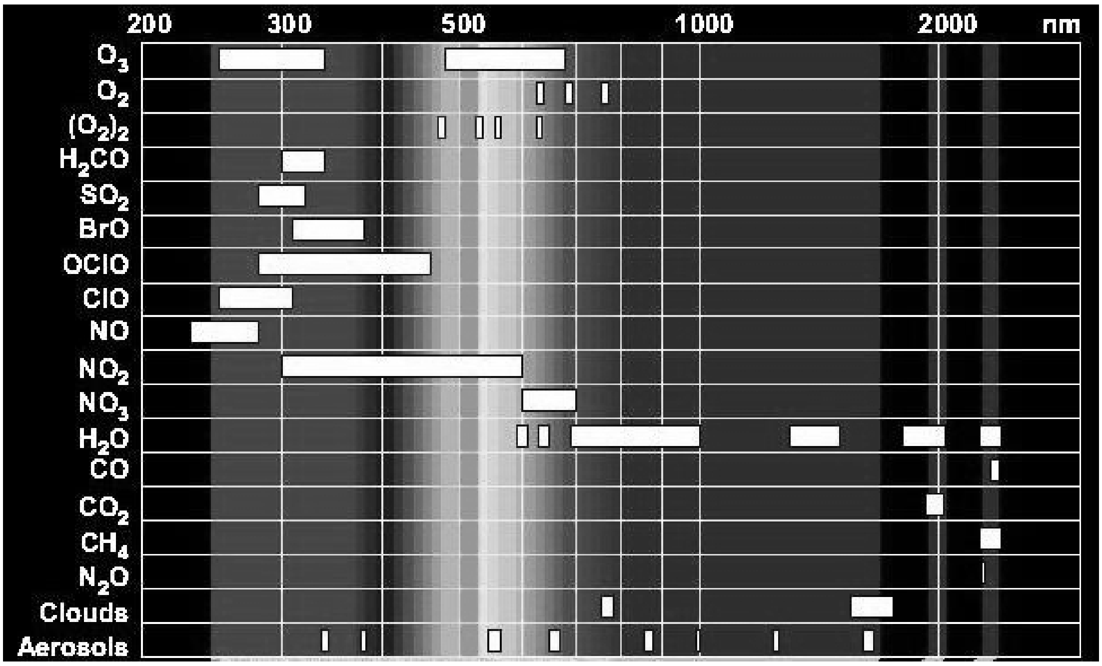

Figure 3.1: Different trace gases and their absorption bands or lines in the UV/visible and near infrared spectrum.

3.1.1 Trace retrieval by absorption spectroscopy

The absorption of a lightray of incident intensity I_0 of a wavelength λ, passing through a infinitesimally layer dx of a medium with one absorbing species is expressed by the Beer-Lambert-law:

$$dI = -A(\lambda) \cdot I_0(\lambda) \cdot dx. \tag{3.1}$$

The factor of proportionality A is the absorption coefficient of the medium. The absorption coefficient is proportional to the concentration of the absorber n:

$$A(\lambda) = \sigma(\lambda) \cdot n, \tag{3.2}$$

$\sigma(\lambda)$ is the absorption cross section. Integrating Equation 3.1 leads to

$$I(\lambda) = I_0(\lambda) \cdot \exp\left[-\int\limits_s \sigma(\lambda) n(s) ds\right]. \tag{3.3}$$

In the atmosphere often more than one absorber has to be considered. For the absorption from J absorbers the intensity I is:

$$I(\lambda) = I_0(\lambda) \cdot \exp\left[-\int\limits_s \sum_{j=1}^{J} \sigma_j(\lambda) n_j(s) ds\right]. \tag{3.4}$$

Light in the atmosphere is additionally attenuated by scattering. If the light is scattered by atmospheric molecules (Rayleigh scattering), then it is distributed equally into the forward and backward directions. The theory is for example described by PENNDORF (1957), who also gives scattering cross sections for gas molecules. Scattering cross sections are approximately proportional to λ^{-4}.

Aerosols also interact with the radiation (Mie scattering). Due to their size, which is in the same order of magnitude or larger than the wavelength of the solar light, the scattering does not follow the principles of Rayleigh scattering. The scattering depends on the shape and the size of the scattering particles. The main part of the light is scattered into the forward direction. In practice, simplified formulas are often used (see for example VAN DE HULST (1957)).

The attenuation due to scattering processes can be expressed analogue to the absorption by the Beer-Lambert law. Instead of the absorption coefficients, scattering coefficients are used. The complete attenuation is the sum of absorption and scattering processes. Accordingly, the attenuation coefficient is then expressed as the sum of absorption and scattering coefficients:

$$A_{ext} = A_{abs} + A_{Ray} + A_{Mie}. \tag{3.5}$$

Similar to equation (3.4), the attenuated radiation is expressed as:

$$\begin{aligned} I &= I_0 \cdot \exp\left(-\int_s \sum_{j=1}^{J} \sigma_j(\lambda) n_j(s) ds\right) \\ &\cdot \exp\left(-\int_s \sigma_{Ray}(\lambda) n_{air}(s) ds\right) \cdot \exp\left(-\int_s \sigma_{Mie}(\lambda) n_{aer}(s) ds\right). \quad (3.6) \end{aligned}$$

The number density of the scattering air molecules is n_{air}, and the number density of aerosols is expressed with n_{Aer}.

For simplification, the height dependencies of the absorption cross sections are neglected. Then the integral over the particle concentration along the light path gives the amount of particles in the slant column ($SC = \int n(s)ds$) between the instrument and the top of the atmosphere:

$$I = I_0 \cdot \exp\left(-\sum_{j=1}^{J} \sigma_j(\lambda) SC_j\right) \cdot \exp\left(-\sigma_{Ray}(\lambda) SC_{air}\right) \cdot \exp\left(-\sigma_{Mie}(\lambda) SC_{aer}\right). \quad (3.7)$$

Generally, the amount of an attenuating medium integrated along the vertical path is of greater interest than the slant path amount. Therefore the slant path has to be corrected with the air mass. The air mass (AMF) describes the ratio of the amount of an attenuating medium integrated along a slanted path through the atmosphere to the amount integrated along a vertical path. Neglecting the curvature of the atmosphere, the airmass can be determined depending on the solar zenith angle (SZA) as the ratio of the hypotenuse to the adjacent leg of a right triangular, which equals: AMF $= SC/VC = 1/\cos(\text{SZA})$. For air the air mass at a solar zenith angle SZA is defined as (Kasten and Young 1989):

$$AMF(SZA) = \frac{m(SZA)}{m(0)} \quad (3.8)$$

with:

$$m(SZA) = \rho_0 \int_0^{\infty} (\rho/\rho_0) \cdot \left[1 - (1 + 2\delta_0(1-\rho/\rho_0)) \cdot (cos(90 - SZA)/(1 + h/R)^2)\right]^{\frac{-1}{2}} dh \quad (3.9)$$

and h = height about mean sea level, $\rho = \rho(h)$ = air density at height h, ρ_0 = air density at $h = 0$, $\delta_0 = n_0 - 1$, n_0 = refractive index for air at 0.7 μm wavelength at $h = 0$, R = mean Earth radius.

For each attenuating medium, such as absorbing trace gases, scattering air molecules, and scattering aerosols, a slightly different airmass is existing, owing principially to their different height distribution and the sphericity of the atmosphere. However, all are approximately equal for small solar zenith angles, Basher (1982).

Substituting the slant columns in Equation 3.7 with the vertical columns corrected for the airmass gives the attenuated radiation I, depending on amounts of attenuating molecules in the vertical colums:

$$
\begin{aligned}
I \;=\; & I_0 \cdot \exp\left(-\sum_{j=1}^{J}\sigma_j(\lambda)VC_j \cdot \mathrm{AMF}\right) \\
& \cdot \exp\left(-\sigma_{Ray}(\lambda)VC_{air}\cdot \mathrm{AMF}\right)\cdot \exp\left(-\sigma_{Mie}(\lambda)VC_{aer}\cdot \mathrm{AMF}\right). \quad (3.10)
\end{aligned}
$$

The product of the cross section and the amount of molecules in the vertical column gives the optical depth of the medium. For example, the Rayleigh optical depth is expressed as:

$$\tau_{Ray}(\lambda) = \sigma_{Ray} \cdot VC_{air}. \quad (3.11)$$

3.1.2 Optical measurement systems

The instruments described in the following are all based on radiation measurements. The detected radiation was attenuated on its way through the atmosphere by absorption and scattering processes as described in Equation 3.10. The retrieval of the trace gas abundance based on this radiation measurements differs depending on the instrumental characteristics.

Dobson spectrometer

The Dobson spectrophotometer consists of a double monochromator and is used for determining total column ozone by measuring the ratio of intensities of two selected wavelenghts in the solar UV spectrum, Dobson (1931). One of the wavelengths absorbs ozone far more strongly than the second wavelength. The intensity ratio is used to estimate the total amount of ozone in the optical path from the Sun to the spectrophotometer. By using one pair of wavelengths, the effects of differential scattering by atmospheric molecules and aerosols are still included. If measurements at two wavelength pairs are combined, the scattering effects essentially cancel, because they are similar for different wavelength pairs. 4-5 wavelength pairs can be selected, depending on measuring conditions. The instrument can be used with direct or scattered sunlight.

Fourier-transform infrared spectroscopy

Fourier-transform infrared spectrometers (FTIR) use direct sun- or moon-light as radiation sources, (e.g. Becker and Notholt (2000)). The radiation is directed by a beam splitter into the two arms of a Michelson interferometer. With this type of instrument a wide wavelength range can be detected, typically covering the IR-range of the spectrum. By varying the length of one arm of the interferometer a complete spectral scan is done. The obtained interferogram can be converted into a standard spectrum by Fourier transformation. Vertical column densities of various trace gases can be obtained, like CFCs, reactive odd chlorine and odd nitrogen, chlorine reservoir gases, and ozone.

Differential optical absorption spectroscopy

With differential optical absorption spectroscopy (DOAS) scattered sun- or moonlight in the UV/vis range is measured. Some instruments are designed for occultation measurements. The measured data are analysed for the atmospheric columns of a number of important atmospheric traces species such as O_3 , NO_2, BrO, OClO, and O_4. For the analysis, the DOAS-method is used (Perner and Platt 1980). In this technique, only the differential structures of the absorption cross-sections are taken to identify absorbers and to quantify their integrated amount along the light path. Broadband absorption and extinction by Mie and Rayleigh scattering and broadband instrumental features are removed by a polynomial of low order.

Microwave radiometry

With a microwave radiometer the rotation changes of molecules are measured. The shape and intensity of the measured line contains information about the altitude of the detected molecules. Trace gas profiles of O_3 , H_2O and ClO with a height resolution of about 10 km between 12 and 55 km can be obtained with this method, Langer (1999). For example, the rotational transitions of ozone are measured at 142.17504 GHz with a bandwidth of 1.65 GHz. Because of scanning in the microwave range, the microwave radiometer is independent of clear sky conditions and can measure around the clock.

Light detection and ranging

In contrast to all described systems, which use the sun or the moon light or t emitting molecules themselves as light source, the light detection and ranging (LIDAR) system measures its own active lightsource: a pulsed laser beam. A detailed description can be found in Wahl (2002).

The laser beam is directed into the sky and the backscattered light is collected with a mirror and a photomulitplier detection system. Two laser beams are sent out simultaneously. The first wavelength is strongly absorped by ozone (e.g. 308 nm), whereas the absorption of the second wavelength (e.g. 353 nm) is neglible. The laser pulses are scattered back from each altitude level because of the Rayleigh-scattering. It is recollected by a telescope at the ground. The difference in the measured extinction of the two wavelengths is mainly due to the ozone absorption. The ozone content can be calculated. The information about the height is obtained by the time delay between sending and receiving of the pulsed laser light. Measurements with a LIDAR system require clear sky conditions.

Balloon-borne instruments

For airborne ozone measurements optical methods are also widely used. Regener and Regener (1934) carried out the first direct measurement of the vertical ozone distribution with a balloon borne UV spectrograph. Since these pioneering measurements, the optical instruments and the telemetry possibilities have been developed, so that today very sophisticated instruments are in use for airborne ozone measurements.

Absorption measurements by means of filter radiometers have been performed by balloon and rockets, using the sun as light source, see for instance Holland et al. (1985), Barnes and Simeth (1986), Kobayashi and Toyama (1966), and Okano et al. (1996). Ratios between irradiances measured at two wavelengths yield the ozone column content above the sensor. Vertical profiles are deduced by differentiation. This method does not require the knowledge of the absolute value of solar extraterrestrial irradiance but only the spectral bandpass of all of the optical components, the relative distribution of solar irradiance and the absorption cross-section of ozone within the filter band passes. The advantage of the filter radiometers is the comparably light weight, so that high altitudes can be achieved by stratospheric balloons or rockets. The optical design of the instrument requires the preselection of the two filter wavelengths and does not allow for change to other wavelengths in order to measure the concentration of other trace gases by detecting their absorption lines.

Ferlemann et al. (2000) describe a DOAS-instrument for stratospheric balloon-borne trace gas measurements. Like the groundbased DOAS, this instrument can measure the concentration profiles of various trace gases, such as O_3, O_4, H_2O, NO_2, OClO, BrO, IO, and OIO. It contains two grating spectrometers in one thermostated (273 K) and evacuated housing. With a solar tracker direct solar radiation can be collected. The instrument has a weight of 45 kg and is operated on the azimuth controlled LPMA/DOAS gondola. The gondola can be started from specially equipped launching sites.
To limit the costs and the necessary logistics, the actual development is based on miniaturising the instruments to get more versatile systems, concerning costs and logistics. Weidner et al. (2005) has developed a Mini-DOAS, with a weight of 7 kg. Trace gas profiles of O_3 and BrO were measured successfully. The instrument is temperature stabilised and is operated on the LPMA/DOAS gondola, because an azimuth controlled position is necessary for the data retrieval.

Space-borne instruments

In October 1959 the Satellite Explorer 7 started with the first succesfull meteorological instrument on board: the SUOMI Radiometer. The first coarse maps of the solar radiation reflected by the Earth and the infrared radiation emitted by the Ears were made with the data of this mission (Kidder and Vonder Haar 1995).

Since then numerous meteorological satellite missions have been carried out. Satellite measurements provide global coverage within a few days and deliver a comprehensive picture of the state of the atmosphere. Column ozone have been measured by TOMS (total ozone mapping spectrometer) instruments on various spacecraft since 1978. Today TOMS is operated on board the satellite Earth Probe. The long total ozone data record will be continued by OMI (ozone monitoring instrument) aboard AURA, which was launched in July 2004, more information at *http://toms.gsfc.nasa.gov/eptoms/ep.html* and *http://www.nasa.gov/-mission_pages/aura/main/index.html*.

The European Space Agency is operating ENVISAT, a satellite in orbit since March 2002 with ten instruments on board. One of the them, SCIAMACHY (SCanning Imaging Absorption SpectroMeter for Atmspheric CHartographY), measures sunlight transmitted, reflected and scattered by the Earth's atmosphere or surface in a wide wavelength range covering UV, vis and near IR (220 - 2380 nm) with a resolution of $\Delta\lambda$ = 0.2 - 1.5 nm (Bovensmann et al. 1999). SCIAMACHY measures in three viewing geometries: Nadir, limb, and occultation. In nadir mode the atmosphere under the instrument is observed. During limb mode the instrument looks at the edge of the atmsophere and with scans at different tangent altitudes, different layers of the atmosphere are examined. If the sun or the moon is in the field of view of the instrument while looking at the edge of the atmosphere (as in limb mode) occultation measurements can be performed. As the sun (or moon) sets or rises through the atmosphere, the pathlength of the light through the atmosphere increases or decreases and the solar (or lunar) spectrum becomes more or less attenuated by the absorption of the various gases. These attenuated spectra are compared to the extraterrestrial solar (or lunar) spectrum measured outside the atmosphere with a small time delay. A specialty of SCIAMACHY is the possible combination of limb and nadir measurements. The same atmospheric volume can be observed first in limb and then after about 7 minutes in nadir geometry. This allows the determination of tropospheric trace gas column amounts.

Using this alternating limb/nadir scan option global coverage is achieved within 6 days. SCIAMACHY measures concentration profiles in the stratosphere and troposphere of numerous trace gases, such as O_3, BrO, OClO, ClO, SO_2, H_2CO, NO_2, CO, CO_2, CH_4, H_2O, and N_2O, as well as aerosol profiles, cloud coverage, cloud top height, temperature, and pressure.

SAGE III (Stratospheric Aerosol and Gas Experiment) uses a grating spectrometer that measures UV and vis radiation from either the sun or the moon by vertically scanning across the object (Polyakov et al. 2005). The spectral coverage ranges from 290 to 1030 nm plus a discrete photodiode at 1550 nm. SAGE III obtains profile measurements of aerosol extinction, O_3,, H_2O, NO_2, NO_3, OClO, temperature, pressure and clouds in the mesosphere, stratosphere, and upper troposphere with a vertical resolution of 0.5 - 1 km. One SAGE III instrument is mounted on the Meteor-3M spacecraft and was launched December

2001. A second will be placed in orbit on the International Space Station in the near future (http://www-sage3.larc.nasa.gov).

3.2 Non optical methods for ozone measurements

The electrochemical concentration cell sonde (ECC-sonde) is the worldwide mostly used sensor for in situ balloon-borne ozone observations, KOMHYR (1969). The ozone sensor is coupled via an interface to a meteorological radiosonde for data telemetry. The combined payload of the ozone sensor (7.6 x 7.9 x 13.3 cm) and the radiosonde weighs less than 1 kg. The ozone sensor, see Figures 3.2 and 3.3, has two bright-platinum electrodes immersed in potassium iodide (KI) solutions of different concentrations, contained in separate cathode and anode chambers. The chambers are linked with an ion bridge, so that an exchange of ions is possible, whereas the concentration differences remain unchanged. The ambient air is forced through the sensor by means of a pump, fabricated from inert Teflon. An O_3 -molecule, which enters the cathode starts the following reaction:

$$2KI + O_3 + H_2O \rightarrow 2KOH + I_2 + O_2. \tag{3.12}$$

The produced iodine (I_2) reacts with two electrons, which are produced at the anode and transported via the ion bridge to the cathode to Iodide ($2I^-$), thus producing an electric current between the chambers. By measuring the current, the amount of ozone can be determined.

KOMHYR et al. (1995) estimated the ozone measurement accuracies based on laboratory tests and comparison of ECC-sonde ozone measurements with other instruments during the Stratospheric Ozone Intercomparison Campaign (STOIC), 1989. Accuracies for ECC-sondes are estimated to be about 6% near the ground, between -7 to 17% in the high troposphere, increase to about ±5% in the low stratosphere and remain so to an altitude of about 32 km, and then decrease to -14 to 6% at 38 km.

Beside the ECC sonde, another electrochemical ozone sonde is used: the Brewer-Mast sonde. Generally, the same measurement principle is applied for the ozone measurements. A detailed description is given by CLAUDE et al. (1987).

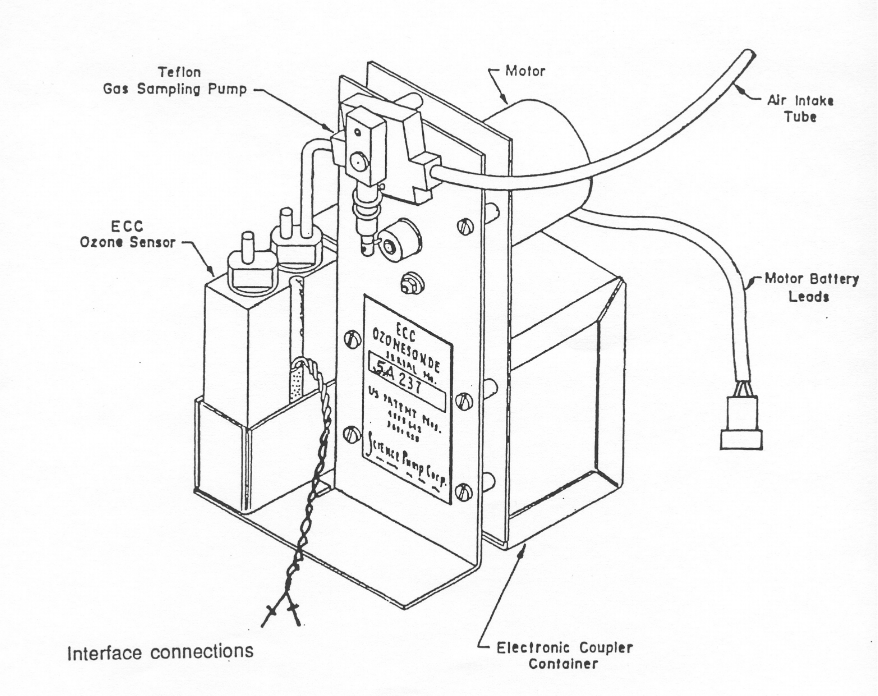

Figure 3.2: Schematic diagramme of an electrochemical concentration cell (ECC) ozonesonde, showing the principal components of the instrument

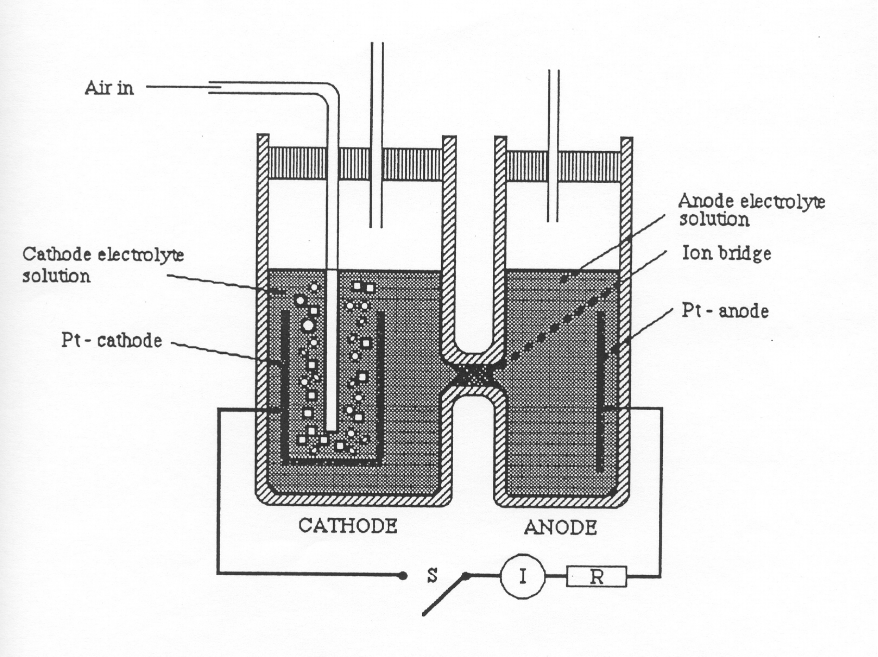

Figure 3.3: Schematic diagramme of the ECC ozone sensor, showing the measuring principle.

Chapter 4

The PIOS instrument

The goal of this work was the development of a new sonde, which closes the gap between the standard ECC ozone sondes and the sophisticated optical sensors for measuring different trace gases. The latter are used on large size stratospheric balloons, which can only be launched from specially equipped starting sites.
The new sonde should become a versatile tool for case studies and satellite validation by combining the advantages of both systems:

- cost-efficient and very easy to handle
- low weight and small size
- independent from specially equipped launching sites or additional instrumentation
- ability to measure different trace gases simultaneously by using an optical method
- measurements possible up to 40 km altitude

In this chapter the new sonde, which has been developed in the frame of this work is presented. The balloon-borne sensor measures the spectral solar irradiance and meteorological data simultaneously. To reduce developing time and cost of the sonde, well-established techniques and parts readily available were used whereever possible. The design of the sonde is based on its three main modules:

1. a miniature grating spectrometer (USB2000UV/vis, Ocean Optics Inc., USA), which measures the dispersed sunlight in the UV/vis wavelength range;
2. a radiosonde (SRS-C34, Meteolabor AG, Switzerland), which measures pressure, temperature, humidity, and GPS position and furthermore, transmits the data set to a ground station;

3. a controlling unit (isitec GmbH, Germany), which synchronises the optical and the meteorologcial data sets and prepares them for transmitting to a ground.

The new sonde is registered as an utility model WOLFF and RUHE (2004) at the Deutsches Patent- und Markenamt (German Patent and Trademark Office). It is named PIOS (platform independent optical sensor).

4.1 Technical design of the instrument

4.1.1 Spectrometer and sampling optics

The incoming light enters the system via a cosine corrector (CC-3-UV, Ocean Optics Inc.) at the top of the sonde. The cosine corrector is designed to collect radiation from a 180° field of view. That guarantees measurements with the sun always in the field of view, independent of the actual sun elevation. Furthermore it reduces the temporary oscillation of the incoming radiation caused by the swinging of the payload. The diffusing material used in the cosine corrector is a thin plane disk of PTFE (teflon) that is located at the end of a stainless steel barrel with a diameter of 6.3 mm. The angular response of the cosine corrector is typical for a plane diffusor as described in BERNHARD and SECKMEYER (1997). For all angles the response function of the CC-3 shows sligthly smaller values than the cosine function. The differences are raising towards higher angles. At 40° the response function is 8% smaller than the cosine function (http://www.oceanoptics.com/technical/cc3.pdf).
A fibre optic cable (length 40 cm; diameter 400 μm) is used to direct the light from the diffusor into the miniature grating spectrometer. The dimensions of the spectrometer are 89 mm x 64 mm x 34 mm. Figure 4.1 illustrates the main components of the miniature spectrometer and the optical path. Light fibre and spectrometer are connected with a SMA connector. The light is entering the spectrometer through a slit with a slit width of 25 μm. The collimating mirror focuses the light entering towards the grating. A grating with 600 lines mm^{-1}, blazed at 300 nm was selected to cover a wide wavelength range between 200 and 850 nm. The spectrometer is available with other gratings in different groove densities, allowing for a different wavelength coverage and resolution in the spectrometer. The dispersed light is directed onto the focusing mirror, which focuses it onto the detector: a 2048-channel charge coupling device array (CCD), ILX511 from Sony Inc.. At each channel a photodiode is collecting the incoming photons within one integration period and discharge a capacitor at a rate proportional to the photon flux. When the integration time is complete, a series of switches (one for each capacitor) closes and the charges are transported to the shift register. After the completed transfer, the switches open again and the capacitors attached to the photodiodes are recharged and a new integration period begins. At the same time that light energy is being integrated, the data is read out of the shift register by

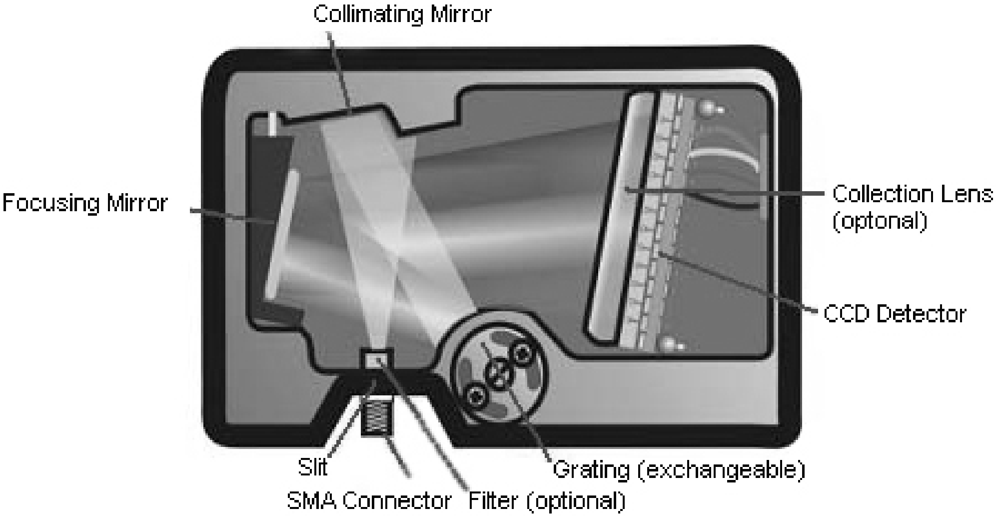

Figure 4.1: Schematical illustration of the optical path in the miniature spectrometer USB2000 (OceanOptics Inc.). The labelled components are explained in section 4.1.1. Taken from Ocean Optics (2003)

an A/D converter. The whole spectrum is measured simultaneously. This guarantees the detection of all photons under the same conditions independent of the movements of the payload.

For this study the spectrometer operates with integration times between 20 and 255 ms out of a possible range of 3 to 30000 ms.

Additionally, a collection lens can be attached to the CCD. It focuses light from a tall slit onto the shorter CCD detector elements. That would improve the light-collecting efficiency. The spectrometer used in this work were not equipped with the optional lens.

4.1.2 Radiosonde

The actual meteorological conditions, i.e. temperatures of the ambient air and of the spectrometer, pressure, humidity, and GPS position are measured with the radiosonde SRS-34 (meteolabor AG). Figure 4.2 shows a photograph of an open radiosonde in its polystyrene housing (dimensions: 345 x 210 x 90 mm). Table 4.1 details the characteristics of the used sensors. The radiosonde consumes a

parameter	**sensor**	**range**	**error**
temperature	copper-constantan couple	−100°C - +60°C	±0.1K
pressure	hypsometer distilled water	−10°C - +110°C 6hPa-1000hPa	±0.1K $\leq 1\%$
humidity	carbon element	−60°C - +40°C 0-100%	2%
position	GPS-receiver		horizontal 10 m vertical 20m

Table 4.1: Sensors and their characteristics of the radiosonde SRS-CR34

current between 245 and 480 mA.

The temperatures of the ambient air and of the spectrometer are measured with fast response copper-constantan thermocouples with 0.05 mm diameter. The small size minimises the error due to radiation. The sensor of the air temperature is placed outside on top of the sonde. It is attached with a thin wire to keep a distance of about 15 cm to the housing. The sensor for measuring the temperature of the spectrometer is directly attached to the spectrometer's housing. Both sensors have a temperature range between −100°C and +60°C and an absolute accuracy of ±0.1K.

The air pressure is measured with a hypsometer. Compared to the widely used aneroid capsule for pressure measurements the hypsometer provides data which are less sensitive to rapid temperature changes which often can occur during the transport of radiosonde from the indoor preparation room to the outside launching place.

During flight preparation 1 ml of distilled water has to be filled into a small glass tube. When activating the hypsometer the water is continuously heated to its boiling temperature which is measured with a copper-constantan thermocouple. The temperature sensor has a temperature range of −10°C to +110°C with an accuracy of 0.1 K. Figure 4.3 displays the absolute pressure difference for an error of 0.1 K in the water boiling temperature. At a surface pressure of 1000 hPa, the relative error caused by a temperature difference of 0.1 K is 0.35%. The relative error is increasing very slowly with decreasing pressure values. At 100 hPa, the relative error is 0.5% and at 10 hPa, the relative error of the pressure measurement is 1% (Richner and von Hünerbein 1999). For comparison, the Vaisala Barocap sensor has an accuracy of 1.5 hPa between 1080 hPa (0.14%) and 100 hPa (1.5%) and of 0.6 hPa between 100 hPa (0.6%) and 3 hPa (20%). For pressures under 400 hPa the hypsometer is more accurate. Pressure measurements with a hypsometer are limited to a minimum pressure of 6.1 hPa, where water has its triple point and evaporates entirely.

A fast response VIZ ACCU-LOK carbon hygristor is used to measure humidity. The provided range extends from 0 to 100% RH, from −60°C - +40°C, with an accuracy of 2% RH. For the further data analysis the humidity measurements will not be used.

Latitude, longitude and altitude is determined by a GPS-receiver (C/A Code, 16 channels) with an antenna on top of the sonde.

To ensure uninterrupted altitude information, the altitude of the sonde is determined by two independent means: (1) barometric height of the pressure measurements, and (2) the GPS altitude. The hypsometer compensates for short GPS outages that mainly occur in lower altitudes. The movements of the sonde causes short signal losses, because the satellites may shortly set below the antenna's horizon. The GPS offsets for the fact that the hypsometer ceases to function when water reaches its triple point at 6.1 hPa ($\approx$ 35 km).

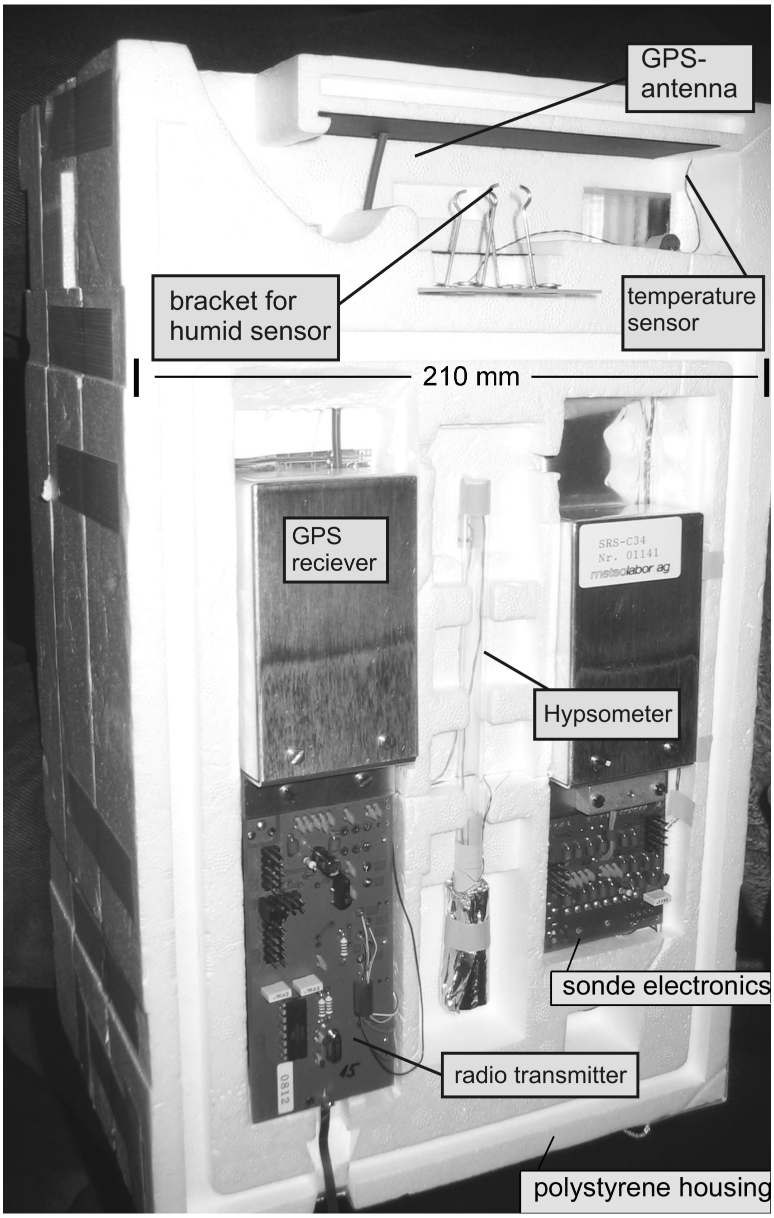

Figure 4.2: Photograph of the meteorological part of the new sonde, the radiosonde SRS-34 of Meteolabor AG. The components are labeled and described in section 4.1.2.

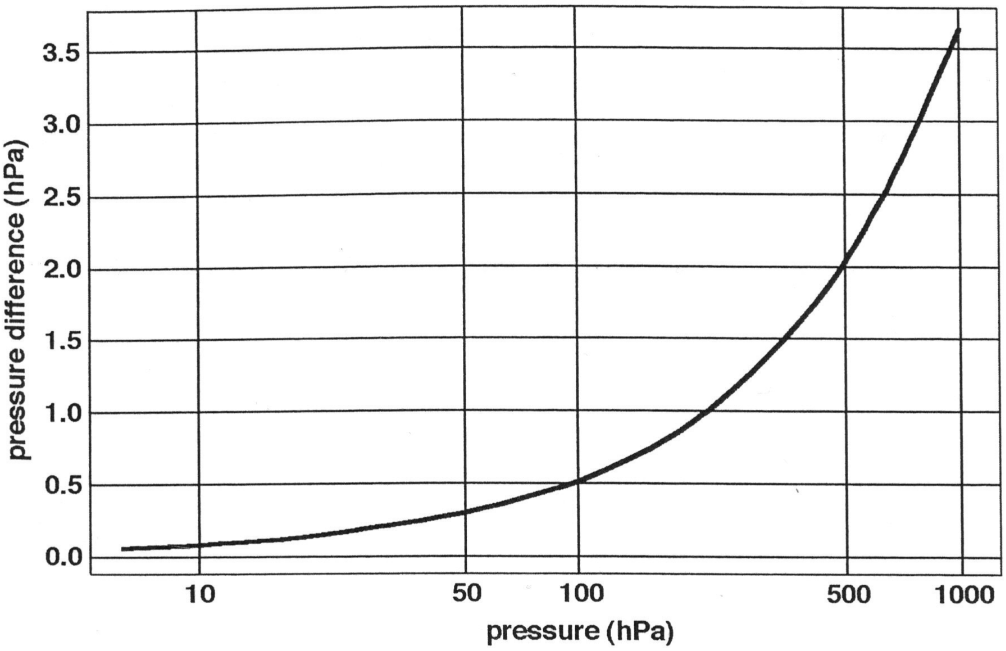

Figure 4.3: Absolute pressure differences calculated for a uncertainty of $\Delta T = 0.1$ K of the water boiling temperature.

4.1.3 Controlling unit

To combine the two data sets from the spectrometer and the radiosonde a special controlling unit was developed. The microprocessor based controlling unit offers two ports for the incoming data. The controlling unit evaluates, synchronises, and prepares the data sets for transmission.

The fixed data rate of the radiosonde of 2400 baud limits the transmission of optical data to 1000 channels for a 10 s interval. This time interval relates to a vertical resolution of 50 m, assuming an average ascending rate of 5 m s^{-1}, which is typical for balloon ascents. 1000 channels are selected out of the original 2048 (see section 4.1.1) prior to the start depending on the scientific request. The channels can be selected with a PC based configuration tool (Figure 4.4). The PC or laptop for configuration has to be connected at port 1 of the controlling unit.

All spectra detected within the described 10 s interval are compared and one spectrum is selected as being representative for the 10 s time period. Selection criterium is that the chosen spectrum shows the highest irradiance values without any saturation.

The controlling unit adapts the integration time of the spectrometer for the case that one or more channels show saturation for incoming photons. If a saturation is detected in three consecutive measurements, the controlling unit will decrease the integration time in predetermined steps from 255 ms down to 20 ms.

The flow diagramme Figure 4.5 shows the evaluation process for one measured spectrum. At first it is checked for saturation. If no saturation is detected the spectrum gets the status OK, if saturation is detected the spectrum gets the status not ok (NOK). Secondly, the comparison with the former spectrum is made and it is decided wether the former spectrum stays in the memory of the controlling unit or the new spectrum will come into memory. After a ten seconds intervall the actual spectrum in the controlling unit memory is the representative spectrum for that time period.

The optical and meteorological data sets are synchronised by chosing the meteorological measurements taken with the smallest time delay to the representive optical spectra.

The controlling unit can additionally be equipped with a mass storage (SD-card, 128 Mb) to store all measured data, including all 2048 spectrometer channels and all disregarded spectra from the evaluation process. The unreduced data set can be analysed if recovering of the sonde is possible.

The sonde can be operated in the calibration mode. In this mode, the adaption of the integration time is disabled. Measurements are undertaken with a fixed integration time, which is selected prior to the measurement. For activating the calibration mode and the selecting of the integration times, the communication between a controlling PC and the sonde is operated via the user interface, see Figure 4.4. The data is transferred via a cable connection with 19200 baud. The higher transmission rate allows the transfer of all 2048 channels, all measured

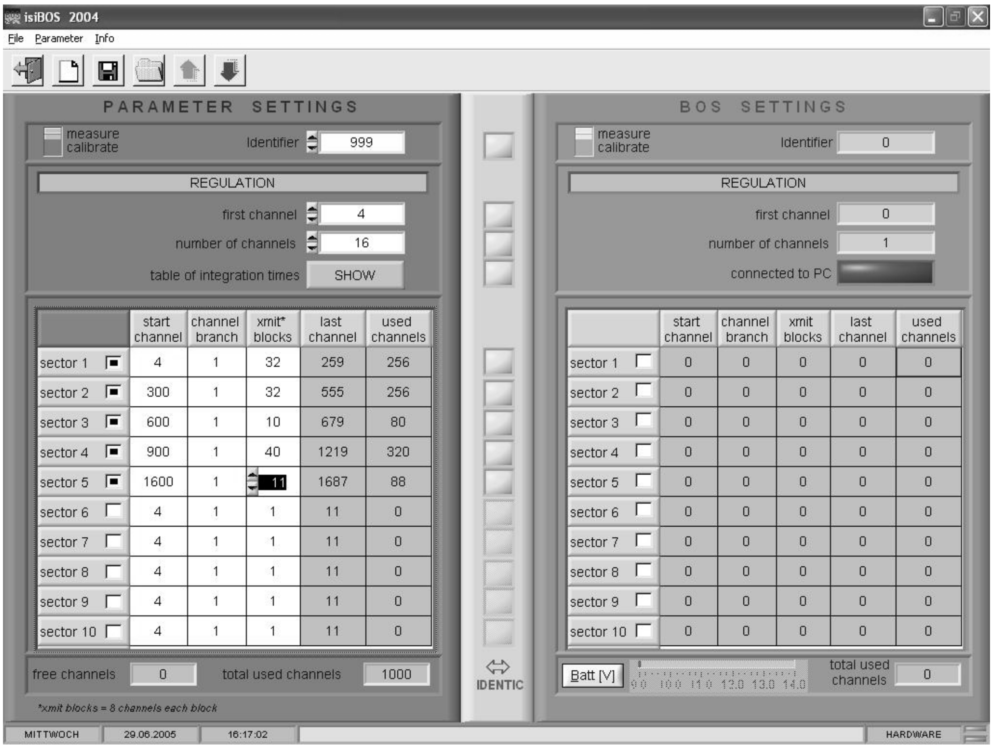

PARAMETER SETTINGS

measure / calibrate

Identifier: 999

first channel: 4

number of channels: 16

table of integration times: SHOW

	start channel	channel branch	xmit* blocks	last channel	used channels
sector 1 ☒	4	1	32	259	256
sector 2 ☒	300	1	32	555	256
sector 3 ☒	600	1	10	679	80
sector 4 ☒	900	1	40	1219	320
sector 5 ☒	1600	1	11	1687	88
sector 6 ☐	4	1	1	11	0
sector 7 ☐	4	1	1	11	0
sector 8 ☐	4	1	1	11	0
sector 9 ☐	4	1	1	11	0
sector 10 ☐	4	1	1	11	0

free channels: 0

total used channels: 1000

*xmit blocks = 8 channels each block

BOS SETTINGS

measure / calibrate

Identifier: 0

first channel: 0

number of channels: 1

connected to PC

	start channel	channel branch	xmit blocks	last channel	used channels
sector 1 ☐	0	0	0	0	0
sector 2 ☐	0	0	0	0	0
sector 3 ☐	0	0	0	0	0
sector 4 ☐	0	0	0	0	0
sector 5 ☐	0	0	0	0	0
sector 6 ☐	0	0	0	0	0
sector 7 ☐	0	0	0	0	0
sector 8 ☐	0	0	0	0	0
sector 9 ☐	0	0	0	0	0
sector 10 ☐	0	0	0	0	0

total used channels: 0

MITTWOCH 29.06.2005 16:17:02

Figure 4.4: Screen shot of the user interface for the controlling unit. On the left side 10 channel sectors can be chosen with a maximum sum of 1000 channels. In the upper left corner it can be switched between calibration and measurement mode. The table of integration time can be displayed with the SHOW button. The table can then be edited. By pressing the upward pointing arrow in the menu the settings are transferred onto the controlling unit and displayed on the left site.

spectra, and all meteorological data. In this mode the data is not preanalysed by the controller according to Figure 4.5.

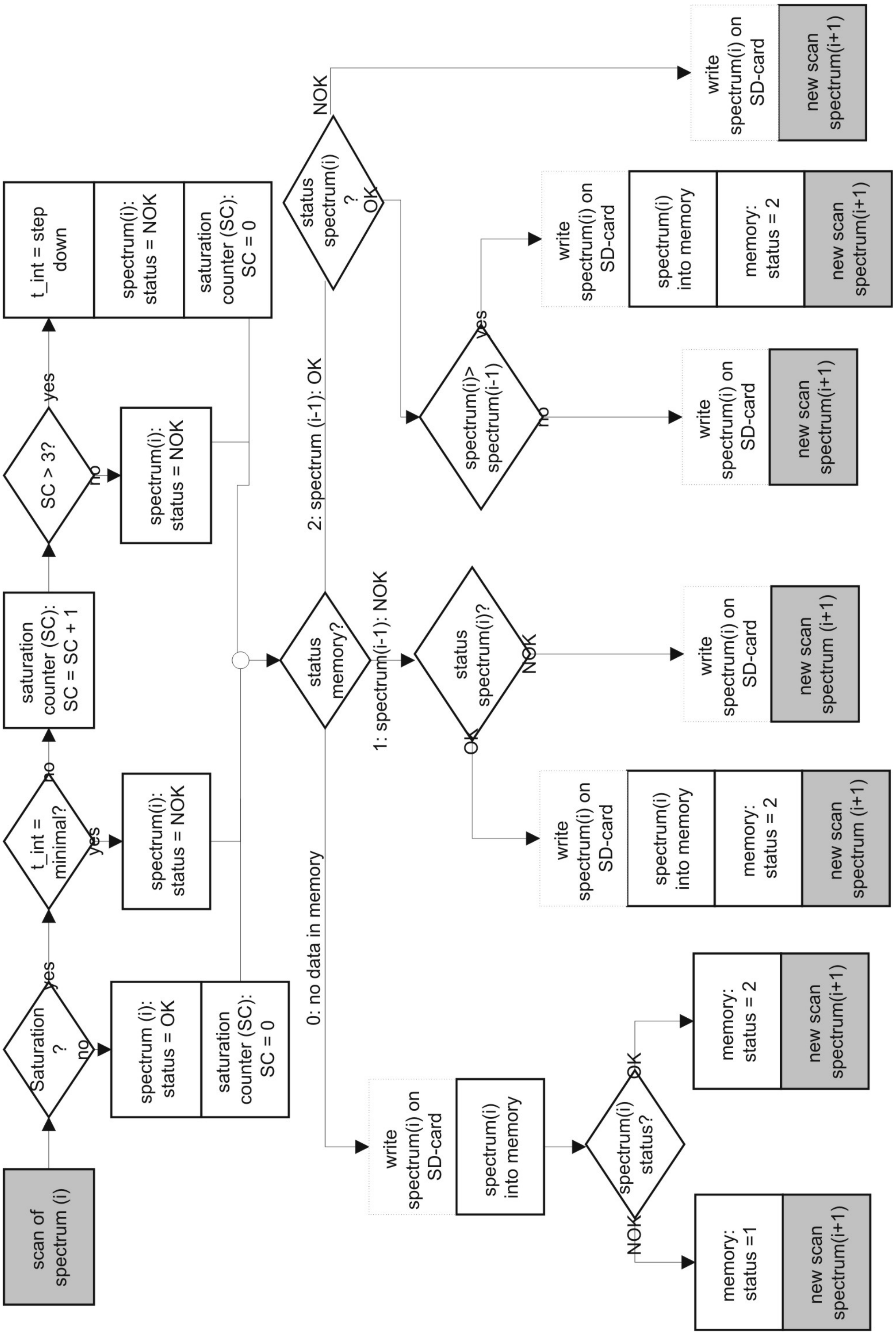

Figure 4.5: Flow diagramme of the evaluating process of the scanned spectrum in the controlling unit. After finishing the process at one of the grey shadowed steps, the process is repeated as long the 10 s measurement interval last. Optional steps are framed with a dashed line

4.1.4 Overall sensor design

In Figure 4.6 the data flow in the sonde is schematically illustrated. The meteorological data set of the radiosonde is transferred to port II of the controlling unit. The measured spectrum is transferred to port I of the controlling unit. Commands from the controlling unit to the spectrometer, such as the change of the integration time, are sent via the same connection (port I)

Before the measurement, the controlling unit can be initialisised by choosing the operation mode (calibration or measurement) and defining the channel sectors via the user interface software. For that purpose a Laptop or PC is connected to port I of the controlling unit. In the calibration mode, the data output can be read out via a cable connection directly at port II of the controlling unit. In the measuring mode the controlling unit evaluates the spectral data as described in section 4.1.1 and synchronises them with the meteorological data. The complete data set is then transferred to the transmitter of the radiosonde and transmitted to the groundstation. The groundstation contains an antenna (yagi-antenna), a receiver (AR8600), an interface (ARGUS 37), and a laptop with the data recording software. The interface belongs to the radiosonde system and decodes the data. The software was developed for reading out the data set of the new sensor. It also displays the meteorological data and the spectral data in real time. Trace gas profiles are analysed seperately after the ascent with a different software programme.

The complete system measures 345 x 210 x 180 mm. The overall weight of the sonde is 1.7 kg. The housing consists of two single radiosonde boxes.

The first box contains the radiosonde part and its power supply, the other is adapted to keep the spectrometer, the controlling unit and their power supply, see Figure 4.7. Controlling unit and spectrometer consume a current of 80 mA. Because of possible electromagnetical interferences, between the controlling unit and the radiosonde electronics a shielding is necessary. For the first generation of sondes, that was constructed with an aluminium foil wrapped around the controlling unit box. For the second generation, a small aluminium box is used as a casing for the spectrometer and the controlling unit.

For balloon-borne measurements with the sonde, additional equipment is needed. Inside the polystyrene box 5 - 7 water bags are placed. The waterbags slow down the cooling process during the ascent through the atmosphere.

A parachute slows down the descend rate and subsequently reduces the impact speed of the sonde. That minimalises the danger of damages caused by the sonde and also protect the sonde itself against breakage. During the first minutes after launch, an unwinder is slowly extending the distance between sonde and balloon to 100 m. Ca. 120 cm above the sonde a small black disc is mounted in order to shield the entrance optics against any reflections from the balloon. Figure 4.8 shows the entire payload.

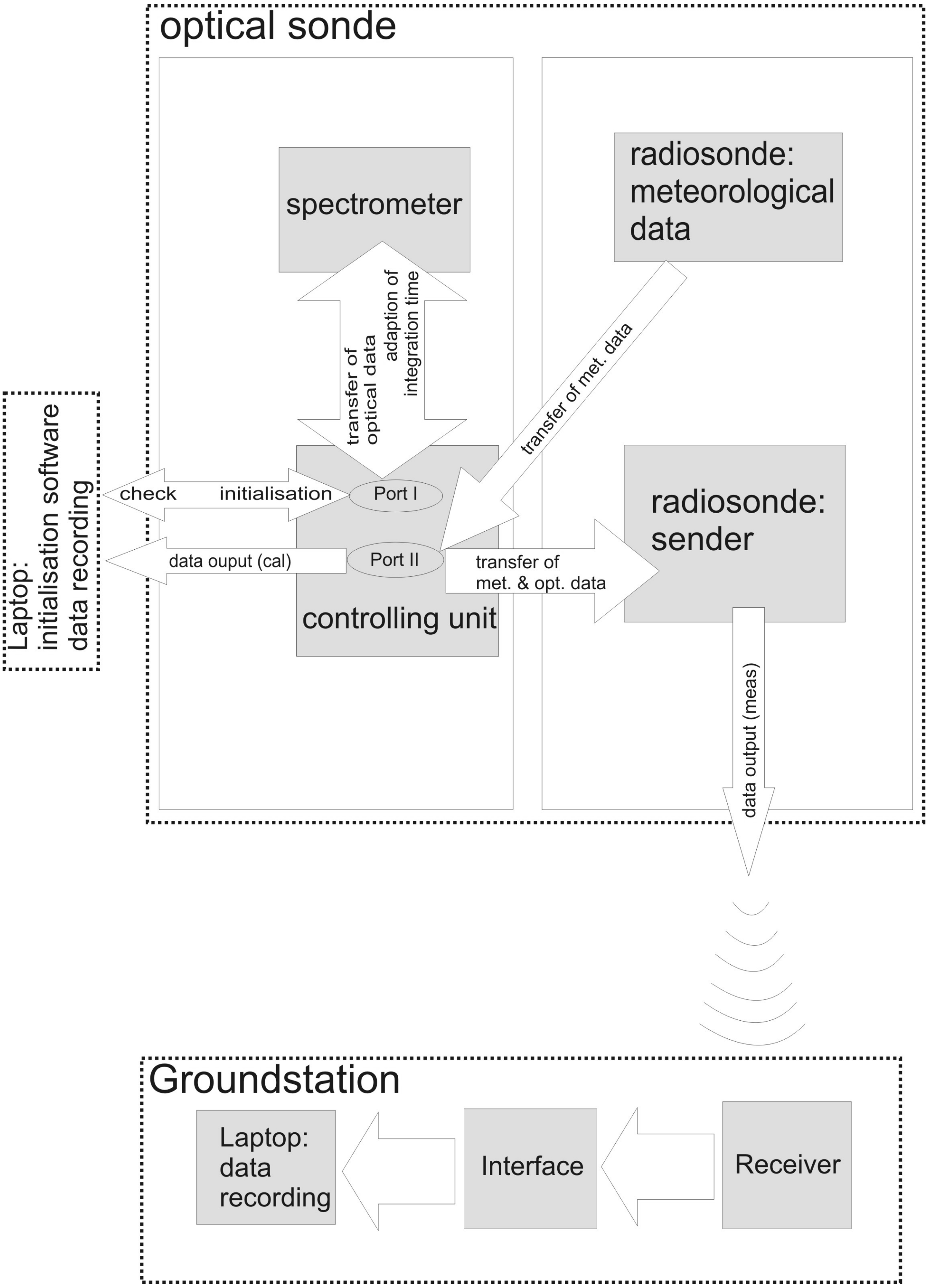

Figure 4.6: Schematic illustration of the data flow in the new sonde. The right box contains the radiosonde units: meteorological sensors and radio transmitter. The left box contains the controlling unit and the spectrometer.

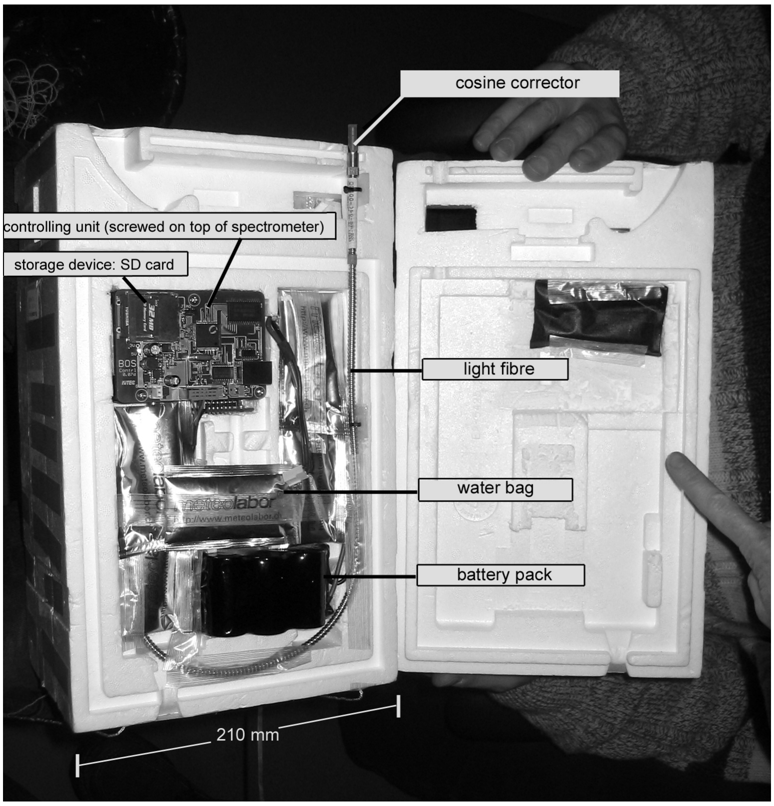

Figure 4.7: Photograph of the spectrometer and the controlling unit in the PIOS sonde.

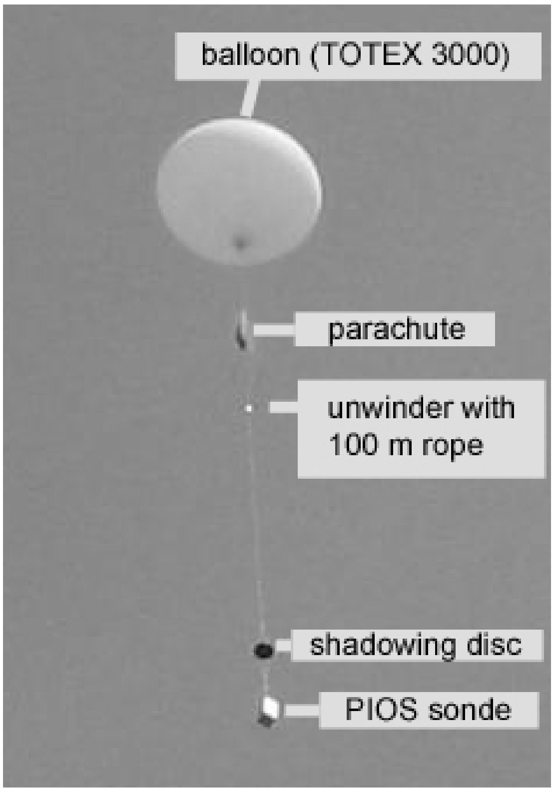

Figure 4.8: Photograph of the payload, including the sonde, the shadowing disk, the parachute, and the unwinder.

4.2 Sounding procedure

The preparation time of the sonde takes about 1 hour. It starts with the initialisation of the radiosonde with the radiosounding-system software. The hypsometer has to be filled with water and activated. The correct data flow of all meteorological instruments has to be checked. The sounding frequency and the signal strength of the transmitter will be selected. Then the radiosonde will be disconnected from the cable and the data are received via the radio receiver. Eventually, a fine tuning at the receiver is necessary to get an optimal signal.

The data are displayed at the groundstation. The correct transmittance of the meteorological data set and the spectra can be checked. Water bags are placed into the sonde. It is closed and secured with tape. The sonde will be placed outside now in order to acquire a GPS-position.

Now the sonde measures the GPS-position, the solar spectrum and the meteorological data. The integration time will be automatically adapted to the suitable time which does not cause any saturation in the spectrum. It is recommended to take an actual dark spectrum and perform a wavelength calibration measurement in order to have an actual characterisation of the sonde.

The launching equipment (parachute, unwinder, shadow-disc) is attached and the sonde is ready for launching. Connected to an external power supply, the sonde can wait until the start conditions without consuming battery power.

Before the launch, the sonde has to be disconnected from the external power and will be automatically switched to the internal power supply. Status of the batteries and overall data flow should be checked just before launch.

Chapter 5

Characterisation of the PIOS instrument

The optical sensor in the PIOS sonde is a miniature grating spectrometer. Ten of these spectrometers were optical characterised. The main aspect of the laboratory measurements was the characterisation of the sonde for the temperature changes, expected during a balloon ascent.
The spectrometer has its own unit for the measured irradiance. It detects the signal in counts per integration period, proportional to the incoming photons in this period. Since no absolute calibration was performed, the counts can not be converted into photons. The selected integration time varies between the measurements. In the following the measured irradiance is given in arbitrary units (a.u.).

5.1 Optical resolution and instrument's slit function

The spectrometer covers the wavelength range between 200 and 850 nm. The dispersed signal in the spectrometer is detected with a CCD array, consisting of 2048 channels. The dispersion of the spectrometer calculates to 0.32 nm channel^{-1}. With the information of the channel resolution of 4.2 channels (company information at *http://oceanoptics.com/technical/opticalresolution.asp*) the optical resolution is 1.34 nm full width of the half maximum (FWHM). In the laboratory, the bandwith was determined from measurements of spectral lines of a pencil style spectral calibration mercury argon lamp. The signal of the line at 296.73 nm detected with the spectrometer is shown in Figure 5.1. The FWHM can be determined with 1.2 nm for this wavelengh. The wavelength dependance of the bandwidth was checked with all detectable lines from the mercury argon lamp between 253.6 and 615.0 nm. Within this wavelength range the bandwith changes slightly but does not exceed the FWHM given by the company.
The instrument's slit function was also determined from the detected signals of

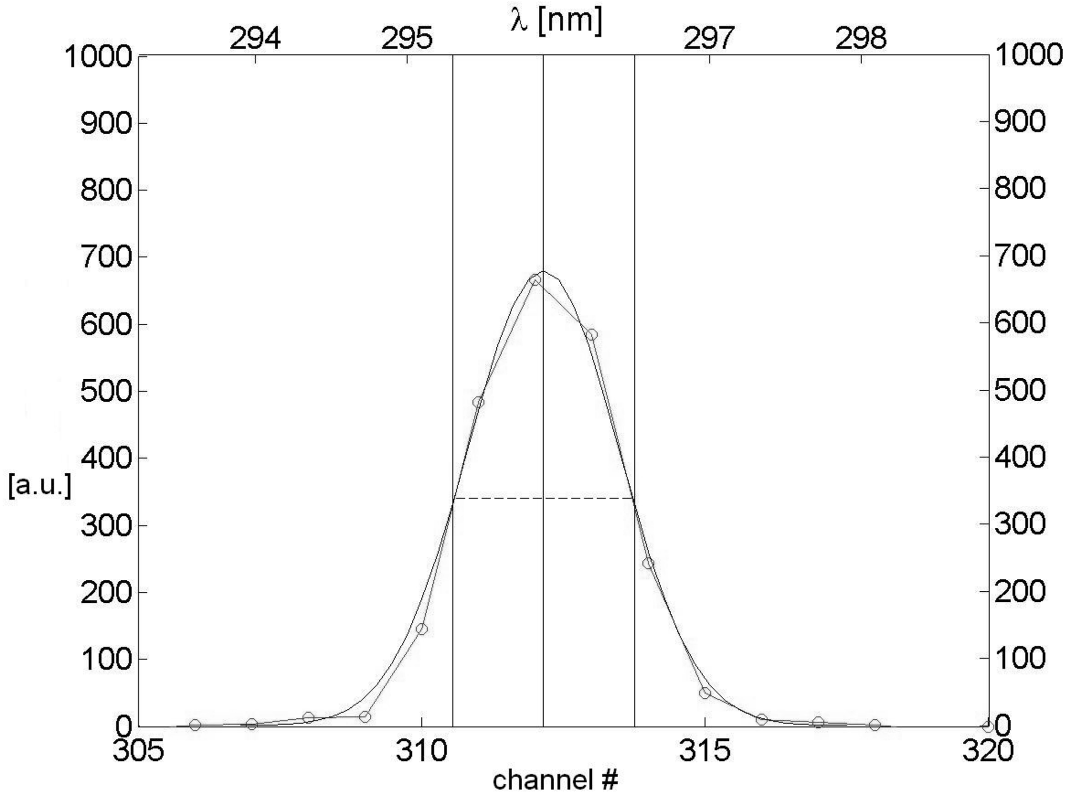

Figure 5.1: Measured signal of the spectral line at 296.73 nm (red). The dashed line illustrates the FWHM of the measurement. Optical resolution of the spectrometer. The black line is the approximated instrument's function.

the spectral lines of the mercury argon lamp. It was approximated with a normal probability density function around the wavelength of the spectral line λ_0:

$$F(\lambda_0, \lambda) = \frac{1}{\kappa \cdot \sqrt{2\pi}} \cdot \exp\left(\frac{-(x-\lambda_0)^2}{2\kappa^2}\right) \tag{5.1}$$

With $\kappa = 0.5\,\text{nm}$ the best fit to all measured spectral lines was achieved. Equation 5.1 can be calculated for any wavelength λ_0. Multiplied with the signal strength of a known signal at λ_0 it will result in the signal detected by the spectrometer at wavelength λ. The instrument's slit function will be used for the calculation of the effective absorption cross sections or the convolution of the extraterrestrial spectrum.

5.2 Dark current

A typical dark current (dc) is shown in Figure 5.2. It was measured with spectrometer #3658 with an integration time of t_{int} = 250 ms at 26° C in a climate chamber. The average dark current corresponds to dc = 105 a.u. with a standard deviation of ±2 a.u.. The dark current offset is highly dependent on temperature. The 10 spectrometers checked in the laboratory showed a linear relationship between the mean dark current and the temperature of about 5 a.u.K^{-1} (Figure 5.3). The linear regression lines, the correlation coefficients R^2, and the root mean square deviations (RMSD) were calculated. For spectrometer #3658 a slope of -5.39 a.u. K^{-1} ($R^2 = 0.997$, RMSD=2.09) and for spectrometer #1932 a slope of -5.53 a.u. K^{-1} ($R^2 = 0.994$, RMSD=3.60) were calculated. The slope for spectrometer #3673 was calculated with -5.01 a.u. K^{-1}. The calculation is based on two measurements at two different temperatures.

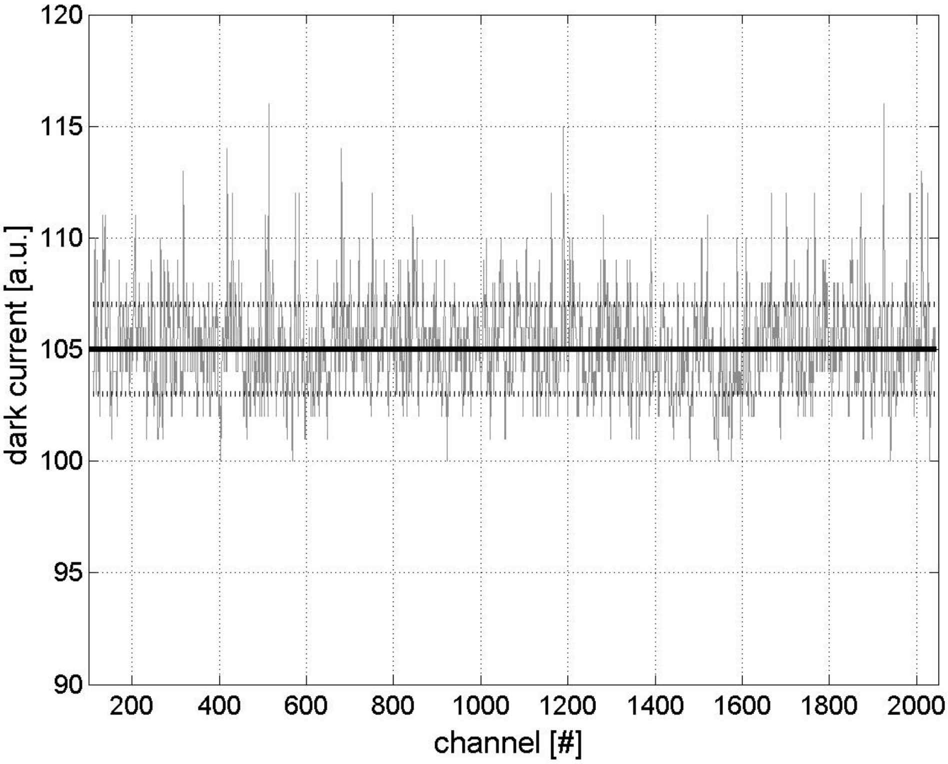

Figure 5.2: Typical dark current of spectrometer # 3658. The solid line marks the mean dark current of 105 a.u., the dotted lines are the standard deviation of ±2 a.u.

The temperature induced dark current changes can be corrected by using the laboratory results. Alternatively, the wide wavelength range of the used spectrometer offers the possibility for inflight correction. The UV-C wavelengths at the beginning of the detected spectrum (≤ 250 nm) are in fact dark channels for the miniature spectrometer, as the solar radiation at these wavelengths becomes negligible in the stratosphere. In order to establish how well the mean dark current is represented by the dark current of a single channel, the temperature dependency of the mean dark current was compared with the dark current detected at channel #1. Almost identical slopes were found for both cases. Figure 5.4 shows the temperature dependence of the mean dark current and the representative single channel dark current and their differences for spectrometer #3658. The differences are less than ±1 counts. This is smaller than the standard deviation (±2 a.u.) of the mean dark current.

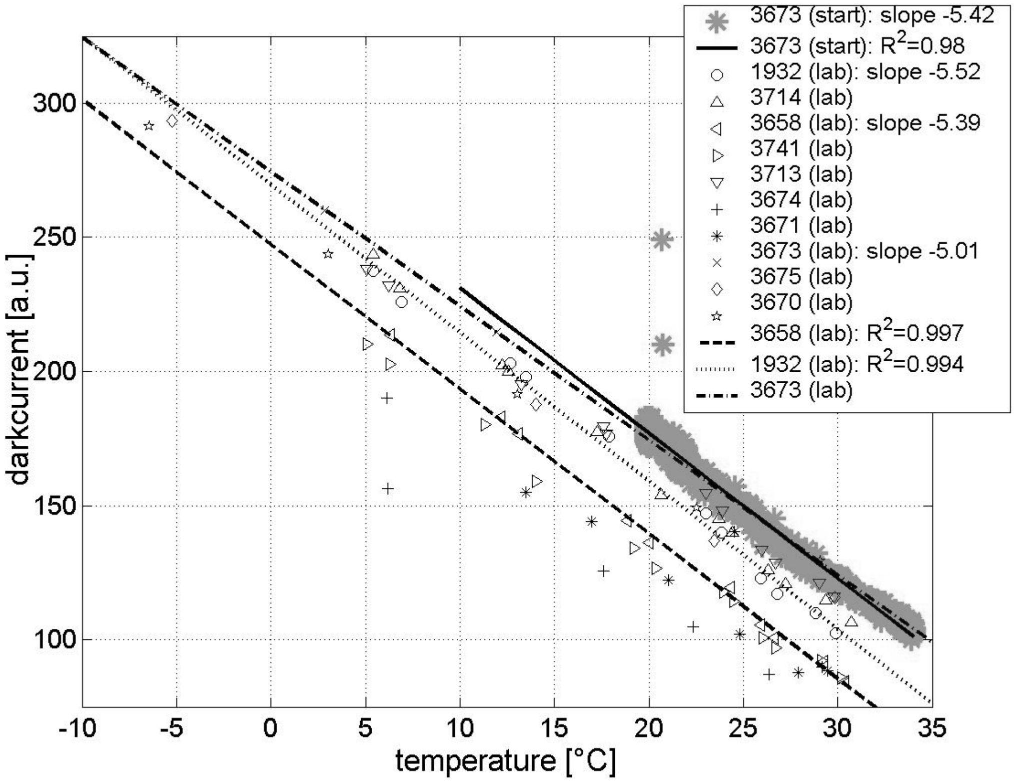

Figure 5.3: Dark current versus temperature for all spectrometers, plotted with the symbols. For clarity only the regression lines of the spectrometers #3658, #1932, and #3673 calculated from the laboratory measurements are exemplarily added. The green asterisks mark the measured dark currents at channel # 1 for spectrometer #3673 during a flight. the solid line is the calculated regression line.

The laboratory measurements showed that the dark current detected at channel #1 represents the mean dark current. During field-measurements, however, channel #1 is exposed to the solar irradiance entering into the spectrometer, but due to its short wavelength (≈ 250 nm) it can be assumed as a quasi dark channel.

Figure 5.3 shows in addition to the laboratory measurements the detected signal of channel #1 taken during the flight from spectrometer #3673. The calculated linear regression line for the relationship of the dark current to the temperature has a slope of -5.4 counts K^{-1} ($R^2 = 0.98$, RMSD=3.79), which is in good agreement with the laboratory measurements of all spectrometers.

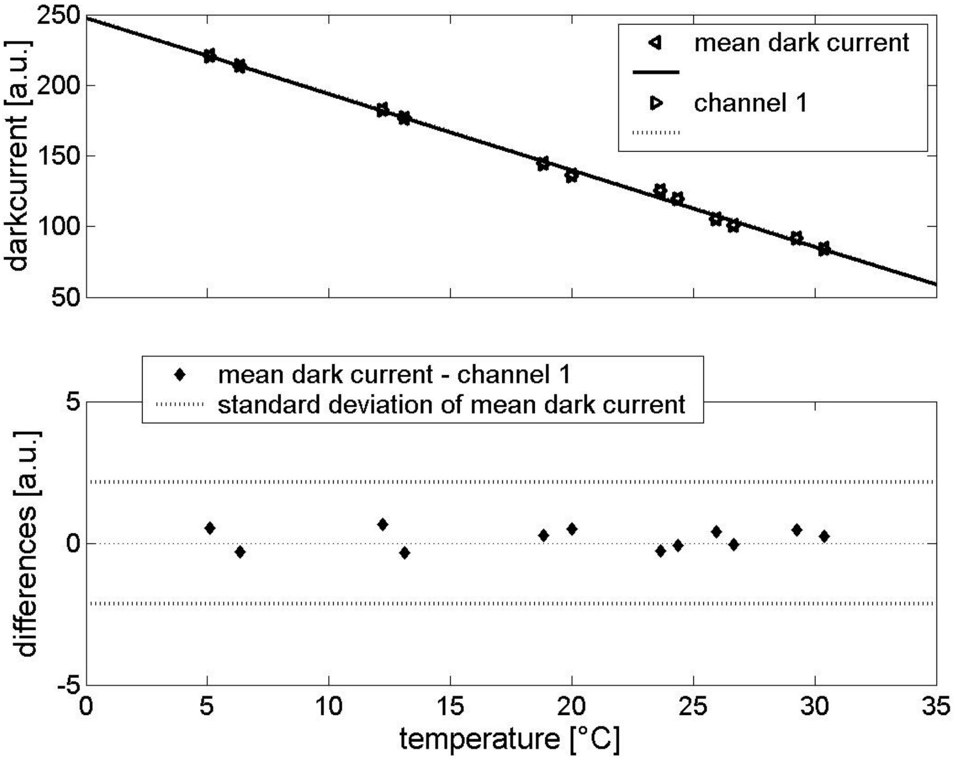

Figure 5.4: Upper panel: dark current versus temperature, comparison of mean dark current and the dark current at channel #1. Lower panel: differences between the representative dark current and the mean dark current. The standard deviation of the mean dark current of all channels ±2a.u. is plotted with dashed lines

Therefore, the inflight dark current correction based on the measurements of channel #1 can be applied instead of using the laboratory results. By doing so the correction is independent from any changes of the dark current behaviour over time, which may occur during transport or storage. Furthermore, preflight laboratory measurements of the temperature dependency of the dark current become obsolete.

5.3 Spectral calibration

After wavelength calibration, the relationship of the individual wavelength (λ) to channel (ch) can be expressed by a third-order polynomal with four independent coefficients ($c_0, ..., c_3$):

$$\lambda(ch) = c_0 + c_1 \cdot ch + c_2 \cdot ch^2 + c_3 \cdot ch^3. \tag{5.2}$$

For the wavelength calibration a pencil style spectral calibration mercury argon lamp is used as the standard radiation source.

The spectrum of the light source is detected with an integration time, that allows to detect 8 to 11 peaks without any of them is showing saturation. For each peak the channel position of the maximum is identified. Generally the signal maximum is not exactly at a channel position, but inbetween two channels. Therefore, the position is determined by a spline interpolation of the detected peak signal.

The exact wavelengths of the spectral lines of the light source are known. The polynom Equation 5.2 is fitted to match the determined channel positions for all lines in a least square sense. The resulting coefficients ($c_0, ..., c_3$) gives the actual wavelength calibration.

The determined wavelengths drift slightly as a function of time and environmental conditions, Ocean Optics (2003). This necessitates a wavelength calibration before each launch.

In contrast to the slow storage drift, the temperature changes during the flight cause a fast wavelength drift. To compensate for this laboratory tests with all ten spectrometers have been carried out. Each spectrometer was placed in a climate chamber and at different temperatures the spectrum of the light source was measured. Typically, a temperature range of 20 - 30 K was covered. Temperature dependent wavelength calibrations were calculated from this measurements.

These tests showed that different spectrometers have slighthly different drift behaviours and that differences exist within the spectrum of single spectrometers. Figure 5.6 shows an example of the drift behaviour for channel #420 of spectrometers #3673 and #3658 as measured in the laboratory.

The results allow to calculate a temperature-drift function, however, this calculation would not take the unknown influence of the storage drift into consideration. This implies that an inflight correction possibility should be established.

For the analysis of trace gas absorption, high wavelength accuracy is necessary, because absorption coefficients can change drastically with the wavelengths. This would mean that small wavelength errors result in large errors in the calculations of the absorbing trace gas amounts. A method developed by Huber et al. (1993) was used to determine the wavelength shift for each spectrum measured during the balloon-flight. This method is based on the convolution of the highly resolved extraterrestrial spectrum $I_0(\lambda)$ with the instrument's slit function (Equation 5.1). The highly resolved extraterrestrial spectrum (from Kurucz (1984), updated by Chance and Spurr (1997)) and the convolved extraterrestrial spectrum is shown in Figure 5.5.

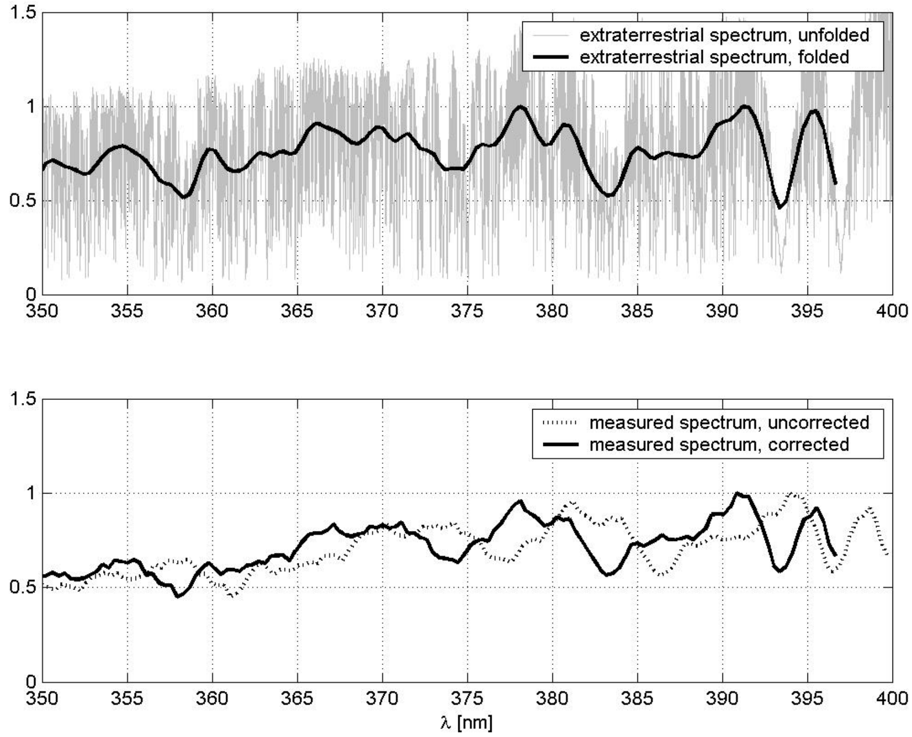

Figure 5.5: Upper panel: The extraterrestrial radiation with a resolution of 0.01 nm, grey line, and folded with the spectrometer's slit function, black line.
Lower panel: The dotted line is the measured spectrum at maximal height with the laboratory wavelength calibration (it was not performed directly before the start). The same spectrum with corrected wavelengths is drawn with the solid line. The y-axis shows normalised values of the spectral irradiance.
Note: Absolute differences in the irradiance between the extraterrestrial and measured spectrum are due to instrument's characteristics and do not influence the correction of the wavelength drift.

Each measured spectrum is compared with the convolved extraterrestrial spectrum. The initial channel wavelength relationship is determined prior to the start by the wavelength calibration. For each measurement during the flight the wavelengths for the channels are shifted in steps of 0.1 nm and the resulting spectrum is compared with the extraterrestrial spectrum. The optimum correspondence of the Fraunhofer structures is determined, thus giving the new wavelengths for the channels. During the laboratory measurements differences were identified for different parts of the spectrum. This necessitates that the Fraunhofer comparison are performed separately for wavelength intervalls of about 50 nm. Figure 5.5 shows the measured spectrum versus the wavelengths, determined from the wavelength calibration performed before the flight, and the shifted spectrum after the Fraunhofer correction. The structures of the corrected spectrum are in good agreement with the extraterrestrial spectrum

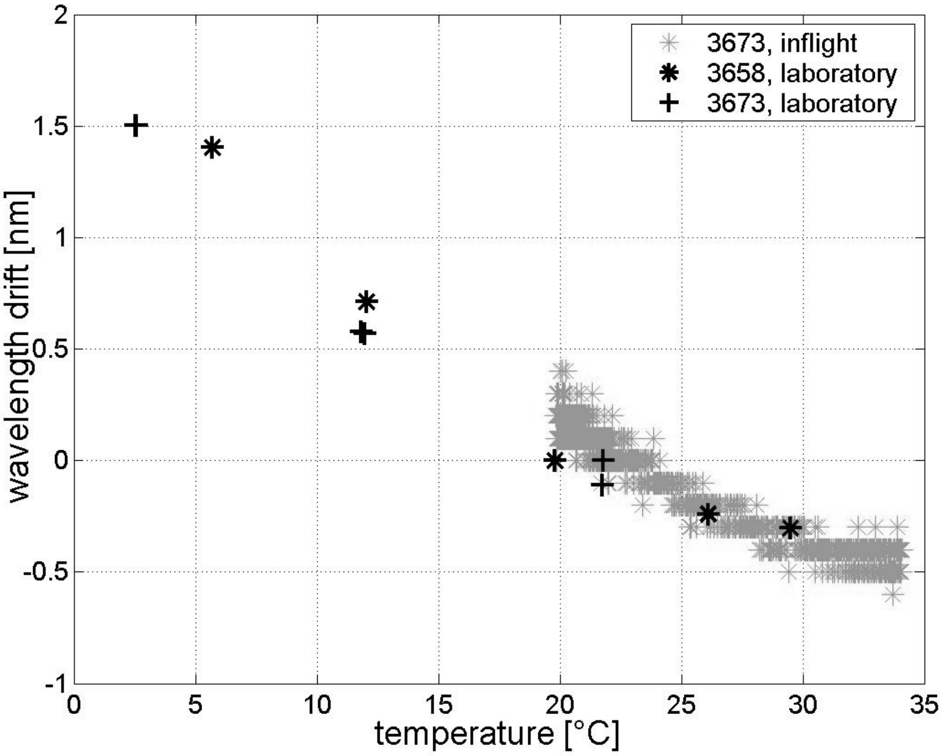

Figure 5.6: Wavelength drift of channel 420 in the laboratory (spectrometers 3658 and 3673) and during the flight (spectrometer 3673). For the laboratory measurements the wavelength calibration was done for different temperatures with a mercury argon light source. For the flight measurements the measured spectra were shifted against the Fraunhofer spectrum.

Figure 5.6 shows the resulting drift behaviour of channel #420 after the Fraunhofer correction for the flight measurements of #3673. Evidently this inflight correction method shows comparable dependency on temperature changes as the laboratory results obtained from the laboratory wavelength calibrations at different temperatures. The wavelength detected by a selected channel is decreasing with increasing temperature. Towards higher temperatures the drift decreases. The typical temperature change of the spectrometer during a flight is less than 15 K, due to the insulating effect of the polystyrene housing. This results in a wavelength drift of less than 1 nm. This is shown in Figure 5.6 for the sample channel of spectrometer #3673.

5.4 Radiative calibration

The strength of the signal detected by the spectrometer changes with temperature. The effect is different for each spectrometer and shows a smooth variation with wavelengths. In Figure 5.4 the detected signal of a constant light source (tungsten-halogen, 150W) measured at three different temperatures of the spectrometer is shown. The measurements were performed in the climate chamber which allowed for controlling the ambient temperature of the spectrometer. Because of the characteristics of the used light source, which has a rather weak signal in the UV wavelength range, the measurements were only analysed for the visible region of the spectrum (400 - 600 nm).

For the trace gas analysis of the irradiance only ratios of irradiances measured at two different wavelengths will be used (describtion follows in chapter 7). Therefore, the influence of temperature changes on the ratio was analysed. Figure 5.4 shows the measured signal in the range between 400 to 600 nm normalised with the measured signal at wavelength $\lambda = 500$ nm for the three temperatures.

The relative differences between the normalised signals measured at two different temperatures are calculated. The temperature differences are (1) $\Delta(T) = 29^\circ \text{ C} - 18^\circ \text{ C } = 11$ K, and (2) $\Delta(T) = 29^\circ \text{ C} - 6^\circ \text{ C } = 23$ K.

As expected, the relative differences are smallest for wavelengths close to 500 nm. These relative differences are compared with the relative error of the irradiance measurement at 29°C. For the large temperature difference of 23 K, the differences of the signal ratios for the range of 480 to 520 nm are always below the relative error of the signal at 29°C. For the smaller temperature difference of 11 K, the wavelength range for which the differences between the ratios are below the relative error of the signal at 29°C, increases to 470 to 550 nm.

This shows that for the visible part of the spectrum, the temperature dependent variation of the measured irradiance is a negligible effect on the irradiance ratios calculated of wavelengths not differing more than ±20 to ±30 nm from each other. One can only assume that this is also valid for the UV-range of the spectrum, which was used for the ozone analysis. The wavelength pairs which will be used in the trace gas analysis (chapter 7), differs typically by 20 nm, which is inside the described tolerance. This implies that the temperature influence on the wavelength ratios can be neglected

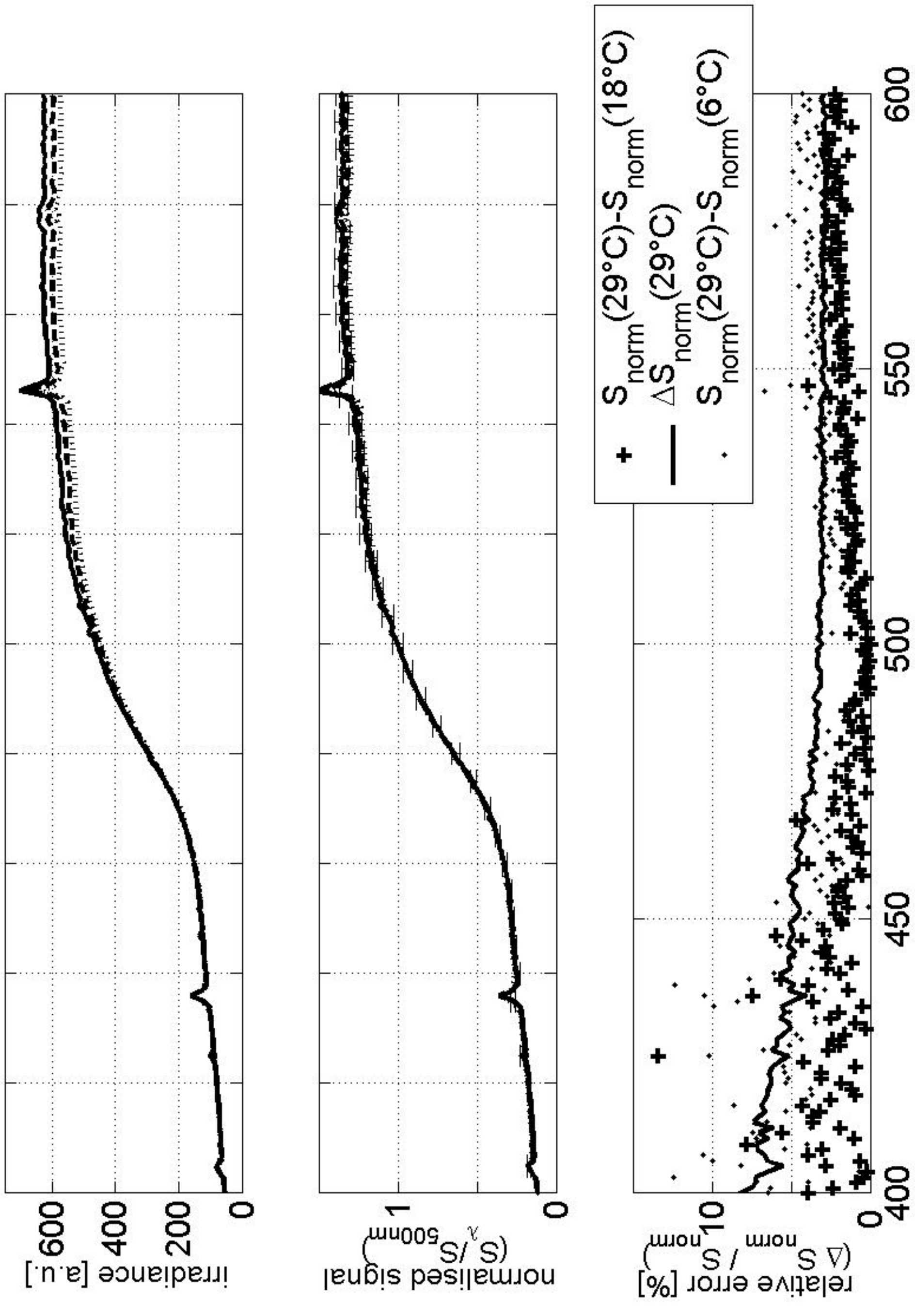

Figure 5.7: Temperature dependence of the measured signal strength. Upper panel: detected signal from a continuous light source at various temperatures. Medium panel: normed signal from a continuous light source at various temperatures. Lower panel: differences (relative) between normalised signals measured at various temperatures compared with the relative uncertainty of the signal measured at one temperature.

Chapter 6

Description of the measurement campaigns and technical results

Twelve flights have been carried out with the new sounding system. Between the flights, the system was continously improved.

The first three flights in Lindenberg in the beginning of 2004 were planned mainly as technical flights in order to test and improve the overall sensor design. The renewed system was launched four times during the measurement campaign at the Koldewey-Station in Ny-Ålesund, Svalbard, in June 2004. The obtained data were compared with the data of the routine electrochemical sonde of the Koldewey-Station. With the experiences of this measurement campaign, some further technical improvements were applied. Five sondes of the final type were launched during the recent measurement campaign at the Meteorological Observatory in Hohenpeißenberg in July 2005. During this campaign, no severe technical problem occured and all five starts were performed successfully. Therefore, it could be confirmed that the new sounding system has reached a state, where technical problems are minimised and successful measurements can be guaranteed.

6.1 Technical flights at the Meteorological Observatory Lindenberg

The first test flights with the new sonde were carried out at the Meteorological Observatory (MO) of the Deutscher Wetterdienst (DWD, german weather service) in Lindenberg, Germany. The prototype of the sonde PIOS A was started in January 2004 in order to check the overall functionality. After that flight, some technical details were changed and two improved sondes were launched in May 2004, PIOS B and C.

Figure 6.1: The balloon-preparation hall at the Meteorological Observatory Lindenberg. The balloon to the right carries the PIOS sensor. The left balloon carries the ECC-sonde.

6.1.1 Meteorological Observatory Lindenberg

The village of Lindenberg is located about 60 km South-East of Berlin at 52.18° North and 14.06° East. The Meteorological Observatory Lindenberg (MOL) was founded in 1905. At that time systematic measurements of vertical profiles of wind, temperature and humidity were carried out with tethered balloons and kites. These measurements and their scientific analyses contributed to a description of the vertical structure and the processes in the troposphere and lower stratosphere. Today, Lindenberg is an aerological station, with four regular radiosonde launches per day. Once a week, an electrochemical ozone sensor is started. The measurement programme is extended by numerous instruments detecting various atmospheric parameters. Lindenberg is also a reference station for worldwide radiation measurements and provides cloud- and radiation data for satellite validation.

6.1.2 Technical status and improvements

The controlling unit of the prototype sonde complied mainly with the description given in section 4.1.3. The communication rate between the spectrometer and the controlling unit was set to 38.4 Mbaud. The integration time of the spectrometer was reduced stepwise from 1000 to 20 ms.

A major difference to the current version of the sonde was the power supply. The prototype (PIOS A, 21.1.2004) was equipped with one battery pack (10.5 V), connected to the controlling unit. The energy was distributed further to the spectrometer and to the radiosonde. In the second sonde (PIOS B, 12.5.2004), the battery pack (10.5 V) was connected to the radiosonde unit instead. From there power was distributed to the controlling unit and the spectrometer. The PIOS B solution resulted in a more stable voltage at the GPS-receiver. The GPS-receiver reacts very sensitive on short-time power oscillations. In the third sonde (PIOS C, 13.5.2005), the power was provided by two battery packs: (1) The radiosonde was supplied by three parallel connected 9 V batteries. (2) A 10.5 V battery pack supplied the controlling unit and the spectrometer.

To avoid electromagnetical interferences between the controlling unit and the GPS-receiver of the radiosonde, a shielding of the controlling unit was realised with some aluminium foil between the two styrofoam boxes for PIOS A. For the second and third flight, the polystyrene box containing the spectrometer and controlling unit was wrapped totally in aluminium foil.

For the first flight, the data were received by the Vaisala antenna of the MOL. The antenna has eight poles, covering different directions. The best available element for signal reception is selected automatically by the telemetry receiver. For all following flights, a yagi antenna was used, which needed to be directed manually towards the sonde.

Two of the sondes (PIOS A and B) were equipped with SD memory cards.

6.1.3 Technical aspects of the flights

PIOS A, 21.1.2004

The ground test of the sonde showed a very instable GPS-signal. Therefore, a provisorily shielding was applied by using an aluminium foil between the two polystyrene boxes. Meteolabor, the producer of the radiosonde, recommended to reduce the sending power of the sonde to 13 Dbm, instead of 20 Dbm (full power).

Before the launch, the data transmission worked and a GPS-signal was received. During the ascent, the quality of the received radio signal decreased rapidly and ended in a total signal loss at 16.8 km altitude, about 70 minutes after launch. Possible reasons for the telemetry problems may be the reduced sending power, as well as the power distribution in the sonde. The size of the power supply was calculated sufficiently for the entire system and should last for several hours under normal conditions. However, the hypsometer heating device may have temporary peaks of very high power consumption, thus reducing the available power for the radio transmitter, which needs a minimum voltage of 5 V.

For the next start the power supply was connected directly to the radio transmitter of the radio sonde. The power connection of the spectrometer was realised through the controlling unit. That guaranteed stable power supply of the trans-

mitter, independent from the hypsometer behaviour.
After the flights, PIOS A and B were recovered and the SD-cards could be read out. It became apparent that due to a software failure in the controlling unit, only the transmitted data sets were stored on the SD-card and not all measured spectra.

PIOS B, 12.5.2004

Before the launch, the data transmission worked and a GPS-signal was received. During the entire ascent up to 32 km altitude and parts of the descent, a radio signal could be received. For the highest altitudes a small decrease in the data quality was observed.
Right after the launch, the GPS signal dropped out, but was received again with changing quality until 5 km altitude. From that no further GPS signal was received.

PIOS C, 13.5.2004

Tests on ground with the third sonde, gave some evidence that one reason for the unstable GPS-signal could be due to unstable power supply, caused by power consumption peaks in one of the other components. Therefore, two separated power supplies were realised in the PIOS C sonde: one for the controlling unit and spectrometer, the other supplying the radiosonde.
No GPS signal was received during the flight. The data transmission quality decreased very rapidly and total signal loss was reported in 12 km altitude, 35 minutes after the launch. No reason could be identified for the early signal loss.

6.2 Measurement campaign at Koldewey-Station, Ny-Ålesund

After the flights in Lindenberg, extended tests were performed in order to identify the GPS-problem.
Further evidence was found for the necessity of a stable power supply for the GPS-module.
Tests performed by Meteolabor in Switzerland approved the assumption of major electromagnetic interferences between the processor of the controlling unit and the GPS-receiver. It also appeared that the chosen shielding with aluminium foil is sufficient.
The GPS-receiver seemed to be very sensitive against disturbances while searching its position. Once receiving the signal it became more stable.
During the campaign in Ny-Ålesund (9.6 - 26.6.2004) four PIOS-sondes were launched.

Figure 6.2: The NDSC-Observatory and the balloon preparation hall of Koldewey-Station, Ny-Ålesund, Spitsbergen.

6.2.1 Koldewey-Station

The German Arctic research station Koldewey is located in Ny-Ålesund, 78.9°N and 11.9°E, on the main island Spitsbergen of the archipelago Svalbard. Ny-Ålesund is an international research site. It was founded as a coal mining town in the beginning of the 20th century. After two severe accidents in 1962, the mine was closed. The owner of the mine, Kings Bay Kull Company (now Kings Bay AS) remained in town and is supporting the growing research activities by providing the necessary logistics. Today more than 10 research stations from different nations are in operation. The scientific projects cover various fields of polar research.

The Koldewey-Station of the Alfred Wegener Institute for Polar and Marine Research was opened in 1991. The main focus of the Koldewey-Station is the monitoring of the polar stratosphere. The Koldewey station is a primary station of the network for detection of stratospheric change (NDSC) providing stratospheric data obtained by LIDAR, Microwave radiometer, sun/star photometer, FTIR and balloon launches. Radiosondes are started daily. During summer, an electrochemical ozone sensor is started once a week, During winter starts are carried out at least twice a week, depending on the stratospheric situation and ongoing campaigns and their needs.

Figure 6.3: Launch preparation of a polyethylene balloon: unpacking(1) and inflating(2 + 3).

Figure 6.4: Launch preparation of a polyethylene balloon: unfurling of the ballon-rest and start of the sonde.

6.2.2 High alitude polyethylene balloons

Two of the starts at the Koldewey-Station were carried out with thin-film high-altitude balloons, developed by the Institute of Space and Aeronautical Science (ISAS), Japan. The balloons are made of a very thin polyethylene film, which has a thickness of only 6 μm. The used balloon of type BT-5 has a volume of 5000m^3 and a weight of about 11kg. It is a comparable small high altitude balloon. Due to the very thin material and the resulting light weight it can reach higher altitudes ($>$ 42km) than conventional polyethylene balloons of comparable size, Okabayashi (1999).

The balloon has to be handled very carefully. Any contact with hard objects or the ground has to be avoided. The launching team has to wear gloves. With this precautions the flight preparation can be carried out by a group of 8 to 10 people at any place with power supply and access to helium.

The preparation procedure is illustrated by the photo series in Figures 6.3 and 6.4. The balloon is delivered in a cardboard box and folded in a way, that eases the inflating. Only a small part of the balloon, about one third, is first unpacked. A handle seperates that part from the rest of the balloon. On this handle the weight is attached for balancing the lifting weight. While inflating that unfolded part with helium, the rest of the balloon stays protected in the box.

As soon as the weight is lifted, the filling tube is closed and the complete balloon can be unfurled. The payload is attached and the balloon is ready to start.

6.2.3 Comparative measurements

For comparison, ECC ozone sondes were launched at Koldewey-Staion. The first was started on 11.6.2004 and is suitable for comparison with the PIOS starts I (10.6.2004) and II (12.6.2004). Two further ECC sondes were started with a short time delay of about 30 minutes after the two next PIOS launches III (18.6.2004) and IV (24.6.2004).

6.2.4 Technical status and improvements

The controlling unit remained largely unchanged. On Svalbard a recovery of the sondes was very unlikely. Therefore, the controlling unit was not equipped with SD-cards.

Because of the bad experiences with the last Lindenberg flight (PIOS C), the power supply was again provided by one battery pack (10.5 V). Endurance tests showed that the battery pack provided enough power for several hours.

Regarding the instability of the GPS-signal the following features were added before the campaign:

(1) To prevent voltage fluctuations at the GPS-unit, a dc-dc converter was implemented

(2) ferrite cores were applied for reducing electromagnetic disturbances via the connecting cables.

(3) A new step was included in the start preparation: After initialising both, the radiosonde and the spectrometer, the controlling unit is switched off again. The sonde is placed outside at a place with good GPS-satellite coverage. After a couple of minutes, the GPS-receiver has normally found its position and the controlling unit can be switched on again. In most cases the GPS-signal remained stable after this procedure.

As antenna the Yagi-antenna was used. A backup receiving unit was realised with the Vaisala antenna and Vaisala groundstation (digicora MW11).

6.2.5 Technical aspects of the flights

PIOS I, 10.6.2004

Previous ground measurements showed a stable GPS-signal. Nevertheless during the initial flight preparation a GPS-signal loss occured. The controlling unit was switched off for a couple of minutes and after restarting it, the received GPS signal was stable. It remained stable up to an altitude of 32 km. The sonde reached 35 km and the telemetry signal could be received during the entire ascent and parts of the descent without any disturbances.

PIOS II, 12.6.2004

For this sonde a stable GPS-signal was recorded during previous tests, when started with a switched off controlling unit. During the sounding preparation no loss occured and the sonde was started. Unfortunately, the GPS-signal was lost exactly during the start and could not be recovered anymore. That sonde was launched in tandem with a Vaisala radiosonde RS 90, which received a complete GPS data set for the launch. Therefore the analysis of the data set became possible. No disturbances in the data telemetry were observed.

PIOS III, 18.6.2004

PIOS III was launched with a plastic balloon, and reached a maximum altitude of 42.5 km. The GPS-receiver turned out to be very stable during previous tests. It found its position with a running controlling unit. The GPS-signal was received without any problems during the entire flight.

Since the sonde reached higher altitudes, the limit of the hypsometer was reached. It failed working at 36.5 km and caused corrupt data sets for a couple of minutes. The controlling unit turned off and restarted again.

The sonde could be observed by eye up to the maximum altitude due to clear conditions and low winds and very small horizontal movement. This allowed for optimal directing of the antenna. No telemetry disturbances occured.

PIOS IV, 24.6.2004

In contrast to PIOS III that sonde showed unstable GPS-signal during previous tests, despite identical technical design. GPS-signal was only found without a running controlling unit. Placing the sonde in an area with a slightly reduced GPS satellite coverage resulted in immediate signal loss. An additional empty polystyrene box was placed between the spectrometer box and the radiosonde, thus increasing the distance between the controlling unit and the GPS-receiver. In this way a more stable GPS-quality could be achieved.

During the flight preparation a GPS-signal loss occured. Switching off the controlling unit for a couple of minutes helped and a stable GPS signal was obtained again. The GPS was working until an altitude of 28.3km before it lost the signal again. The sonde was still ascending and reached again an altitude where the hypsometer stopped working (38 km). As the hypsometer failed, the controlling unit was switched off and remained in that state for about 30 minutes. A telemetry signal was still received but due to the malfunctioning controlling unit, the received signal was not carrying any readable information. After 30 minutes the controlling unit restarted and complete spectra were received again for another 2 hours. All measurement sensors of the radiosonde showed wrong values. Due to missing temperatures, pressure and GPS-position it was not possible to determine the maximum height of the sonde.

Figure 6.5: Meteorological Observatory Hohenpeißenberg, Germany.

6.3 Measurement campaign at the MO Hohenpeißenberg

Based on the experiences collected at Ny-Ålesund, the techniques were further optimised and five revised sondes were launched during the campaign at the Meteorological Observatory Hohenpeißenberg (MOHp), 11. - 22.7.2005.

6.3.1 Meteorological Observatory Hohenpeißenberg

Hohenpeißenberg is located about 60 km west of Munich at 47.8°N and 11.0°E. The measurement site is located at 976 m altitude. Regular meteorological observations at Hohenpeissenberg started in the year 1781. The almost uninterrupted temperature measurements from 1781 until today are the world longest temperature series from a mountain station. After the Second World War the station became an observatory. An extended measurement programme is carried out since then, including radiation-, ozone-, and RADAR precipitation measurements. Also a scientific research group was established. Today the observatory is a global station in the global atmospheric watch (GAW) network and the Dobson Calibration Center for Europe.

6.3.2 Comparative measurements

The routine sonde at the Meteorological Observatory Hohenpeissenberg is the electrochemical Brewer-Mast sonde. Parallel to all five launches a Brewer-Mast sonde was started.

Measurements with the Ozone-LIDAR requires clear sky conditions and darkness. During the campaign three nights allowed measurements: (1) 13./14.7.2005, (2) 14./15.7.2005, and (3) 17./18.7.2005.

6.3.3 Technical status and improvements

Because of the remaining unstable GPS data quality further changes were made. An aluminium hard case is shielding the spectrometer and the controlling unit, thus providing a better protection than the aluminium foil. Two separate power supplies were applied: 10.5 V for the controlling unit plus spectrometer and 9 V for the radiosonde. Both power supplies were dimensioned and tested for lasting about 10 hours.

Meteolabor changed the GPS-receiver in their radiosonde and also implemented some software changes regarding the GPS data handling. With the new GPS-device they achieved a better GPS data quality in the stand alone radiosonde, personal communication of Maag, Meteolabor (2005).

For the two last launches, PIOS VIII and IX, the flat GPS antenna was replaced by a helix GPS antenna as used at the Vaisala radiosondes.

The communication rate between the spectrometer and the controlling unit was increased to 56.8 Mbaud. That limited the maximum integration time to 255 ms, ?).

All units were equipped with SD-cards (256 MB), which stored all measurements during the flight as explained in subsection 4.1.3.

6.3.4 Technical aspects of the flights

PIOS V, 12.7.2005

Previous tests with the sonde showed a stable GPS signal. During the flight prepartion the sonde had to be initialised twice before receiving the GPS-position. During the flight the GPS signal dropped out between 2 and 6 km, and was then received stable during the ascent (maximum altitude is 35.9 km) and the descent until a height of 19 km.

The hypsometer failed below 30 km altitude. Probably due to the seperated power supplies the controlling unit was not influenced by the hypsometer drop out. The measurements of the ambient air temperature and the spectrometer's temperature show some outliers after the hypsometer stopped working.

The integration time was fixed at 255 ms.

PIOS VI, 15.7.2005

No GPS-problems occured during previous tests, the flight preparation, nor during the entire ascent. The GPS-position was followed almost until the sonde reached ground again and stopped at about 3 km altitude.

During the ascent some disturbances occured in the telemetry signal. That could be corrected by increasing the mounting angle of the antenna.

Shortly after the sonde was disconnected from the external power supply and was ready to be launched, the controlling unit dropped out. The reason was easily identified as a failure in the battery pack. A change to a new battery pack helped and the sonde could be started as planned and was working without any further problems.

The maximum altitude reached was 35 km. The sonde was recovered and returned by the finder two days later. The data on the SD card could be read out and contained a complete data set, including all spectrometer channels and all measured spectra. GPS-signal was received after the impact. The GPS-time was recorded until 23:30, twelve hours after the launch, thus proving the sufficiency of the power supply.

The integration time was fixed at 60 ms.

PIOS VII, 18.7.2005

No problems with the GPS-receiving occured during previous measurements nor the entire flight. The radio signal was received without problems. The integration time of the sonde changed between 255 and 240 ms. A maximal altitude of 35 km was reached.

PIOS VIII, 20.7.2005

The GPS signal was received without problems during previous measurements and the entire flight. The sonde was equipped with a helix antenna for receiving the GPS-signal. The average number of satellites, contacted by the sonde was sligthly larger than for the sondes with a flat antenna type. The average number of contacted satellites was between 8 and 10 for the helix antenna and between 5 to 8 for the flat antenna.

No telemetry disturbances occured.

The hypsometer showed a failure during preparation and was deactivated before launch.

On top of the diffusor a cobalt-filter was attached, to filter visible light. The integration time of the sonde changed between 255 and 247 ms. A maximal altitude of 37 km was reached.

PIOS IX, 21.7.2005

This sonde was equipped with a helix antenna. In contrast to the former sondes, no update on the GPS hard- and software was implemented by Meteolabor. During previous tests and preparation no problems with the GPS occured and a larger number of satellites were seen. The GPS stopped working at 34 km altitude.

The hypsometer worked faultlessly during the entire flight and detected a maximal altitude of about 35 km. The integration time of the sonde during the flight was between 40 and 30 ms.

6.4 Discussion

The main technical aspects of all twelve flights with the new balloon-borne PIOS sonde are summarised in Table 6.1. The main problems, which occured during the development process and their solutions are recapitulated here.

The problems with the instable GPS turned out to be the most difficult part during the development of the new sonde. Not all tested sensors behaved equally and the occuring problems were a combination of various effects. The following technical changes has been applied and improved significantly the GPS stability:

1. A stable power supply has to be guaranteed. Disturbances due to voltage oscillations were prevented by the application of a dc-dc converter.
2. The controlling unit causes electromagnetic interferences and needs to be shielded. A hard case, made of aluminium has turned out to be the best solution.
3. High frequency disturbances via the cable connections has to be blocked. This was achieved by the application of ferrite cores at the connecting cables.
4. The improvements in hard- and software of the GPS-module implemented by Meteolabor improved the signal stability.
5. The more sensitive helix formed antennas received data of a higher quality, that means receiving information of more satellites.

The PIOS IX sonde was equipped with the helix antenna and showed a larger satellite number as long as a GPS signal was received. Nevertheless, the GPS-signal got lost before maximum altitude was reached. This happened very likely due to the reason that PIOS IX was still equipped with an old type GPS-module. Telemetry problems occured mainly during the first technical tests and an insufficient power supply could be identified as the reason. A changed power distribution guarantees for undisturbed data transmittance during the entire flight.

The hypsometer was implemented in the system to guarantee uninterrupted altitude information in case of GPS failures. Due to the properties of water the altitudes with the hypsometer are limited to about 35 km altitude. Several times, the sonde reached higher altitudes and the hypsometer ceased to work. In case of the Ny-Ålesund measurements major problems occured in the controlling unit, probably caused by a changed current drain of the dry hypsometer. After separating the power supplies, the hypsometer drop out did not influence the controlling unit anymore. When a stable GPS-signal during the entire flight can be guaranteed, as the experiences of the last measurement campaign suggest, the hypsometer is not needed anymore.

The software failure which caused the incomplete data record on the SD card was identified and solved. The read-out from the found SD-card of PIOS VI showed a complete data set, including the spectra and channels which were not transmitted.

Starts have been carried out with three different types of balloons: Totex 2000, Totex 3000, and BT-5. The use of Totex 3000 balloons (7 flights) allowed altitudes between 34 and 37 km. As expected the sonde launched with Totex 2000 (PIOS B) reached a lower altitude of 32 km. Both polyethylene balloons could be followed to altitudes above 38 km. The maximal recorded altitude of 42.5 km was reached by PIOS III. PIOS IV was probably ascending further after the altitude measurement stopped at 38 km. For reaching altitudes above 40 km the use of polyethylene film balloons is necessary.

All major problems which occured after the launch of the prototype could be solved by implementing further improvements and continuously testing. The actual system does not show any problems with the telemetry and guarantees a stable data transmittance during the entire flight. Also a stable GPS signal could be received by the revised system, thus allowing for unrestricted data analysis. The technical development of the balloon-borne PIOS system is therefore completed.

PIOS	Date	Spect.	RS	GPS	Telemetry	z_{max}	balloon
$\mathrm{A}^{SD,1}$	21.1.2004	1932	1141	fine	early loss	17 km	TX 3000
$\mathrm{B}^{SD,1}$	12.5.2004	3671	1157	problems	disturbed	32 km	TX 2000
C	13.5.2004	3674	1158	none	early loss	12 km	TX 2000
I^{1}	10.6.2004	3670	1159	problems	fine	35 km	TX 3000
II	12.6.2004	3671	1154	none	fine	35 km	TX 3000
III	18.6.2004	3673	1140	fine	fine	42 km	BT-5
IV	24.6.2004	3675	1161	problems	disturbed	38 km	BT-5
V^{SD}	12.7.2005	3739	1163	fine	fine	36 km	TX 3000
$\mathrm{VI}^{SD,1}$	15.7.2005	3670	1141	fine	fine	34 km	TX 3000
$\mathrm{VII}^{SD,1}$	18.7.2005	1932	1157	fine	fine	35 km	TX 3000
$\mathrm{VIII}^{SD,1}$	20.7.2005	3713	1165	fine	fine	37 km	TX 3000
IX^{SD}	21.7.2005	3658	1155	fine	fine	34 km	TX 3000

Table 6.1: Listing of PIOS measurements. Superscript *SD* marks the sondes, equipped with an SD-card. Superscript *1* marks the sondes which were found.

Chapter 7

Ozone profile retrieval

As an example for the retrieval of a trace gas profile using the radiation measurements of the new sonde, ozone was selected. Ozone is a strong absorber in the UV range. Its distribution can also be determined by other measurement methods, making a comparison of the obtained profiles feasible. Several retrieval algorithms for the determination of ozone concentration using radiation measurements exist. The PIOS data were analysed according to the algorithm developed for the Dobson spectrophotometer.

In the first section the data processing algorithm is outlined. The second section describes the necessary data corrections and the calculation of external parameters as realised in the individual functions.

In the third section the algorithm for calculating an ozone concentration profile of the preprocessed data is presented. The algorithm is illustrated by one example. A method for determining the vertical resolution of the obtained ozone profile is presented, which offers the possibility to evaluate the data quality

7.1 The computing algorithm

The computing algorithm for the data processing was programmed in a modular and flexible way using the MATLAB computing environment. A flow diagramme is shown in Figure 7.1. Individual parts or functions of the programme can be changed, added, or removed. For example, the determination of the Rayleigh scattering coefficients is now realised according to the approximation from BUCHOLTZ (1995), which is described below. It is possible to replace the calculation formula with another approximation, or with a predetermined table, or obtain the Rayleigh scattering information as input from a radiation transfer model. By this modular programming a stepwise optimisation of the algorithm is possible without changes in the main structure.

Before starting the algorithm the details of the analysis are selected in a parameter file, including:

- Setting the data input and output paths,

- Activating and deactivating of functions,
- Selecting the input files for absorption coefficients etc.,
- Setting the averaging length,
- Activating the display and/or the storage of intermediate results and of comments on the data processing thus effecting directly the computing time,
- Defining the instrument's function.

The analysis is divided into four main steps, which can be processed as a complete series or in individual steps. In that case, stored results of previous calculated steps are used as input variables.

First, the raw data are imported and organised in an array structure, which will be stepwise extended during the further analysis. If necessary, the measurements are corrected for data failures. For each height the solar zenith angle and the air mass are calculated.

The second step contains the preparation of the measurements for the trace gas retrieval. First, the burst point is determined. If selected in the parameter file, the data set is reduced to the data measured during the ascent. The dark current is corrected for temperature influences. By comparing the measured spectrum with the Fraunhofer structures, the spectral calibration of the spectrometer is determined for every measurement.

In the third step the necessary coefficients and parameters for the trace gas analysis are imported: the scattering coefficients, the absorption cross sections, and the extraterrestrial radiation.

In the final step the vertical columns of ozone for every measurement are calculated. The vertical columns are averaged for the selected number of measurements. The averaged columns are then differentiated to get the ozone concentration profile in equidistant altitude steps.

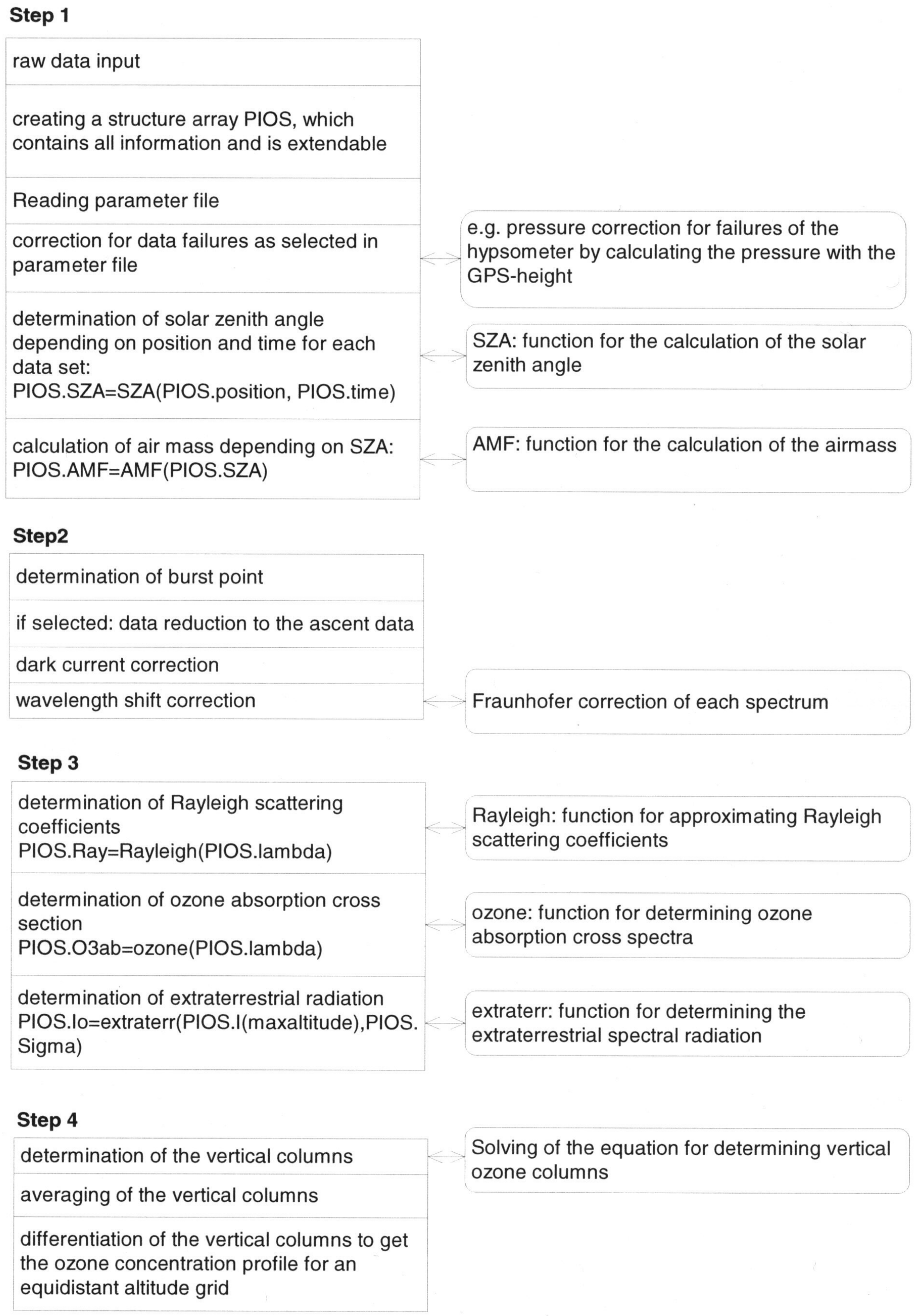

Figure 7.1: Flow diagramme of the analysis software. The left column illustrates the main programme, divided into four parts. It can be calculated as a complete process as well as individually step by step. In this case the parameter file and stored results of previous calculated steps are used as input. In the right column, functions are shown, which calculate the parameter demanded by the main programme. These functions can be exchanged or extended. They can be also used as a link to other programmes or models.

7.2 Description of the used functions

Several parts of the main programme are realised by functions, indicated by boxes with rounded corners in Figure 7.1. The functions can be replaced, thus allowing a future optimisation of the calculations. This section presents the functions used in this study to obtain the ozone profiles.

7.2.1 Correction of data failures

Generally the transmitted data show a very high quality. However, off course parts of the data sets may be incomplete or corrupted due to failures of single instruments or in the radio transmission. Depending on the type of failure, different correction methods may be used. As explained in chapter 6 during some flights, problems occured with the hypsometer or the GPS - receiver. During five flights the water hypsometer stopped working, when the sonde reached altitudes > 35 km. One flight was performed without pressure measurements of the hypsometer. In these cases the missing values are substituted by calculated pressure values, using the altitude measurements of the GPS receiver and the ambient air temperatures. In the opposite case of GPS-failures, the altitude are corrected by using the barometric height determined from the pressure measurements.

7.2.2 Air mass approximation

The solar zenith angle is determined with the actual time and position of the sonde, which is permamently recorded by the GPS receiver. The air mass is calculated using the approximation formula of Kasten and Young (1989), which is appropriate for the curvature of the atmosphere:

$$\mathrm{AMF} = \left[\sin(90^\circ - \mathrm{SZA}) + a \cdot (90^\circ - \mathrm{SZA} + b)^{-c}\right]^{-1}, \tag{7.1}$$

with $a = 0.50572$, $b = 6.07995^\circ$, and $c = 1.6364$.
The solar zenith angle and the airmass determined for the flight of PIOS III (18.6.2004, Ny-Ålesund) is shown in Figure 7.2. The sonde was launched at 11:30 UTC, after the local noon, thus resulting in an increasing solar zenith angle with time (or altitude).

7.2.3 Correction of the temperature influence on the optical measurements

As described in chapter 5 the box temperatures influence the spectrometer measurements. The dark current is corrected as described in section 5.2 with the signal measured at channel # 1. The spectral calibration of the spectrometer is corrected for each measurement using the Fraunhofer correction described in section 5.2.

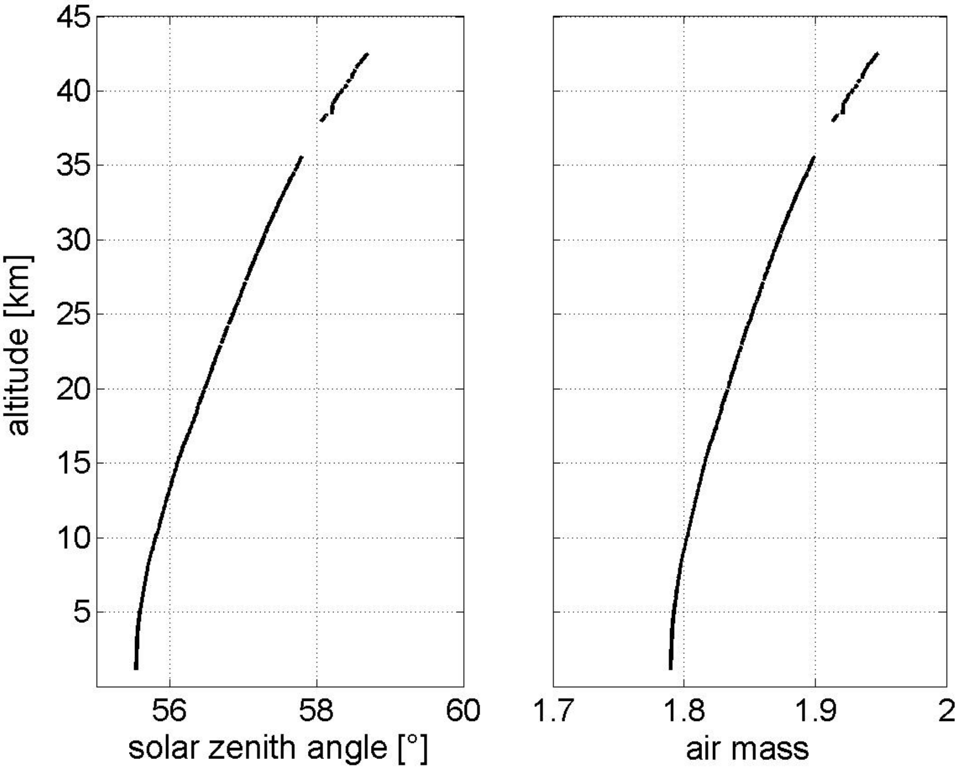

Figure 7.2: Solar zenith angle (left) and airmass (right) versus altitude for the flight of PIOS III, launched on the 18.6.2004 in Ny-Ålesund. The airmass was calculated with the approximation given in Equation 7.1.

7.2.4 Rayleigh scattering

Rayleigh scattering cross sections are calculated according to Bucholtz (1995), who suggests the following approximation:

$$\sigma_{Ray}(\lambda) = A \cdot \lambda^{-(B+C\lambda+D/\lambda)}, \tag{7.2}$$

with the wavelength λ in μm; $A = 3.01577 \cdot 10^{-28}$, $B = 3.55212$, $C = 1.35579$, and $D = 0.11563$. The optical depth τ at altitude z_0 can be written as

$$\tau_{Ray}(\lambda, z_0) = \sigma_{Ray}(\lambda) \cdot VC(z_0), \tag{7.3}$$

with $VC(z_0)$ is the vertical column at altitude z_0. Typical values for the vertical columns of air at the starting alitude z_0 are taken from Bucholtz (1995). The optical depth $\tau(\lambda, z)$ at any altitude z can be approximated by:

$$\tau_{Ray}(\lambda, z) = \tau_{Ray}(\lambda, z_0) \cdot \frac{p(z)}{p(z_0)}. \tag{7.4}$$

The effective optical depths were calculated at different wavelengths with a resolution of $\Delta\lambda = 0.01$ nm and convolved with the instrument's slit functions (Equation 5.1.

7.2.5 Ozone absorption cross section

As recommended by SANDER et al. (2003) the ozone absorption cross sections σ_{O_3} were taken from MALICET et al. (1995). The absorption cross sections at a temperature of 243 K were used (Figure 7.3). The effective cross sections were calculated by convolving the absorption cross sections (available with $\Delta\lambda = 0.01$ nm) with the instrument's slit function.

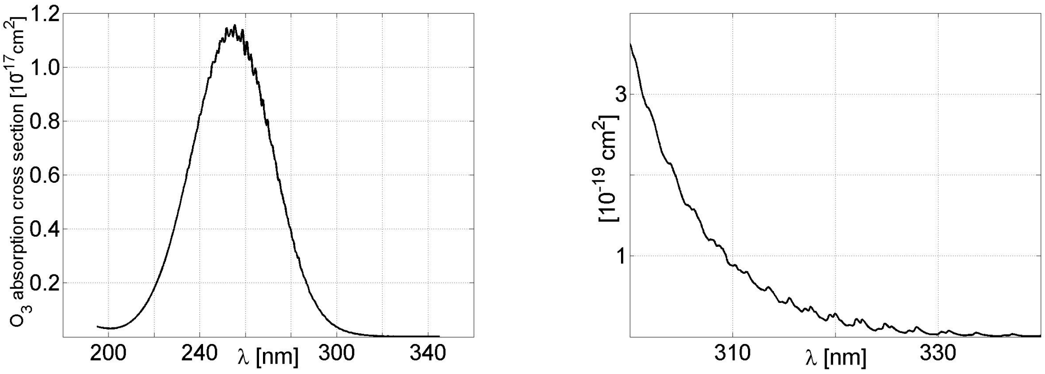

Figure 7.3: Absorption cross sections for ozone after MALICET (1995) for the wavelength range between 180 and 340 nm (left). The right panel shows an enlargement of the wavelength range between 300 and 340 nm.

7.2.6 Extraterrestrial radiation

The incoming extraterrestrial radiation I_0 is estimated from the measurements at the burst point of the balloon z_{max}:

$$I_0(\lambda) = I(z_{max}, \lambda) \cdot \exp\left[\sigma(\lambda) \cdot VC_{O_3}(z_{max}) \cdot AMF\right]. \tag{7.5}$$

All flights reached altitudes above 34 km. In this altitude the scattering of radiation between the top of the atmosphere and the instrument can be neglected. The amount of ozone in the vertical column above the burst point was set to $0.5 \cdot 10^{18}$ molecules cm^{-2}.

7.3 Calculation of the ozone profile

The measured data set of the PIOS instrument contains the spectral solar radiation for each measurement altitude ($\Delta z \approx 45$ m). With the external parameters, such as the extraterrestrial radiation and absorption and scattering cross sections, Equation 3.10

$$\begin{aligned} I &= I_0 \cdot \exp\left[-\sum_{j=1}^{J} \sigma_j(\lambda) VC_j \cdot \mathrm{AMF}\right] \\ &\quad \cdot \exp\left[-\sigma_{Ray}(\lambda) VC_{air} \cdot \mathrm{AMF}\right] \cdot \exp\left[-\sigma_{Mie}(\lambda) VC_{aer} \cdot \mathrm{AMF}\right] \quad (3.10) \end{aligned}$$

can be solved for the amount of ozone above the sonde, the vertical column.

The sonde measures the global irradiance, because its detector has a field of view of 180°. The global irradiance is composed of direct and diffuse irradiance. With the radiative transfer model LibRadtran (Mayer and Kylling 2005) the fraction of direct and diffuse irradiance was computed for the wavelength range from 300 to 340 nm. At 20 km the direct irradiance amounts to 95% and diffuse irradiance amounts to 5% of the global irradiance. Towards higher altitudes the fraction of direct light increase even more. At 10 km altitude the direct irradiance amounts to 85% at a solar zenith angle of 30° and to 80% at a solar zenith angle of 57° of the global irradiance. For the following analysis the diffuse component was neglected because of its low fraction.

7.3.1 The adopted Dobson spectrometer algorithm

The algorithm for calculating the total ozone above each position of the sonde is taken from the Dobson spectrometer analysis (e.g. Dobson (1957) and (Komhyr 1980)). It is based on measuring the relative intensities of the direct radiation of selected pairs of ultraviolet wavelengths, called the A, B, C, and D wavelength pairs. Table 7.1 lists the wavelengths and their effective absorption and scattering optical depths. The A wavelength pair, for example, consists of 305.5 and 325.4 nm. The shorter wavelength of the pairs is located within the absorption band of ozone, whereas the longer wavelength is relatively unaffected by ozone.

Outside the Earth's atmosphere the relative intensity of the two wavelengths remains essentially fixed. On their way through the atmosphere to the instrument they are attenuated because of scattering by air molecules and aerosols. If ozone molecules are present, the shorter wavelength is strongly absorbed, whereas the attenuation of the longer wavelength is weak. Therefore, the relative intensity measured by the instrument in the altitude z varies with the amount of ozone present in the atmosphere above altitude z.

Thus, by measuring the relative intensities of the selected wavelength pairs in each altitude during the ascent of the sonde, it is possible to determine the amount of ozone in the vertical column of air extending from the position of the sonde to the top of the atmosphere.

#	λ	σ_{O_3}	τ_{Ray}
A_1	305.5	1.6658e-19	1.1265
A_2	325.4	1.1555e-20	0.8600
B_1	308.8	1.0926e-19	1.0757
B_2	329.1	4.4614e-21	0.8197
C_1	314.5	4.7069e-20	0.9946
C_2	332.4	2.5021e-21	0.7857
D_1	317.6	3.2650e-20	0.9537
D_2	339.8	1.0751e-21	0.7159

Table 7.1: The Dobson wavelengths and their effective ozone absorption cross sections and Rayleigh optical depths. Ozone absorption cross section are taken from Malicet (1995). The Rayleigh optical depths are calculated with the approximation formula given in Equation 7.4. Both are convolved with the instrument's function.

For the analysis of the measured intensities of a Dobson spectrometer only absorption by ozone is considered, since the wavelengths are selected in a way that the absorption of ozone is large compared to other absorbers. The ratio of the intensities of a wavelength pair λ and λ' by using Equation 3.10 can be calculated:

$$\begin{aligned}\frac{I(\lambda)}{I(\lambda')} &= \frac{I_0(\lambda)}{I_0(\lambda')} \cdot \exp\left(-(\sigma_{O_3}(\lambda) - \sigma_{O_3}(\lambda')) \cdot VC_{O_3} \cdot AMF\right) \\ &\quad \cdot \exp\left(-(\sigma_{Ray}(\lambda) - \sigma_{Ray}(\lambda')) \cdot VC_{air} \cdot AMF\right) \\ &\quad \cdot \exp\left(-(\sigma_{Mie}(\lambda) - \sigma_{Mie}(\lambda')) \cdot VC_{aer} \cdot AMF\right). \end{aligned} \tag{7.6}$$

The differences between the attenuation cross sections of the wavelength pair λ and λ' are substituted by

$$\Delta\sigma_i = \sigma(\lambda_i) - \sigma(\lambda_i'). \tag{7.7}$$

The vertical column of ozone $VC_{O_3}(z)$ above the instrument in altitude z can be calculated according to:

$$\begin{aligned} VC_{O_3}(z) &= \frac{\ln\frac{I_0(\lambda)}{I_0(\lambda')} - \ln\frac{I(\lambda)}{I(\lambda')}}{\Delta\sigma_{O_3,i} \cdot AMF} \\ &\quad - \frac{\Delta\sigma_{Ray,i} \cdot VC_{air} \cdot AMF + \Delta\sigma_{Mie,i} \cdot VC_{aer} \cdot AMF}{\Delta\sigma_{O_3,i} \cdot AMF}. \end{aligned} \tag{7.8}$$

If the optical depth instead of the scattering cross section for Rayleigh and Mie scattering is used, the following equation is obtained:

$$
\begin{aligned}
VC_{O_3} &= \frac{\ln\frac{I_0(\lambda)}{I_0(\lambda')} - \ln\frac{I(\lambda)}{I(\lambda')}}{\Delta\sigma_{O_3,i}\cdot AMF} \\
&\quad - \frac{\Delta\tau_{Ray,i}\cdot AMF + \Delta\tau_{Mie,i}\cdot AMF}{\Delta\sigma_{O_3,i}\cdot AMF}. \qquad (7.9)
\end{aligned}
$$

The Rayleigh optical depths are calculated using Equation 7.4.
The most critical term in Equation 7.9 is the aerosol optical depth. It is highly variable, owing to varying atmospheric conditions, and it is impossible to routinely estimate its value to a sufficient accuracy by independent means, e.g. Komhyr (1980) and Basher (1982). Therefore, the radiation measurements at two wavelength pairs are used. Forming Equation 7.6 for both wavelength pairs,e.g. A and D, substracting one from the other, and solving for VC gives:

$$
\begin{aligned}
VC_{O_3} &= \frac{\ln\frac{I_{0,\lambda_1}}{I_{0,\lambda_1'}} - \ln\frac{I_{0,\lambda_2}}{I_{0,\lambda_2'}} - \left(\ln\frac{I_{\lambda_1}}{I_{\lambda_1'}} - \ln\frac{I_{\lambda_2}}{I_{\lambda_2'}}\right)}{(\Delta\sigma_{O_3,1}-\Delta\sigma_{O_3,2})\cdot AMF} \\
&\quad - \frac{(\Delta\tau_{Ray,1}(z_0)-\Delta\tau_{Ray,2}(z_0))\cdot AMF\cdot\frac{p(z)}{p(z_0)}}{(\Delta\sigma_{O_3,1}-\Delta\sigma_{O_3,2})\cdot AMF} \\
&\quad - \frac{(\Delta\tau_{Mie,1}-\Delta\tau_{Mie,2})\cdot AMF}{(\Delta\sigma_{O_3,1}-\Delta\sigma_{O_3,2})\cdot AMF}. \qquad (7.10)
\end{aligned}
$$

The aerosol extinction varies little over the wavelength range from 305 to 340 nm. The nearly equal wavelength difference of both wavelength pairs allows the assumption (Komhyr 1980):

$$\Delta\tau_{Mie,1} - \Delta\tau_{Mie,2} = 0. \qquad (7.11)$$

The air masses for different attenuating media differ only sligthly for solar zenith angles SZA$<70°$ for ozone and air molecules. However, if we assume only direct light measurements, the different vertical distribution of the attenuating media needs not to be taken into account. Therefore the same air mass is used for ozone and air molecules. The vertical column amount of ozone in every position of the sonde is calculated as:

$$
\begin{aligned}
VC_{O_3} &= \frac{\ln\frac{I_{0,\lambda_1}}{I_{0,\lambda_1'}} - \ln\frac{I_{0,\lambda_2}}{I_{0,\lambda_2'}} - \left(\ln\frac{I_{\lambda_1}}{I_{\lambda_1'}} - \ln\frac{I_{\lambda_2}}{I_{\lambda_2'}}\right)}{(\Delta\sigma_{O_3,1}-\Delta\sigma_{O_3,2})\cdot AMF} \\
&\quad - \frac{(\Delta\tau_{Ray,1}-\Delta\tau_{Ray,2})\cdot\frac{p(z)}{p_0}}{(\Delta\sigma_{O_3,1}-\Delta\sigma_{O_3,2})}. \qquad (7.12)
\end{aligned}
$$

7.3.2 Calculation of the vertical ozone columns

As an example for the previously described algorithm, the retrieval of the vertical ozone column is described with the data of the flight PIOS V, launched 12.7.2005 at the Meteorological Observatory in Hohenpeißenberg (MOHp). The start time was 9:51 UTC and the balloon reached a maximum altitude of 35.9 km. The integration time of the spectrometer was 255 ms. The solar zenith angle during the ascent decreased from 35.7° to 25.6° at 27 km altitude (≈ 11:20 UTC). At the maximum altitude of 35.9 km (12:00 UTC) the solar zenith angle was 26.9°.

The inflight measured dark current at channel #1 of flight PIOS V is plotted in Figure 7.4. Each measured spectral data set is corrected with this representative dark current.

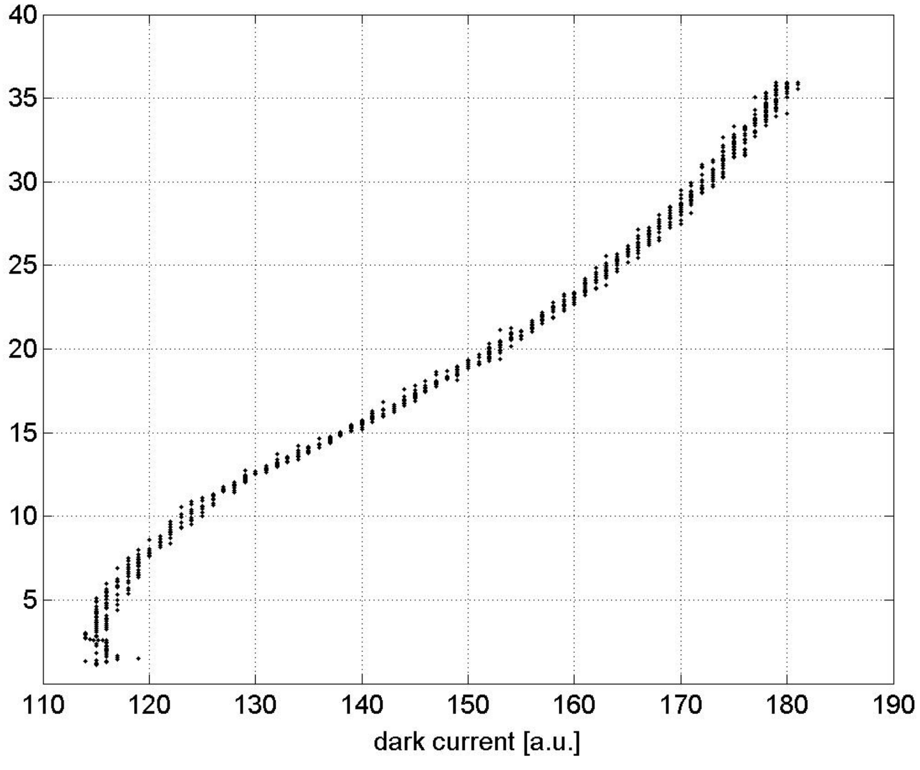

Figure 7.4: The detected inflight dark current of channel #1 versus altitude. Data are taken from PIOS V flight (12.7.2005, MOHp).

For each data set the new wavelength calibration of the spectrometer channels is determined by the Fraunhofer correction. This results in a different channel-to-wavelength relation for each data set, as can be seen in Figure 7.5. For the further analysis irradiance profiles from fixed wavelengths are necessary. Therefore, the irradiance spectrum has to be interpolated at the selected wavelengths for each altitude.

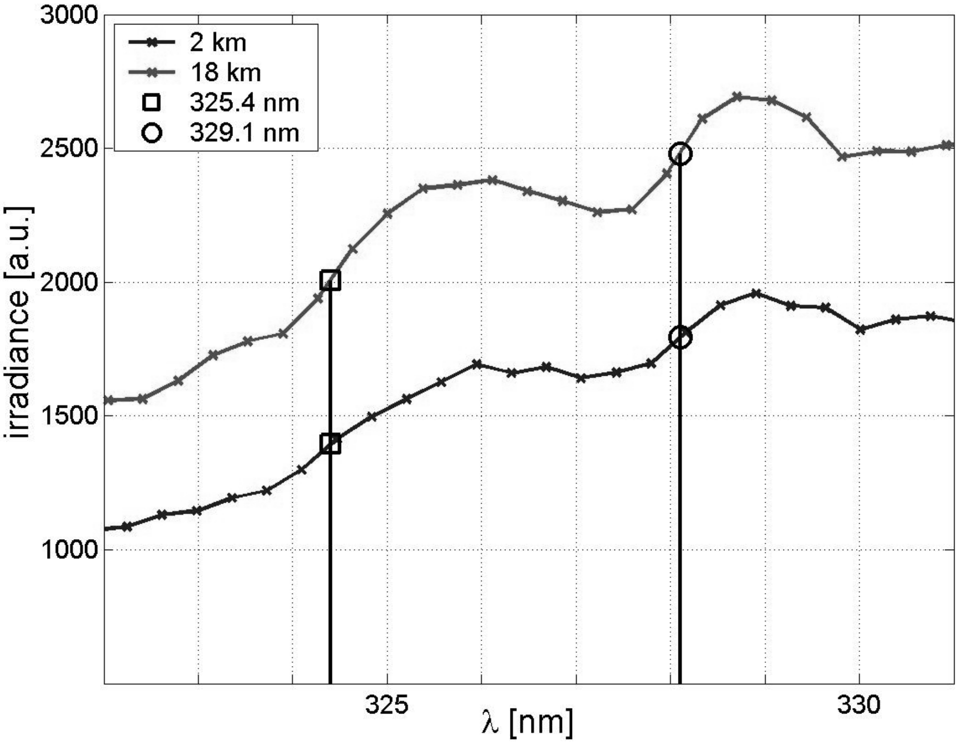

Figure 7.5: Irradiance spectra at 2 km (blue) and 18 km (red) altitude in the wavelength range from 320 to 335 nm. The wavelength positions of the channels are marked with crosses. The symbols show the interpolated irradiances at the Dobson wavelengths A_2 (square) and B_2 (circle). Data are taken from PIOS V flight (12.7.2005, MOHp).

The obtained irradiance profiles $I(\lambda, z)$ at the 6 Dobson wavelengths A_1, A_2, B_1, B_2, D_1, and D_2 are plotted in Figure 7.6. The profiles show a small size scattering of the signal caused by the noise of the instrument, and the numerical operations done so far. The irradiance profiles increase with altitude up to 30 km, due to the decreasing path length of the light through the attenuating atmosphere. Above 30 km the signals are significantly decreasing caused by the decreasing sun elevation. Additionally, some middle size structures are visible, which may be caused by the different viewing angles of the sonde.

Figure 7.7 shows the ratio of the irradiances at the Dobson wavelength pairs and the logarithms of the ratios. The relative irradiance profiles further show a low noise in the signal and a change with altitude, but the middle size structures are

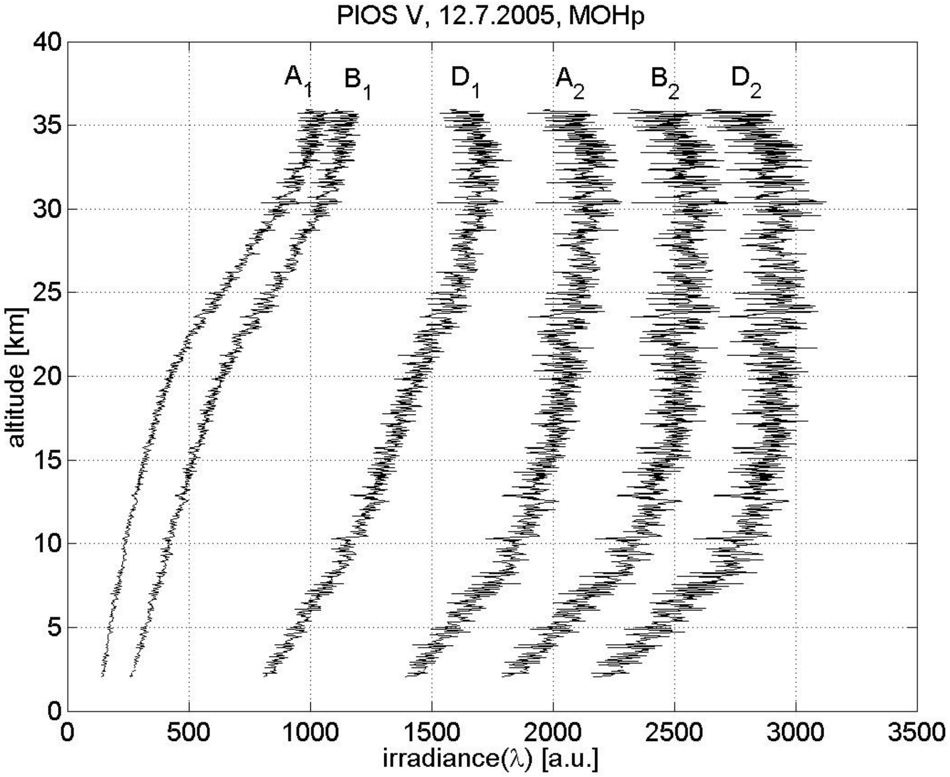

Figure 7.6: Irradiance profiles of the Dobson wavelengths A_i, B_i, and D_i measured during PIOS V flight (12.7.2005, MOHp).

eliminated.

Now Equation 7.12 can be solved at each altitude step. The calculated vertical column densities are plotted versus altitude for both, the AD and the BD wavelength combination.

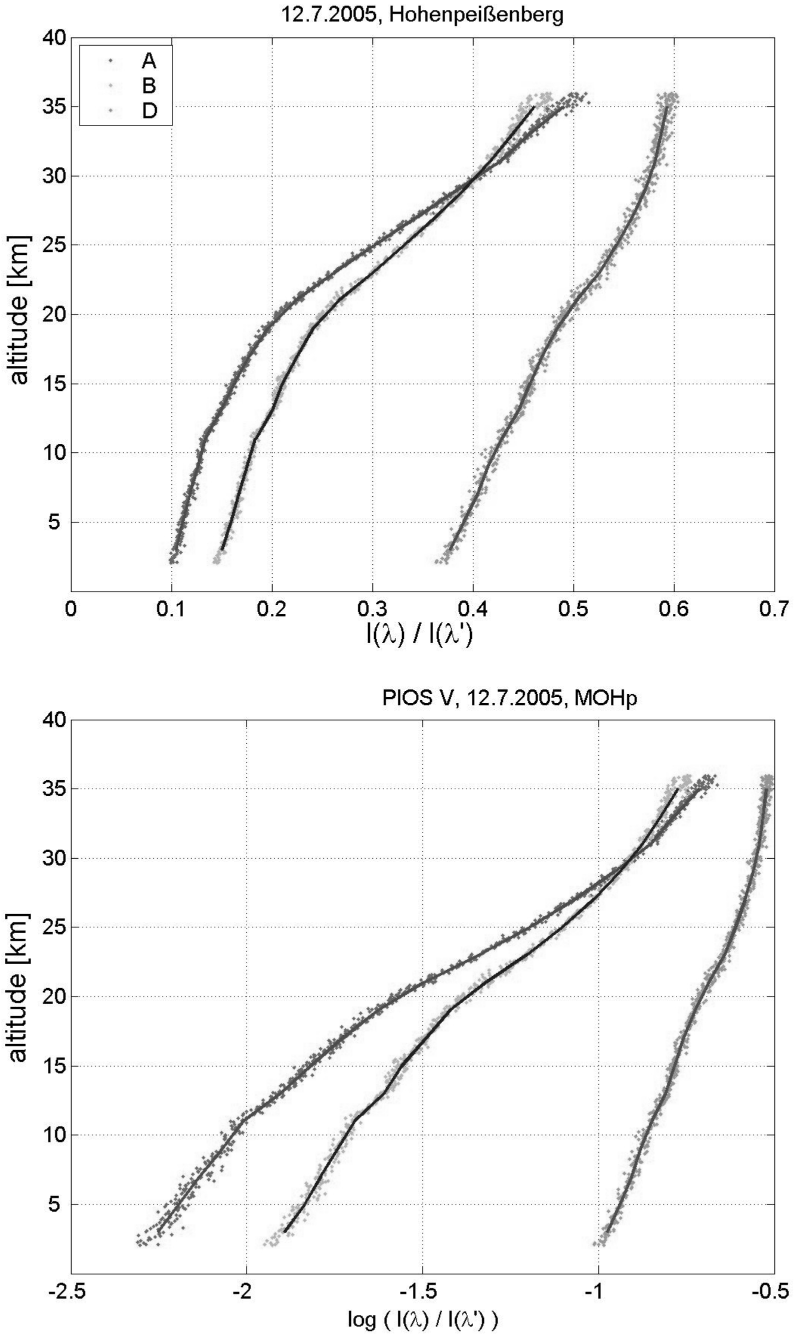

Figure 7.7: Altitude dependence of the ratios (top) and the logarithms of the ratios (bottom) of the measured irradiance profiles of the Dobson wavelength pairs A_i, B_i, and D_i. Data from PIOS V flight (12.7.2005, MOHp).

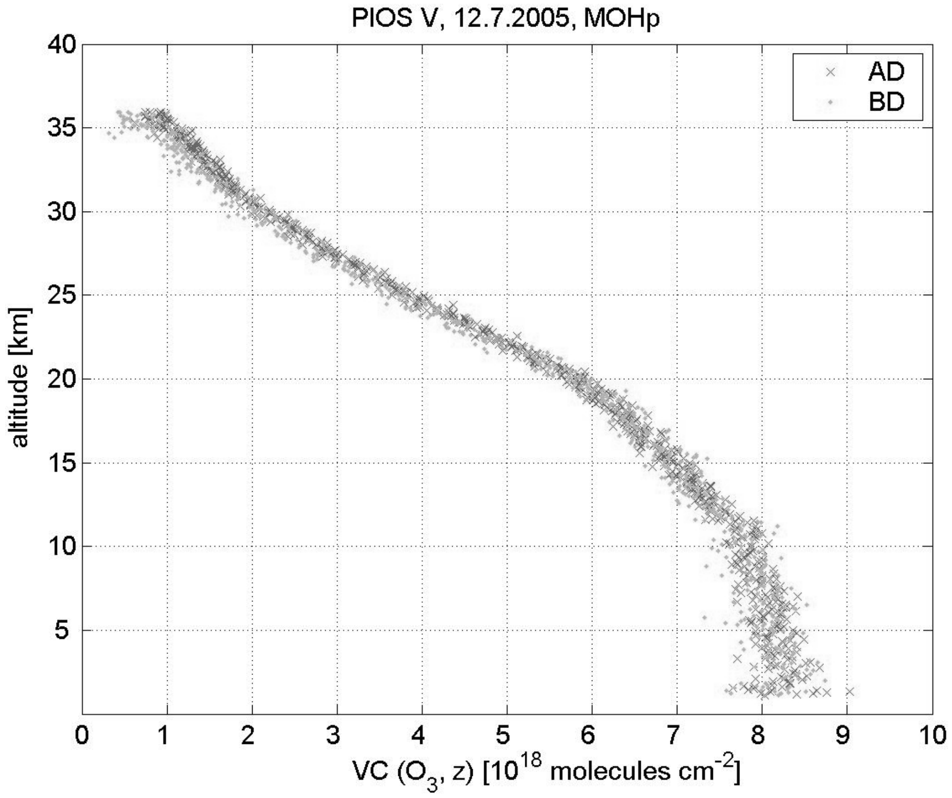

Figure 7.8: The vertical column density of ozone, calculated with the adopted Dobson algorithm for the wavelength combinations AD(magenta) and BD(cyan). Data from PIOS V flight (12.7.2005, MOHp).

7.3.3 Estimation of the possible vertical resolution of the ozone profiles

The obtained vertical column density profile shows a significant noise around a mean profile, including the noise of the instrument and of the performed numerical operations. A running mean is calculated for the vertical profile by averaging 50 data points ($\approx$ 2 km), left panel in Figure 7.9. The differences between this smoothed profile and the single data points are decreasing with the altitude as can be seen in Figure 7.9.

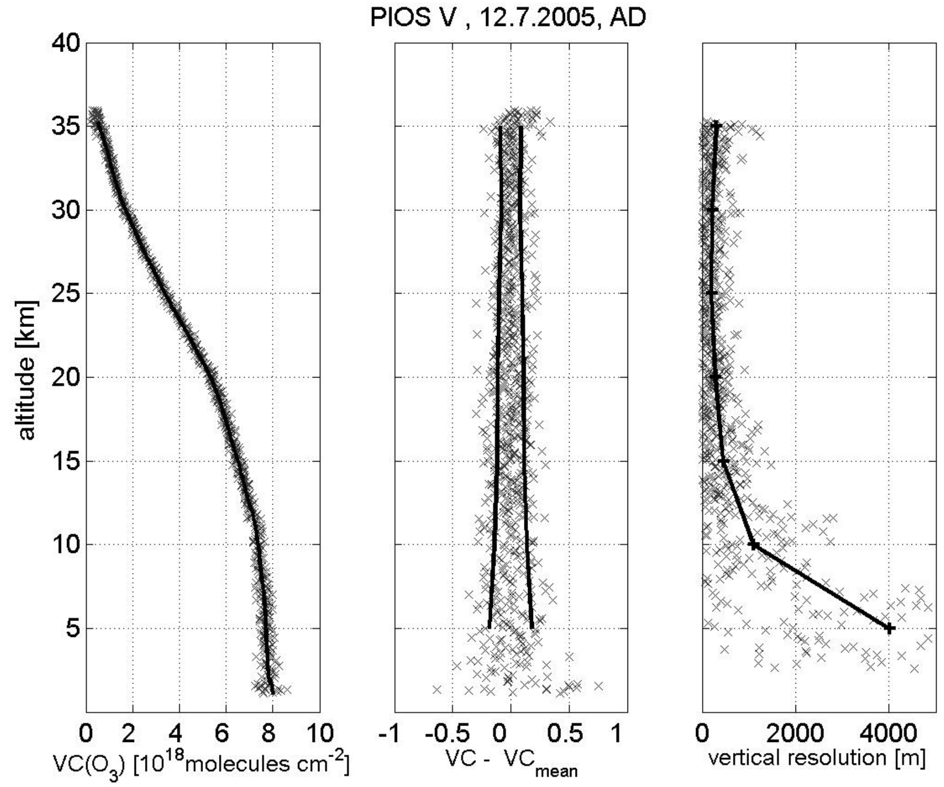

Figure 7.9: Data from PIOS V flight (12.7.2005, MOHp). Left: The vertical ozone columns for the wavelength pair combination A and D versus altitude (crosses). The solid line is the averaged profile. Middle: Differences between the single data points and the averaged vertical columns. The solid lines include 70% of all calculated differences. Difference are given in the same unit as the vertical columns [10^{18} molecules cm^{-2}]. Right: The calculated vertical resolution (crosses) and mean values of the vertical resolution for 5 km altitude intervalls.

This noise determines the maximal possible vertical resolution of the calculated ozone concentration profile. Comparing the noise with the slope of the vertical column profile gives the minimum altitude difference, which allows the detection of a change in the vertical column density.

The mean slopes of the vertical column density by averaging 5 km. Dividing the noise by the obtained slope, results in the altitude difference, for which the change in the vertical column has the same size as the noise.

The result corresponds to the vertical resolution. The vertical resolution for each data point and for mean values are shown in Figure 7.9. Large values (low vertical resolution) are shown for lower altitudes with larger noise and smaller changes in the vertical column profile. Between 15 and 35 km the vertical resolution has values below 1000 m. The maximal vertical resolution of 200 m is calculated at 25 km altitude. At the maximum altitude at 35 km the vertical resolution is slightly smaller, due to the smaller slope in the vertical column density profile.

7.3.4 Calculation of ozone profiles

The ozone concentration profile is derived by differentiating the ozone vertical columns.

The ozone vertical columns calculated with Equation 7.12 are averaged with a running mean using the mean vertical resolution (typically between 1 and 2 km) for the launch as averaging length (Figure 7.8).

The obtained profile is divided into 1 km sections. For each section a linear regression fits a straight line to the data (Figure 7.10).

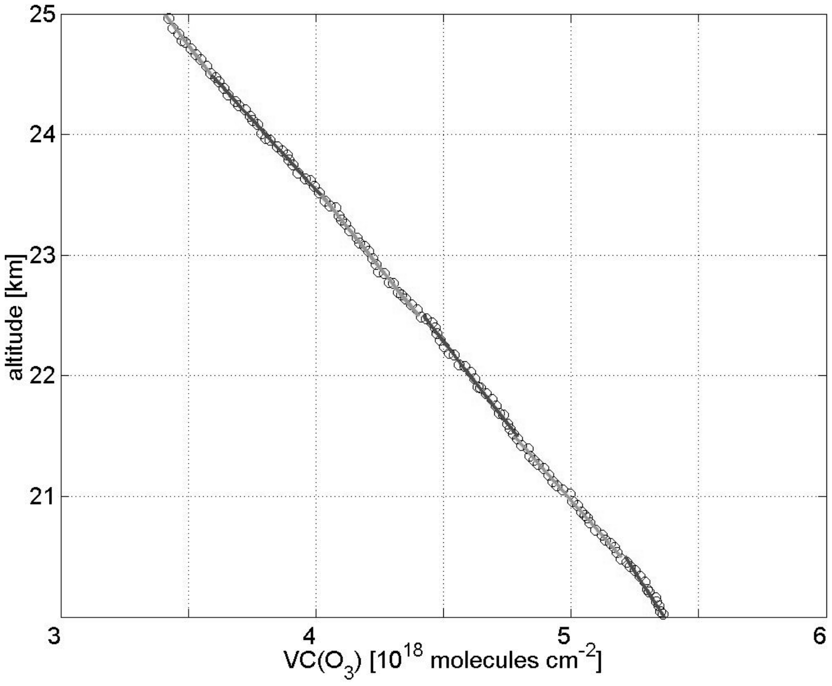

Figure 7.10: Averaged vertical ozone columns for the altitude intervall between 20 and 25 km (circles). For 1-km-sections a straight line is fitted to the data by linear regression (solid lines). Data from PIOS V flight (12.7.2005, MOHp).

The slope of each line gives the ozone number density for the corresponding altitude intervall. The calculated ozone number density profile with $\Delta z = 1$ km for both wavelength pair combinations AD and BD is shown in Figure 7.11. For a fast overview on the reliability of the results, the profiles are differently marked, dependent on a high (< 1000m) or low (> 1000m) vertical resolution.

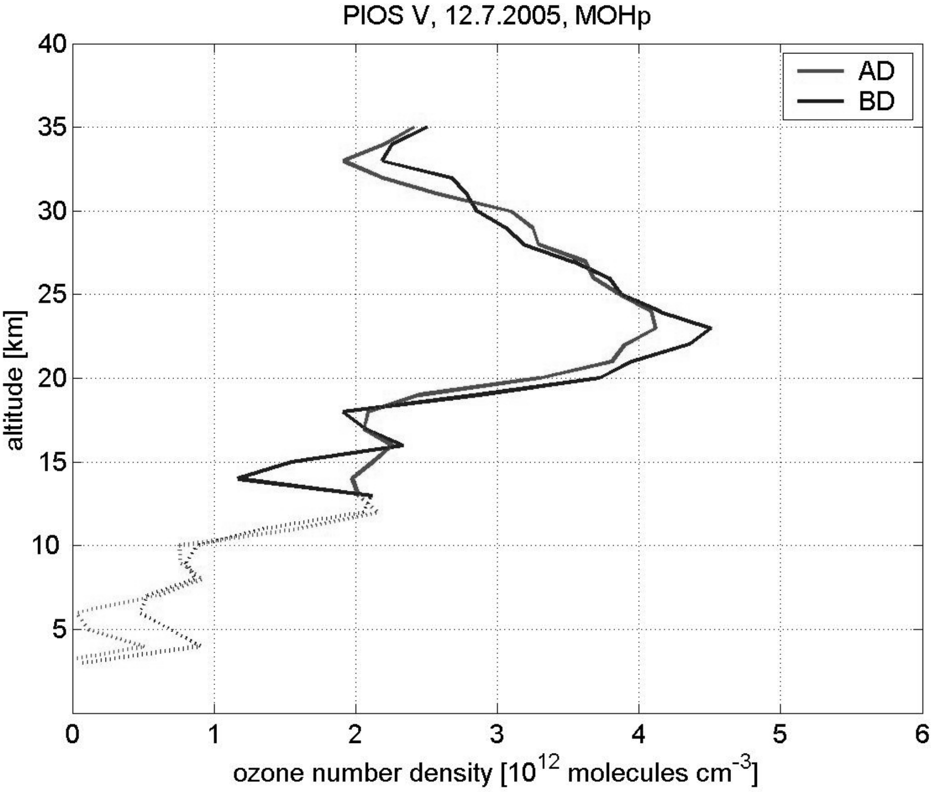

Figure 7.11: Ozone number density profiles, calculated with the Dobson wavelength combinations AD and BD. The ozone number density profiles are calculated for both Dobson wavelength combinations AD and BD. Data from PIOS V flight (12.7.2005, MOHp).

Chapter 8

Measurement campaigns: data evaluation

The solar spectral data measured during the nine ascents of two campaigns in Ny-Ålesund, Svalbard, and Hohenpeißenberg, Germany are analysed in this chapter. The intensity changes in the detected solar spectrum with altitude are demonstrated using a representative example.
According to the description in chapter 7 the vertical ozone columns are derived from the irradiance measurements. For all flights the vertical resolution for different altitude sections were determined, providing an evaluation tool for the data quality of the individual measurements.
The ozone number density profiles are then calculated by differentiating the vertical ozone columns (subsection 7.3.4). The obtained ozone profiles are compared with profile measurements of electrochemical sondes and in three cases also with LIDAR-measurements.
The spectral data in the visible wavelength range between 430 and 450 nm are checked for NO_2 absorption.

8.1 Irradiance changes with height

Due to the attenuation of the solar radiation by trace gas absorption and scattering in the atmosphere the solar spectral irradiance changes with altitude. In this section the measured radiation data are presented. As an example spectra in different altitudes, measured by PIOS IV, launched on 24.6.2004 in Ny-Ålesund, in different altitudes are shown in Figures 8.1 8.2 and 8.3. Two sections of the spectra were selected for transmitting in a way that the corresponding wavelength range covers the Huggins and Chappuis absorption bands of ozone in order to have best conditions for the further ozone analysis using the data. The first section covers the wavelength range from about 250 to 500 nm, the second section covers the wavlength range between 550 and 650 nm. The data are presented in three parts: the UV-range (250 to 400 nm), the first visible range (400 to 500 nm) and the second visible range (550 to 650 nm).

8.1.1 Ultraviolet wavelength range

The measured UV solar spectrum in different altitudes is plotted in Figure 8.1. Due to the ozone absorption in the Huggins band no UV-radiation with shorter wavelengths than 300 nm is measured with the spectrometer at the Earth's surface. Particularly for these short wavelengths ($< 320\,\mathrm{nm}$), the measured intensity is increasing dramatically and shifting the cut off wavelength towards shorter wavelengths with higher altitudes. At 35 km altitude significant irradiance is measured down to 280 nm. The measured intensity at 300 nm was enlarged by more than one order of magnitude between the surface and an altitude of 35 km.

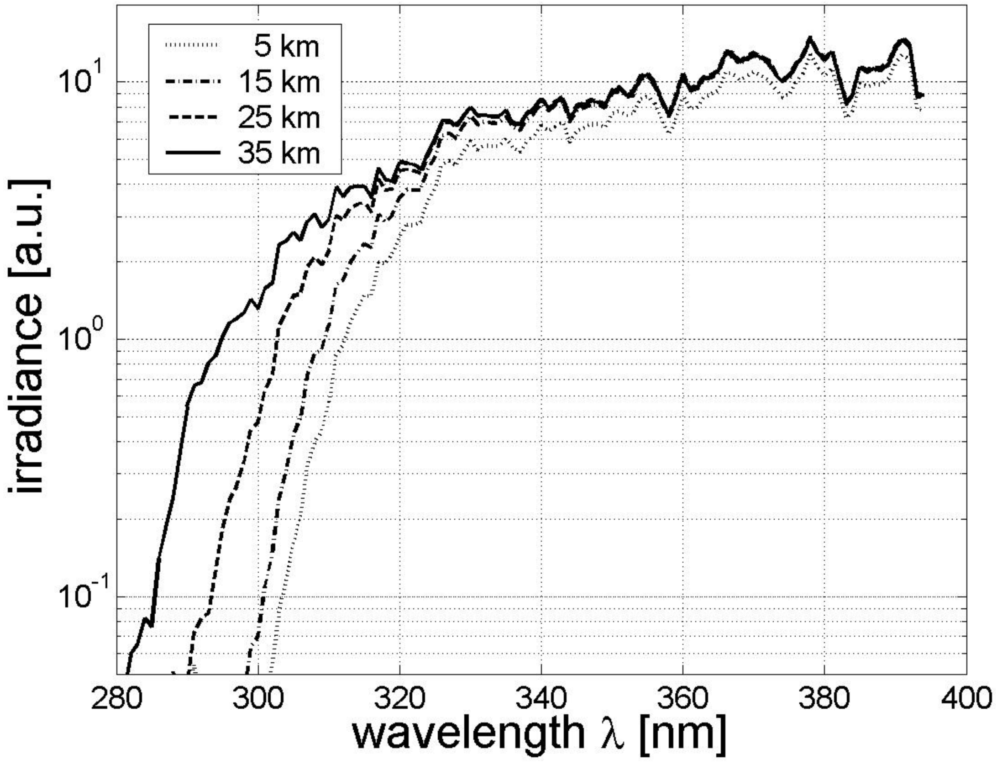

Figure 8.1: Measured spectra in the UV wavelength range from 280 to 400 nm at different altitudes between 5 and 35 km. The spectra were measured during the flight of PIOS IV, 24.6.2004 in Ny-Ålesund. The data are averaged vertically with an averaging length of 2 km and plotted every 10th kilometer.

8.1.2 Visible wavelength range

In the visible range between 400 and 500 nm a significant change with altitude is only detected between the measured intensity in 5 km and 15 km (Figure 8.2). Further spectral irradiance measurements between 15 and 35 km show very small differences. The spectrum in 35 km has even sligthly decreased values than the measurements below. During the ascent of the sonde, the solar zenith angle increased from 55.5° to 58°. The lower sun elevation is equivalent to a longer light path through the atmosphere which accounts for the slightly decreased intensity.

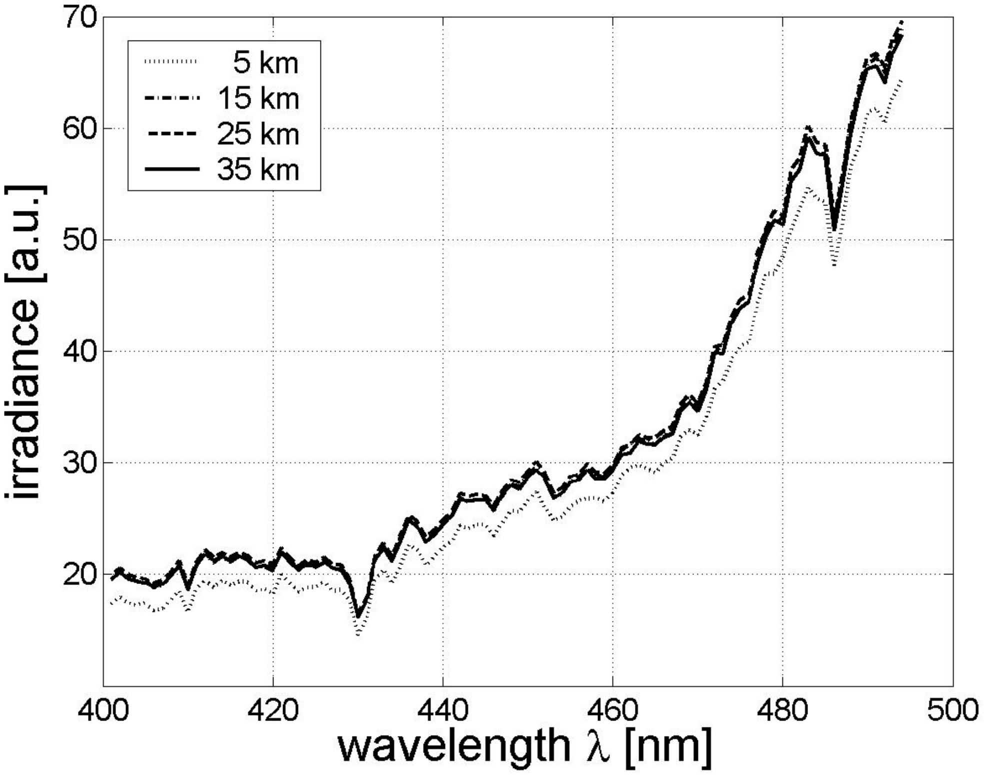

Figure 8.2: Measured spectra in the vis wavelength range from 400 to 500 nm at different altitudes between 5 and 35 km. The spectra were measured during the flight of PIOS IV, 24.6.2004 in Ny-Ålesund. The data are averaged vertically with an averaging length of 2 km and plotted every 10th kilometer.

Figure 8.3 shows the measured spectra for the wavelength range between 550 and 650 nm, where ozone absorbs in the Chappuis band. Ozone has its maximum absorption cross section of about $5{\cdot}10^{-21}$ cm^{-2} in the Chappuis band between 600 and 610 nm, Burkholder and Talukdar (1994). Between the spectra measured in the troposphere and the stratosphere a significant irradiance increase is seen in Figure 8.3. An increase between 15 km and higher altitudes is only visible in the wavelength range between 565 and 615 nm. That is likely a result of the ozone absorption, since the absorption cross sections in this range are larger than 4.2 $\cdot 10^{-21}$ cm^{-2} (Burkholder and Talukdar 1994).

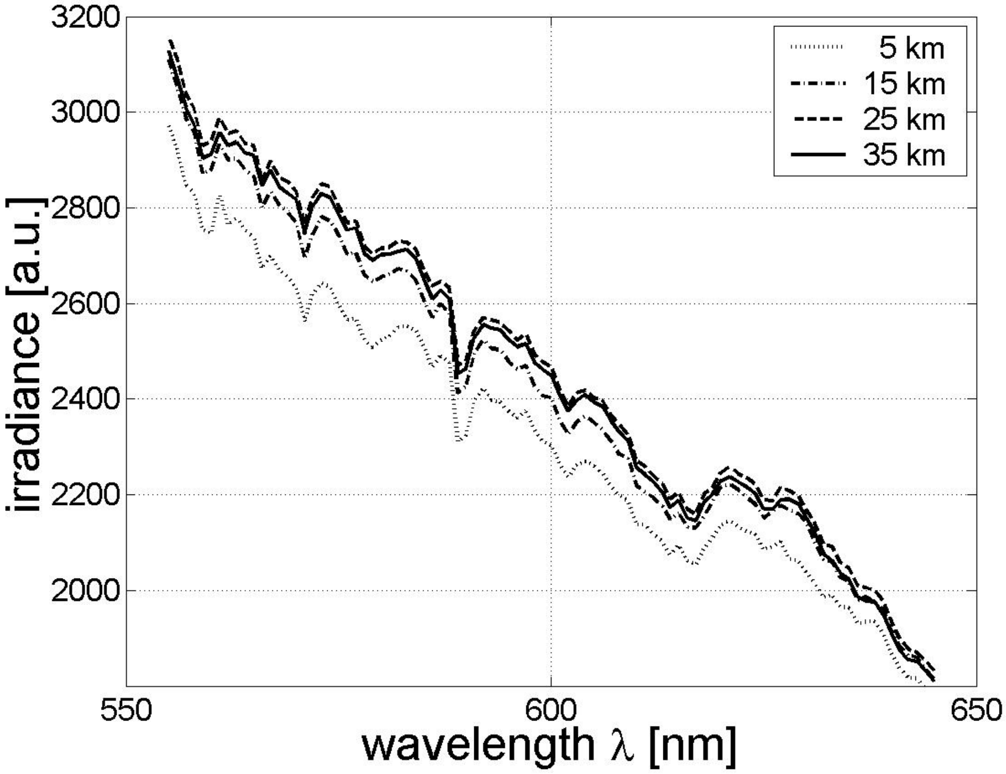

Figure 8.3: Measured spectra in the vis wavelength range from 550 to 650 nm at different altitudes between 5 and 35 km. The spectra were measured during the flight of PIOS IV, 24.6.2004 in Ny-Ålesund. The data are averaged vertically with an averaging length of 2 km and plotted every 10th kilometer.

8.1.3 Vertical ozone columns and vertical resolution

The vertical columns are calculated for nine flights according to the description in subsection 7.3.2. Four of the analysed flights were carried out in June 2004 in Ny-Ålesund, while five flights were performed in July 2005 in Hohenpeißenberg. The main difference in the measurement conditions was the solar elevation during the flights. At the high latitude of 79° N in Ny-Ålesund, the solar zenith angle changed between 55° and 58° during the measurements. In contrast at Hohenpeißenberg (48° N) the solar zenith angles varied between 25° and 39° during the measurements.

During the measurements in Ny-Ålesund the PIOS instrument was measuring with the automatic adaption of the integration time as described in section 4.1.3. That results in short integration times around 30-50 ms in the stratosphere, depending on the individual spectrometer. In Hohenpeißenberg the adaption mode of the integration time was varied for the different launches: One flight was performed with the unchanged automatic adaption of the integration time. For the further flights the adaption of the integration time during the flight was deactivated. One flight was performed with a fixed short integration time of 60 ms. Two flights were performed with a fixed long integration time of 255 ms. One flight was performed with a fixed long integration time of 250 ms.

Based on this different measurement conditions, the nine flights are divided into three different categories:

1. large solar zenith angle ($\geq 55°$) and short integration time (≤ 60 ms)
2. small solar zenith angle ($\leq 40°$) and short integration time (≤ 60 ms)
3. small solar zenith angle ($\leq 40°$) and long integration time (≥ 250 ms).

The flights are listed in Table 8.1 with the measurement conditions (SZA and integration time) and the category.

For all flights the vertical resolution in different altitude section are calculated (subsection 7.3.3). The results are listed in Table 8.2. For each category one measurement is presented in detail:

Figure 8.4 shows an example for a category 1 flight, PIOS III. The shown vertical ozone columns were calculated with the AD wavelength combination. The scattering around the vertical ozone column is less than $\pm 0.5 \cdot 10^{18}$ molecules cm^{-2} and is clearly increasing towards lower altitudes to about $\pm 2 \cdot 10^{18}$ molecules cm^{-2}. The resulting vertical resolution is very low at an altitude of 5 km (> 6000m), and increases to about 1000 m in about 20 km. Between 20 and 35 km altitude the vertical resolution remains almost constant at a value about 1000 m. At 40 km altitude a vertical resolution of about 3000 m was determined.

As an example for the category 2 measurement the PIOS VI flight, performed 15.7.2005 in Hohenpeißenberg is shown in Figure 8.5. The scattering in the vertical columns shows the same order of magnitude in the higher altitudes of

PIOS	Date	SZA [°]	$t_{\mathrm{int}}[ms]$	category
I	10.6.2004	55.8-56.2	30-40	1
II	12.6.2004	55.7-56.6	30-40	1
III	18.6.2004	55.5-58.7	50	1
IV	24.6.2004	55.5-58.2	30-40	1
V	12.7.2005	25.7-35.8	255	3
VI	15.7.2005	26.0-38.5	60	2
VII	18.7.2005	26.9-37.0	250	3
VIII	20.7.2005	27.0-36.7	250	3
IX	21.7.2005	27.3-37.3	30-40	2

Table 8.1: Listing of all nine flights with the solar zenith angle during the flights and the minimal integration time. Based on this conditions, the flights are divided into three categories: 1, 2, and 3 (see text).

less than $\pm 0.5 \cdot 10^{18}$ molecules cm^{-2} as the category 1 flight, but increases very slowly towards the lower altitudes. It reaches its maximum values between $\pm 0.8 \cdot 10^{18}$and$\pm 1 \cdot 10^{18}$ molecules cm^{-2} at around 5 km. Despite the reduced scattering, the calculated vertical resolution is only slightly larger than the category 1 flight: the vertical resolution starts with 6000 m at 5 km altitude, increases to 1000 m at 20 km, remains better than 1000 m until 30 km altitude, and decreases to 1500 m at 35 km altitude. The reason for the comparable low vertical resolution at 5 and 15 km, is the way of its determination. It depends on the scattering on one hand and on the slope of the vertical columns on the other hand, see subsection 7.3.3. The vertical ozone columns profile determined from the flight data of PIOS VI, remains almost constant at altitudes between 5 and 15 km.

The vertical columns in Figure 8.6 are calculated for the category 3 flight of PIOS VII, 18.7.2005. The scattering in the vertical ozone columns is obviously reduced compared to the category 1 or 2 flights. At high altitudes (≈ 35 km) the scattering is about $\pm 0.1 \cdot 10^{18}$ molecules cm^{-2} and grows to about $\pm 0.3 \cdot 10^{18}$ molecules cm^{-2} at low altitudes (≈ 5 km). The resulting vertical resolution is about 3300 m at 5 km altitude, increases to 1000 m at 15 km altitude, stays well above 500 m between 20 and 30 km altitude, and decreases to 600 m at an altitude of 35 km.

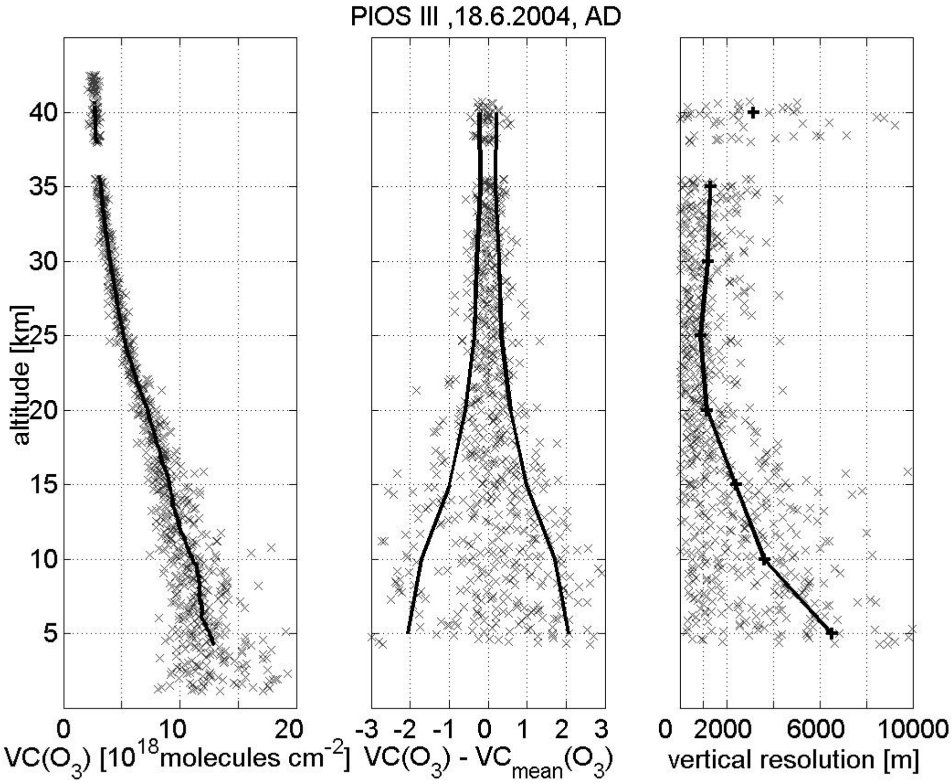

Figure 8.4: Data from PIOS III flight (18.6.2004, Ny-Ålesund); Left: The vertical ozone columns for the wavelength pair combination A and D versus altitude (crosses). The solid line is the averaged profile. Middle: Differences between the single data points and the averaged vertical columns. The solid lines include 70% of all calculated differences. Difference are given in the same unit as the vertical columns [10^{18} molecules cm^{-2}]. Right: The calculated vertical resolution (crosses) and mean values of the vertical resolution for 5 km altitude intervalls.

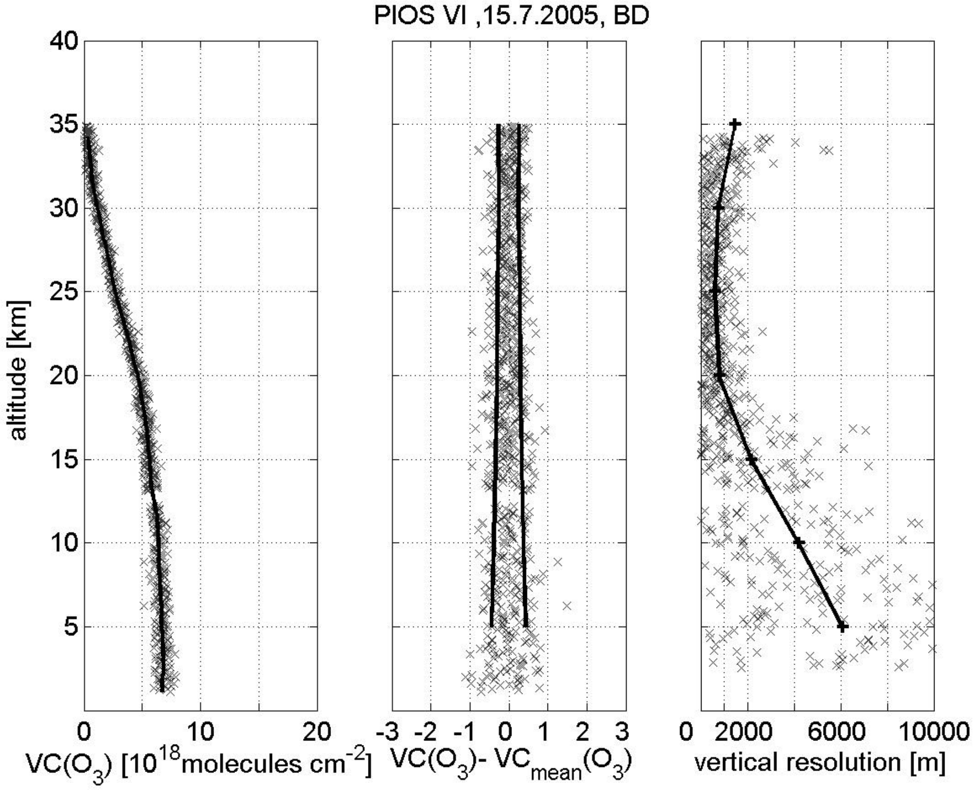

Figure 8.5: Data from PIOS VI flight (15.7.2005,MOHp); Left: The vertical ozone columns for the wavelength pair combination B and D versus altitude (crosses). The solid line is the averaged profile. Middle: Differences between the single data points and the averaged vertical columns. The solid lines include 70% of all calculated differences. Difference are given in the same unit as the vertical columns [10^{18} molecules cm^{-2}]. Right: The calculated vertical resolution (crosses) and mean values of the vertical resolution for 5 km altitude intervalls.

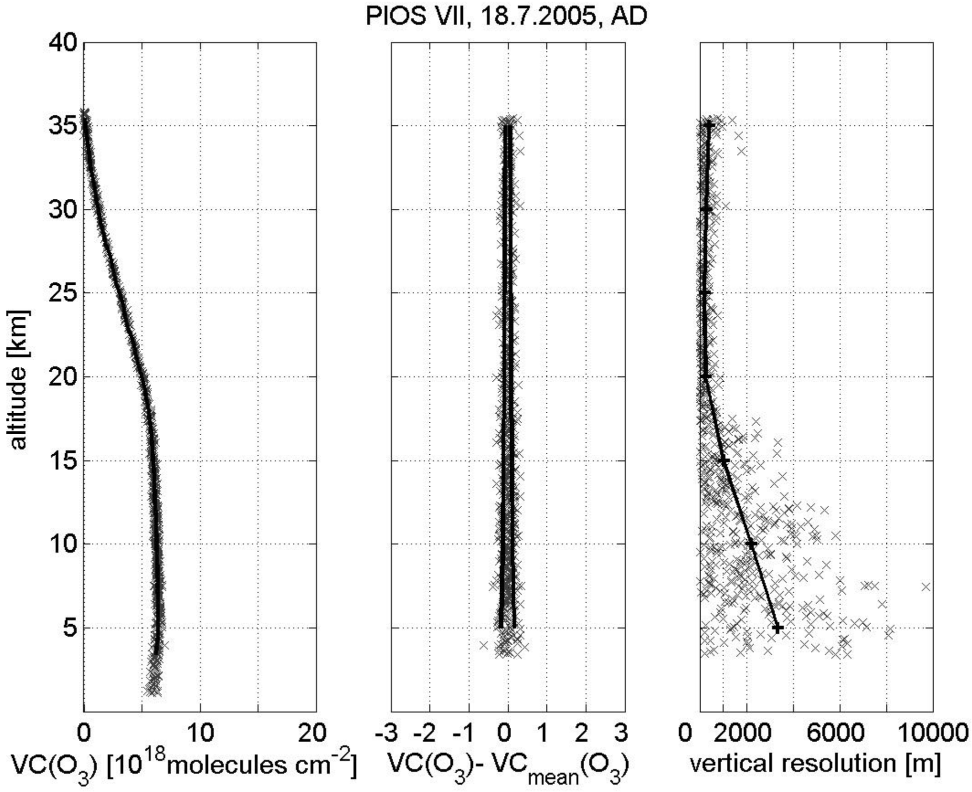

Figure 8.6: Data from PIOS VII flight (18.7.2005,MOHp); Left: The vertical ozone columns for the wavelength pair combination A and D versus altitude (crosses). The solid line is the averaged profile. Middle: Differences between the single data points and the averaged vertical columns. The solid lines include 70% of all calculated differences. Difference are given in the same unit as the vertical columns [10^{18} molecules cm^{-2}]. Right: The calculated vertical resolution (crosses) and mean values of the vertical resolution for 5 km altitude intervalls.

PIOS	λ	5 km	10 km	15 km	20 km	25 km	30 km	35 km
I	AD	17690	3210	2310	**819**	1027	**824**	1370
	BD	9650	1790	2030	870	**950**	1336	nan
II	AD	10580	13580	2970	1031	**910**	**970**	1180
	BD	16120	3770	1670	**926**	1110	1220	2260
III	AD	4220	3110	2410	1210	**942**	1210	1330
	BD	6760	2060	2020	1120	1520	1430	2910
IV	AD	16840	3640	10360	1080	1410	1390	1107
	BD	44440	2700	2390	1250	1820	1620	2160
V	AD	4020	1110	**460**	**290**	**200**	**220**	**310**
	BD	2870	1360	**710**	**340**	**270**	**420**	**550**
VI	AD	229450	4072	1750	**600**	**430**	**520**	**570**
	BD	6090	4200	2170	**810**	**620**	**750**	1470
VII	AD	3370	2230	1020	**260**	**200**	**280**	**400**
	BD	2460	1620	1070	**370**	**310**	**370**	**630**
VIII	AD	2670	1720	**590**	**300**	**190**	**250**	**510**
	BD	2480	4960	**900**	**450**	**290**	**370**	**690**
IX	AD	41690	3390	1800	1300	**670**	**670**	nan
	BD	24510	2660	2290	1390	**854**	1490	nan

Table 8.2: The calculated vertical resolution in [m] for all nine PIOS-flights at different altitudes.

8.2 Ozone profiles

The ozone profiles for all nine flights were calculated by differentiating the vertical columns according to the description in chapter 7. The analysis was performed with the Dobson wavelength pair combination A and D as well as B and D. The profiles were compared with data measured with electrochemical ozone sondes (ECC or Brewer-Mast) and in three cases (12., 15., and 18.7.2005 in Hohenpeißenberg additonally with ozone LIDAR measurements.

8.2.1 Ozone profiles: Ny-Ålesund

The four launches PIOS I - IV performed in June 2004 in Ny-Ålesund have been analysed. The resulting ozone number density profiles are compared with the electrochemical sondes, launched at Koldewey-Station.
All four flights are belonging into category 1, regarding the low sun elevation and the short integration time.

PIOS I: 10.6.2004

The obtained profiles for the launch of PIOS I, 10.6.2004 are shown in Figure 8.7. A high vertical resolution with values smaller than 1000 m was calculated for the AD wavelength combination between 18 and 27 km altitude, and for the BD wavelength combination between 18 and 22 and between 28 and 32 km altitude. The ECC-sonde was launched with a time delay of 24 h on 11.6.2004.
The AD-profile shows for the low altitudes between 5 and 17 km an oscillating structure around an ozone number density of about $3.5 \cdot 10^{12}$ molecules cm^{-3} without any similarities to the ECC-profile. The relative differences exceed 100%. The ozone profile of the BD wavelength combination overestimates the ECC-profile below 10 km by more than 100% . Between 10 and 20 km it does not detect the small-size structures of the ECC-profile, but follow the large-scale increasing of the ozone values. Relative differences are between 10% to 20%, with one exception: 90% relative difference at 15 km altitude.
Between 18 and 31 km altitude the relative differences between the ozone concentration of both PIOS profiles and of the ECC-profile are below 20%.
The highest calculated value in 32 km altitude is for both wavelength combinations about 30% smaller than the corresponding ECC ozone number density.

PIOS II: 12.6.2004

Figure 8.8 displays the calculated profiles for the launch of PIOS II on 12.6.2004. The AD-profile has a high vertical resolution of less than 1000 m between 23 and 30 km. The values of the vertical resolution of the BD-profile fall below 1000 m in the altitude range between 18 and 22 km.
The profiles can be compared to the ozone profile measured by the ECC-sonde launched the day earlier (11.6.2004).

The ozone number densities of the AD-profile show an oscillating structure between 5 and 15 km and differ by more than 100% from the ECC profile. The BD-profile differs between 50% and 100% at the first five kilometers (5 - 10 km). It follows the qualitative structure of the ECC profile in the altitude interval between 10 km and 15 km, where it shows differences between 20% and 30%.
Between 15 and 25 km altitude the differences between the PIOS profiles and the ECC profile are between 0% and 50%. The ozone maxima calculated from the PIOS profiles shows the same extent as the ECC profile, but overestimates the maximum by 30% and do not capture the double structure.
Above 25 km the ozone profiles agree within 20%.

PIOS III: 18.6.2004

The profiles in Figure 8.9 were obtained from the start of PIOS III on 18.6.2004. In the height intervall between 18 km and 22 km a high vertical resoltion with values below 1000 m is calculated for the AD-profile. The vertical resolution of the BD-profile always exceeds 1000 m.
Due to the transmission failure during the ascent (chapter 6) no ozone values could be calculated for the altitude intervall between 34 and 38 km. For the AD-profile two further ozone values are calculated for 39 and 40 km altitude, showing typical values of about $1 \cdot 10^{12}$ molecules cm^{-3}.
The ECC-sonde for the comparison was launched the same day with a time delay of 30 minutes.
Between 5 km and 12 km altitude the AD-profile and BD-profile show an oscillating structure. The relative differences to the ECC-profile are between 20% and 100% for the BD-profile and exceed 100% for the AD-profile.
Between 13 and 24 km the AD- and BD-profiles are very close to each other. The differences to the ECC-profile are between 10% and 50%. The vertical extenst of the ozone maximum is two kilometers smaller in the PIOS profiles. The maximum value of $4.5 \cdot 10^{12}$ molecules cm^{-3} is met by the BD-profile. The peak values of the BD-profile are found between 20 and 21 km with differences of lass than 10% compared to the ECC-profile.
Above 25 km altitude the AD-profile differs less than 10% from the ECC-profile up to the maximum altitude of the ECC-profile at 32 km. The BD-profile shows slightly larger differences to the ECC-profile of about 10% to 15% between 25 and 30 km.

PIOS IV: 24.6.2004

PIOS IV was launched on the 24.6.2004 and the obtained profiles are shown in Figure 8.10. Neither the AD-, nor the BD-profile, show a vertical resolution with values smaller than 1000 m.
The ECC-sonde was launched about 30 minutes after the PIOS sonde.

The AD-profile differs significantly from the ECC-profile by more than 100% in the lower altitudes. Between 10 and 20 km the relative differences lay between 10% and 50%.

The BD-profile differences exceed 100% in the lowest altitudes between 5 and 10 km . Between 10 and 20 km it captures qualitatively the ECC ozone profile, differing about 30% to 50%. The lower maximum in 11 km is detected with only 10% difference to the ECC value and the ozone values of the main maximum between 17 and 23 km differs less than 20%.

Above 21 km the AD-profile shows smaller ozone values than the ECC-profiles, but follows qualitatively the ozone decrease with altitude. Differences are less than 20%. The BD-profile shows increasing differences to the ECC-profile from less than 30% at about 23 km altitude to about 50% between 25 and 30 km. The differences exceed 50% above 30 km altitude. Additionally, a raising oscillating structure is visible in the BD-profile.

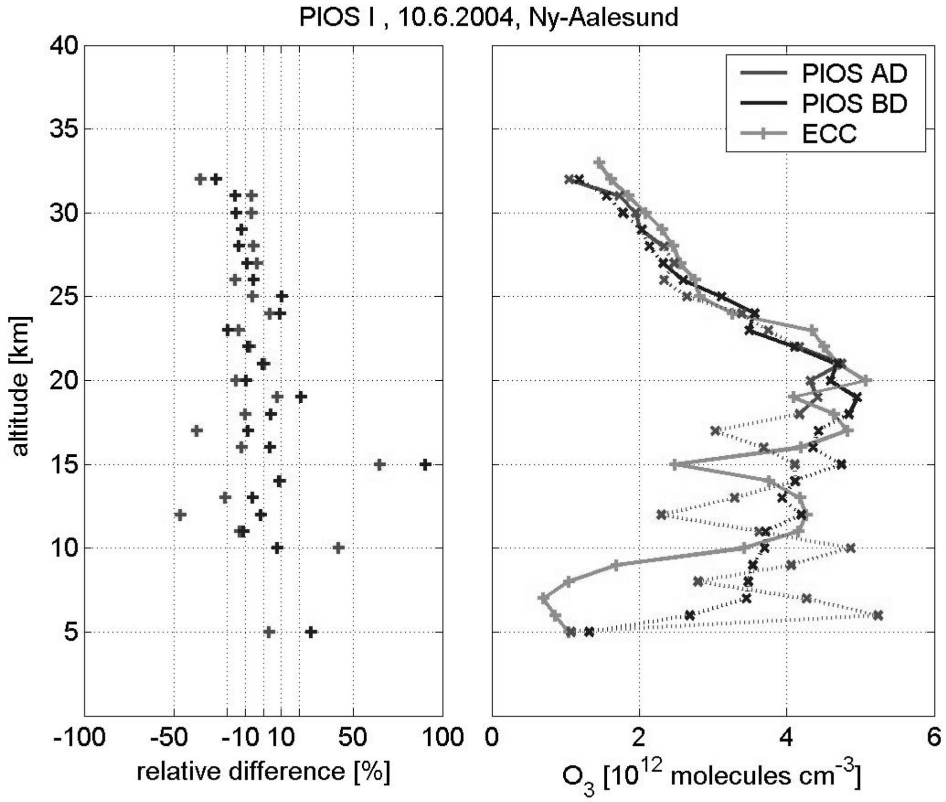

Figure 8.7: Calculated ozone profiles for the start on 10.6.2004 in Ny-Ålesund and relative differences to the ECC-sonde (11.6.2004). The profiles (right panel) for PIOS were calculated with the wavelength combination AD (red) and BD (blue) and compared to the ECC sonde (green). The PIOS profiles are plotted with solid lines for a high vertical resolution < 1000 m and with dotted lines for a low vertical resolution > 1000 m. In the left panel the relative differences between the ECC sonde and the PIOS profiles are shown: red for the AD-profile and blue for the BD-profile.

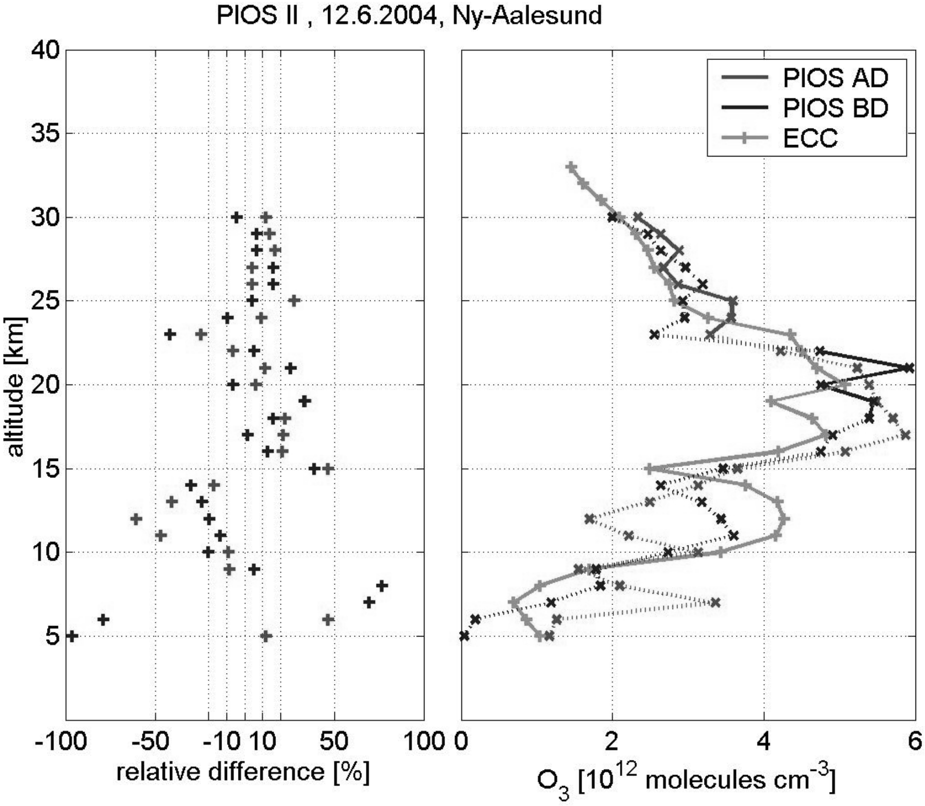

Figure 8.8: Calculated ozone profiles for the start on 12.6.2004 in Ny-Ålesund and relative differences to the ECC-sonde (11.6.2004). The profiles (right panel) for PIOS were calculated with the wavelength combination AD (red) and BD (blue) and compared to the ECC sonde (green). The PIOS profiles are plotted with solid lines for a high vertical resolution < 1000 m and with dotted lines for a low vertical resolution > 1000 m. In the left panel the relative differences between the ECC sonde and the PIOS profiles are shown: red for the AD-profile and blue for the BD-profile.

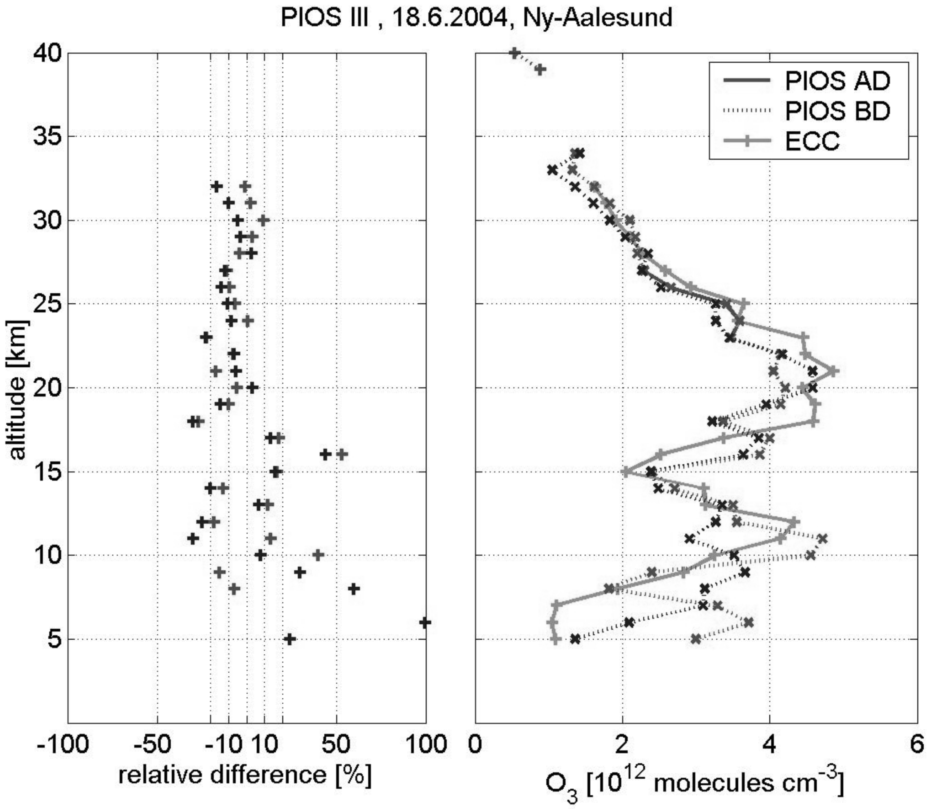

Figure 8.9: Calculated ozone profiles for the start on 18.6.2004 in Ny-Ålesund and relative differences to the ECC-sonde (18.6.2004). The profiles (right panel) for PIOS were calculated with the wavelength combination AD (red) and BD (blue) and compared to the ECC sonde (green). The PIOS profiles are plotted with solid lines for a high vertical resolution < 1000 m and with dotted lines for a low vertical resolution > 1000 m. In the left panel the relative differences between the ECC sonde and the PIOS profiles are shown: red for the AD-profile and blue for the BD-profile.

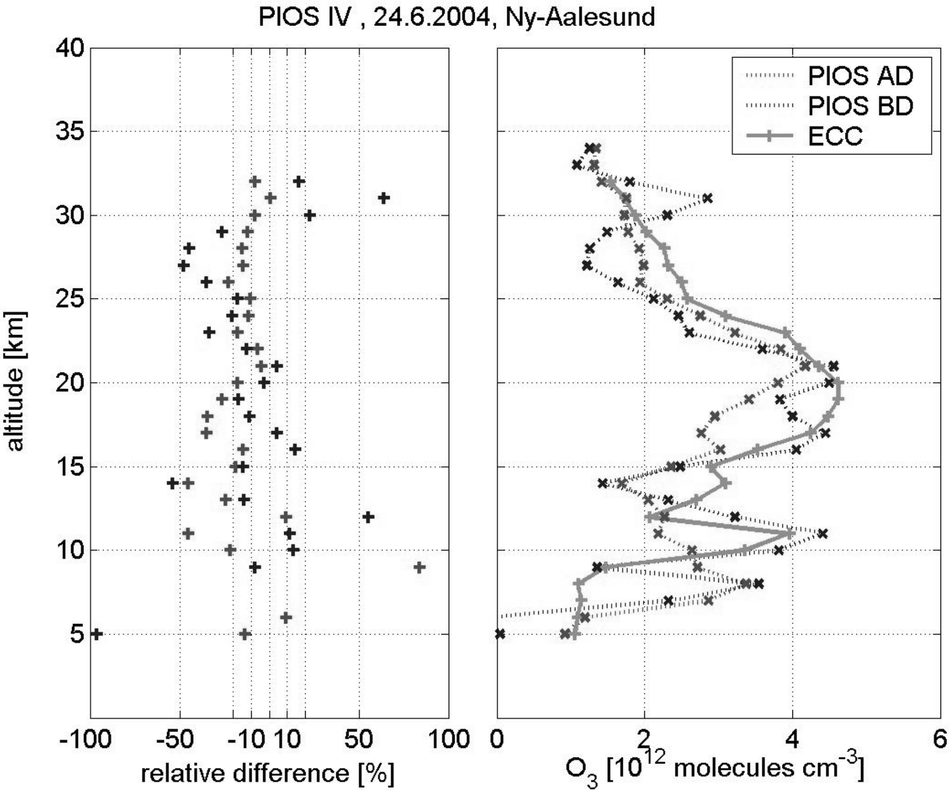

Figure 8.10: Calculated ozone profiles for the start on 24.6.2004 in Ny-Ålesund and relative differences to the ECC-sonde (24.6.2004). The profiles (right panel) for PIOS were calculated with the wavelength combination AD (red) and BD (blue) and compared to the ECC sonde (green). The PIOS profiles are plotted with solid lines for a hihg vertical resolution < 1000 m and with dotted lines for a low vertical resolution > 1000 m. In the left panel the relative differences between the ECC sonde and the PIOS profiles are shown: red for the AD-profile and blue for the BD-profile.

8.2.2 Ozone profiles, Hohenpeißenberg

In July 2005, five optical sondes were launched at the Meteorological Observatory Hohenpeißenberg. The obtained profiles from the three first flights (12.,15, and 18.7.2005) are compared with the measurements of the simultaneous started electrochemical Brewer-Mast sondes and with LIDAR measurements.
Flights V, VII, and VIII are category 3 measurements while flights VI and IX are category 2 measurements.

PIOS V: 12.7.2005

PIOS V was launched on the 12.7.2005 and the obtained ozone profiles are shown in Figure 8.11.
A high vertical resolution of the AD- and the BD-profile with values below 1000 m is calculated at altitudes above 13 km.
The Brewer-Mast ozone sonde was launched immediately after the PIOS sonde with a time delay of less than 5 minutes. The LIDAR measurements were performed in the night from 13. to 14.7.2005.
Above 7 km altitude both PIOS profiles follow generally the ozone profile measured with the ECC-sonde. Between 10 and 15 km the differences between the ozone profiles of PIOS and the ECC-profile are mostly within 20% and rarely reaching 50%. Between 15 and 20 km, the PIOS profiles are comparable to the LIDAR-profile. LIDAR and PIOS detect a local minimum at about 16 km of $\approx 2 \cdot 10^{12}$ molecules cm^{-3}. The measured vertical extent of that minimum is with 3 km significantly larger in the PIOS-data than in the LIDAR-measurements (1 km).
At the altitude of the main ozone maximum (20 to 25 km) the differences between the BD profile to the other measurement systems are within 10%. The AD- profile show ozone values which are 10 - 15% smaller than the ozone values of LIDAR- and Brewer-Mast measurements.
Between 25 and 30 km both PIOS profiles agree with the Brewer-Mast and the LIDAR profile within 10%. The differences between the AD-profile and the comparison measurements remain lower than 10% up to 33 km, the BD profile shows raising differences between 10 and 20%.
Large differences of about 30% and about 70% are visible between the PIOS measurements and the LIDAR measurements at altitudes between 34 and 35 km.

PIOS VI: 15.7.2005

The profiles in Figure 8.12 were obtained from the start of PIOS VI on 15.7.2005. Both PIOS profiles have a high vertical resolution with values smaller than 1000 m above an altitude of 18 km.
The Brewer-Mast sonde was launched shortly (5 minutes) after the PIOS sonde. LIDAR measurements were performed during the following night (15.-16.7.2005).

Between 5 and 10 km altitude, the AD-profile has ozone values which are smaller than the Brewer-Mast values and differs by 50% and more. The BD-profile shows for the same altitude interval values which are 30% smaller than the ozone values of the Brewer Mast profile.

Between 10 and 20 km the BD-profile shows qualitatively the structures of the Brewer-Mast and LIDAR ozone profile, and differs less than 30%. Large deviations are found in the altitude range between 14 and 15 km, where the differences increase 50%. The AD-profile underestimates the ozone values between 10 and 20 km by about 50%.

During the next 10 km (20 - 30 km) the PIOS ozone profiles are 10 - 20% smaller than the comparison measurements. Above 30 km the differences raise to 40% for the BD-profile, whereas the AD-profile differs still less than 20%.

PIOS VII: 18.7.2005

Figure 8.13 displays the calculated profiles for the launch of PIOS VII on 18.7.2005. For altitudes above 18 km both PIOS profiles have a high vertical resolution with values smaller than 1000 m

The Brewer-Mast sonde was launched immediately after the PIOS launch with a time delay of less than 5 minutes. LIDAR measurements were performed in the previous night (17.-18.7.2005).

The AD-profile shows between 5 and 15 km smaller values than the ozone profile of the Brewer-Mast sonde. Differences are higher than 50%. In contrast, the BD-profile matches the Brewer-Mast profile. The differences remain smaller than 30%.

With on exception, the increase of the ozone number density between 15 and 20 km is detected within 20% agreement for all measured ozone profiles. Only at 17 km altitude the LIDAR- and the BD- ozone values differ by 50%.

Above 20 km the differences between the ozone values of PIOS and of the comparison measurements are not exceeding 20% until 28 km (AD) and 29 km (BD). At about 30 km altitude both PIOS profiles exhibit a structure, indicating 20% smaller values than the LIDAR measurements at the same altitude. Between 31 and 34 km the differences are reduced to about 10%. At the highest altitude, the PIOS-profiles (35 km) show relative differences of ±30% compared to the LIDAR profile.

PIOS VIII: 20.7.2005

The profiles of the PIOS VIII flight (20.7.2005) are plotted in Figure 8.14. A high vertical resolution for the AD and BD profiles with values smaller than 1000 m is calculated for altitudes above 13 km.

The Brewer-Mast sonde was launched after the PIOS sonde with a time delay of maximal 5 minutes.

Between 5 and 10 km both profiles (AD and BD) show differences of about 50%. The BD-profile remains smaller than the Brewer-Mast profile, whereas the AD-profile tends to minor oscillations.

The ozone values of the BD-profile are smaller than the ozone values of the Brewer-Mast profile for altitudes below 25 km, showing differences of 50% between 10 and 15 km, decreasing to about 20% between 15 and 25 km. The ozone profile of PIOS, calculated with the AD combination is very close to the ozone profile of the Brewer-Mast sonde between 9 and 13 km altitude, differing between 5 to 20%. Between 13 and 25 km altitude the ozone values of the AD-profile are about 20% smaller than the ozone values of the Brewer-Mast profile.

Above 25 km, both PIOS ozone profiles show less than 10% differences to the Brewer-Mast ozone profile. In 30 and 31 km altitude the difference to the Brewer-Mast sonde is about 20%.

Above the highest alitude of the Brewer-Mast sonde, the both PIOS profiles are very close to each other, and show a reasonable structure.

PIOS IX: 21.7.2005

Figure 8.15 shows the ozone profiles of the last PIOS flight, carried out on the 21.7.2005. A high vertical resolution with values below 1000 m is calculated for the AD-profile at alitudes above 23 km. The BD-profile has a high vertical resolution with values smaller than 1000 m for the altitude range between 23 and 27 km.

The Brewer-Mast sonde was launched less than 5 minutes after the PIOS sonde. Between 5 and 10 km altitude the AD-profile shows 10 to 50% smaller ozone values than the Brewer-Mast profile, whereas the BD-profile has 10 to 70% larger ozone values.

Between 11 and 14 km the Brewer-Mast measurement shows a local maximum, which is not seen in the PIOS-profiles. They show ozone values 20 to 50% smaller than the Brewer-Mast ozone values at that altitude.

Between 15 and 20 km the differences between the PIOS-profiles and the Brewer-Mast profile are less than 15%.

From 20 km up to 30 km the AD profile differs less than 20% from the Brewer-Mast profile. The structure of the main ozone maximum as measured by the Brewer-Mast sonde, is captured by the BD-profile. Between 22 and 29 km the differences are less than 10%.

Above 30 km the AD-profile follows very close the Brewer Mast profile with differences of less than 10%, whereas the BD-profile differs about 20%.

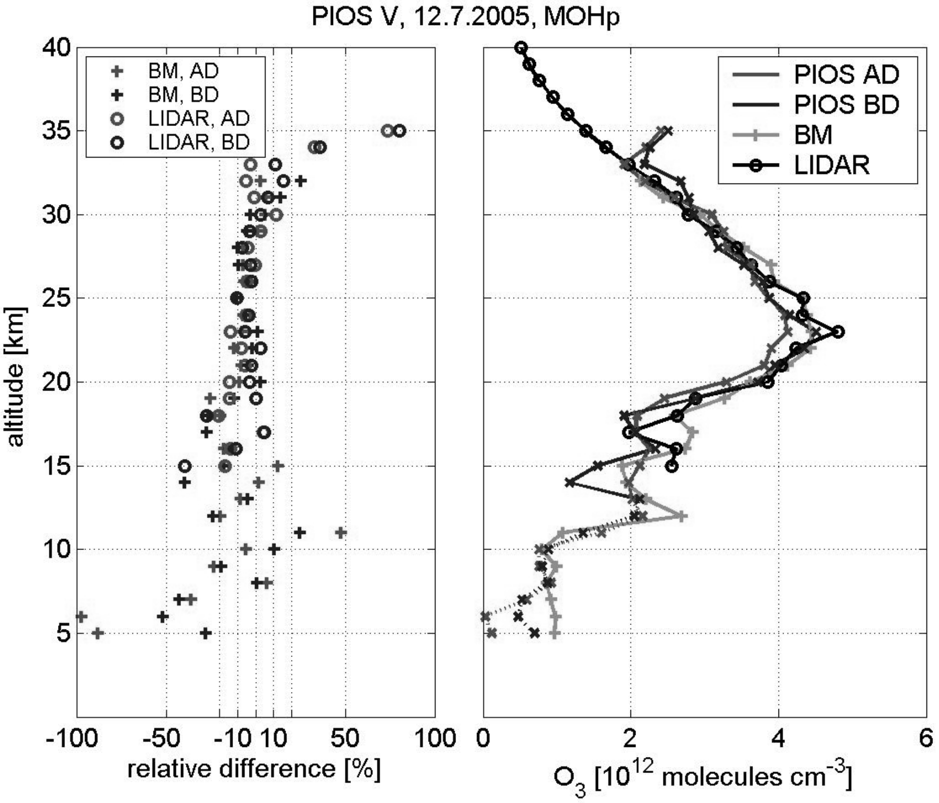

Figure 8.11: Calculated ozone profiles for the start on 12.7.2005 in Hohenpeißenberg and relative differences to the Brewer-Mast sonde (12.7.2005) and the LIDAR measurements (13.7.2005). The profiles (right panel) for PIOS were calculated with the wavelength combination AD (red) and BD (blue) and compared to the Brewer-Mast sonde (green) and the LIDAR measurements (black) . The PIOS profiles are plotted with solid lines for a high vertical resolution < 1000 m and with dotted lines for a low vertical resolution > 1000 m. In the left panel the relative differences between the Brewer-Mast sonde (crosses) and the PIOS profiles, and between the LIDAR (circles) and the PIOS profiles are shown: red for the AD-profile and blue for the BD-profile.

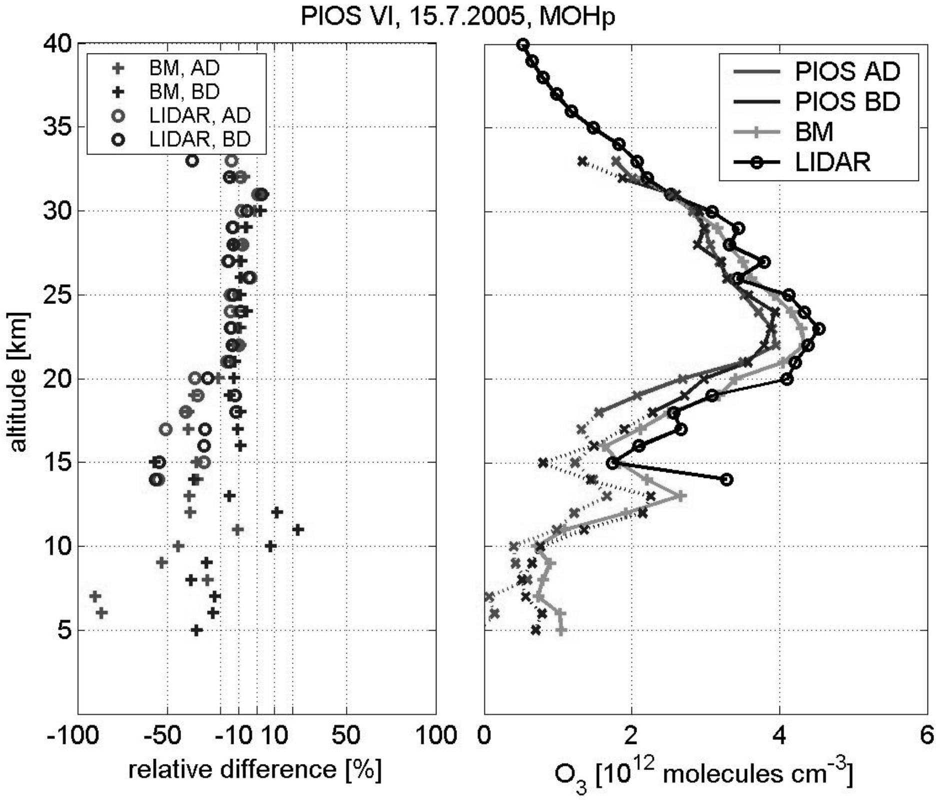

Figure 8.12: Calculated ozone profiles for the start on 15.7.2005 in Hohenpeißenberg and relative differences to the Brewer-Mast sonde (15.7.2005) and the LIDAR measurements (15.7.2005). The profiles (right panel) for PIOS were calculated with the wavelength combination AD (red) and BD (blue) and compared to the Brewer-Mast sonde (green) and the LIDAR measurements (black). The PIOS profiles are plotted with solid lines for a high vertical resolution < 1000 m and with dotted lines for a low vertical resolution > 1000 m. In the left panel the relative differences between the Brewer-Mast sonde (crosses) and the PIOS profiles , and between the LIDAR (circles) and the PIOS profiles are shown: red for the AD-profile and blue for the BD-profile.

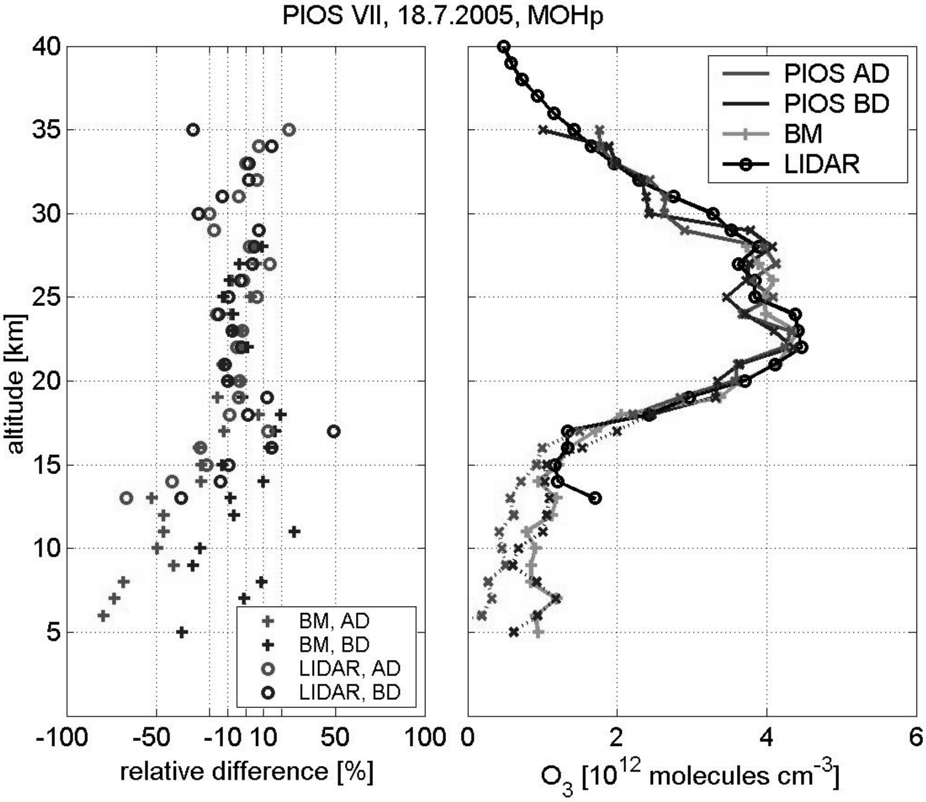

Figure 8.13: Calculated ozone profiles for the start on 18.7.2005 in Hohenpeißenberg and relative differences to the Brewer-Mast sonde (18.7.2005) and the LIDAR measurements (17.7.2005). The profiles (right panel) for PIOS were calculated with the wavelength combination AD (red) and BD (blue) and compared to the Brewer-Mast sonde (green) and the LIDAR measurements (black). The PIOS profiles are plotted with solid lines for a high vertical resolution < 1000 m and with dotted lines for a low vertical resolution > 1000 m. In the left panel the relative differences between the Brewer-Mast sonde(crosses) and the PIOS profiles, and between the LIDAR (circles) and the PIOS profiles are shown: red for the AD-profile and blue for the BD-profile.

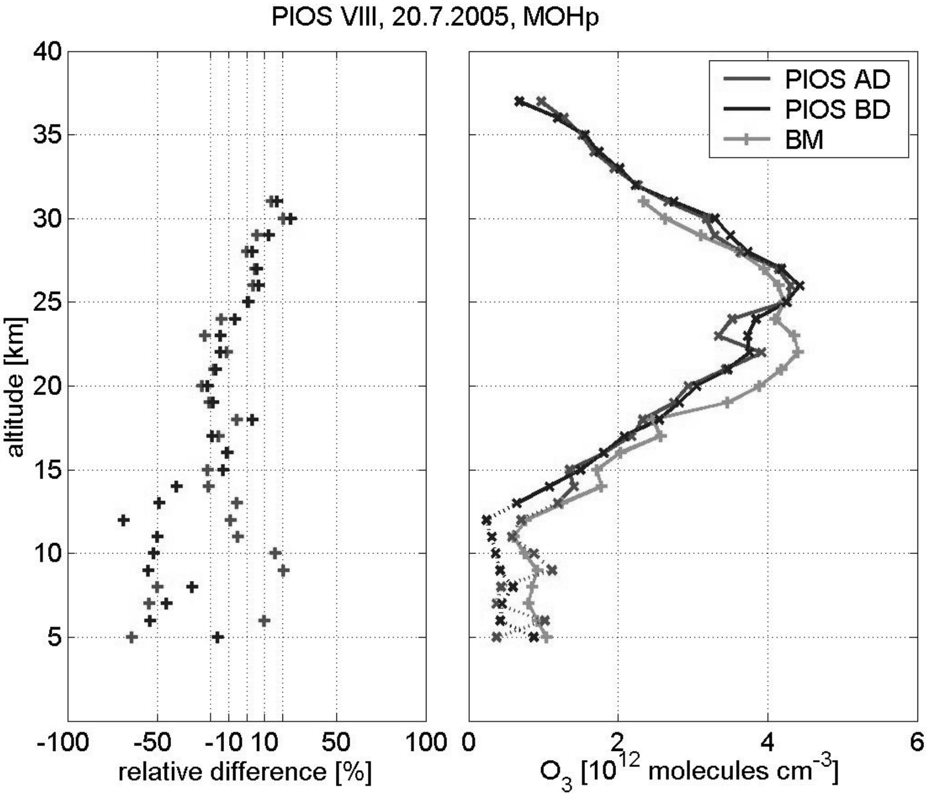

Figure 8.14: Calculated ozone profiles for the start on 20.7.2005 in Hohenpeißenberg and relative differences to Brewer-Mast sonde (20.7.2005). The profiles (right panel) for PIOS were calculated with the wavelength combination AD (red) and BD (blue) and compared to the Brewer-Mast sonde (green). The PIOS profiles are plotted with solid lines for a high vertical resolution < 1000 m and with dotted lines for a low vertical resolution > 1000 m. In the left panel the relative differences between the Brewer-Mast sonde and the PIOS profiles are shown: red for the AD-profile and blue for the BD-profile.

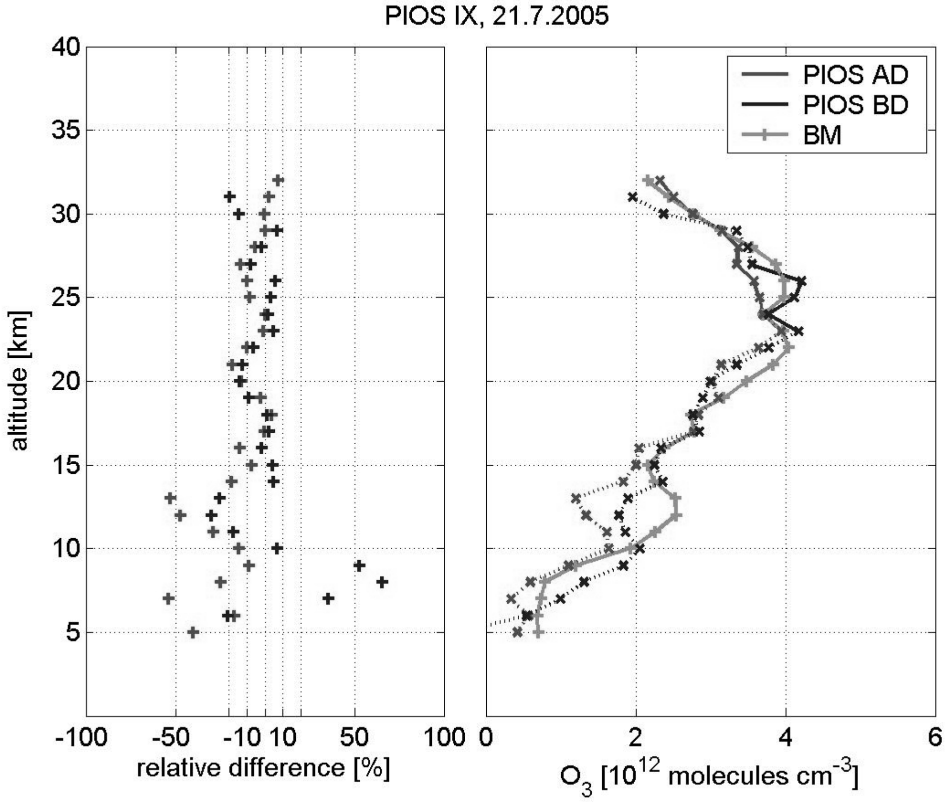

Figure 8.15: Calculated ozone profiles for the start on 21.7.2005 in Hohenpeißenberg and relative differences to the Brewer-Mast sonde (21.7.2005). The profiles (right panel) for PIOS were calculated with the wavelength combination AD (red) and BD (blue) and compared to the Brewer-Mast sonde (green). The PIOS profiles are plotted with solid lines for a high vertical resolution < 1000 m and with dotted lines for a low vertical resolution > 1000 m. In the left panel the relative differences between the Brewer-Mast sonde and the PIOS profiles are shown: red for the AD-profile and blue for the BD-profile.

8.3 Other trace gases

In the wavelength range between 400 and 500, NO_2 has some absorption lines as shown in Figure 8.16 for the wavelength range from 425 nm to 450 nm (Harwood and Jones 1994). The absorption cross sections in Figure 8.16 are from Harwood and Jones (1994), selected for 223 K . In the wavelength range between 425 and 450 nm, NO_2 shows enhanced absorption at about 428 , 431, 435, 439, 445, and 448 nm. The irradiance spectrum, measured at 15 km altitude (Figure 8.17) shows significant structures at wavelengths 431, 434, 439, 446, and 449 nm. The latter four are all in the same order of magnitude and may result from the absorption of the NO_2 in the atmosphere. The larger structure at 431 nm, is rather caused by a tilt-problem, as described in detail by Sioris et al. (2003). Since the abundance of stratospheric NO_2 is very low compared to ozone, the expected changes in the irradiance spectra with altitude are very small.

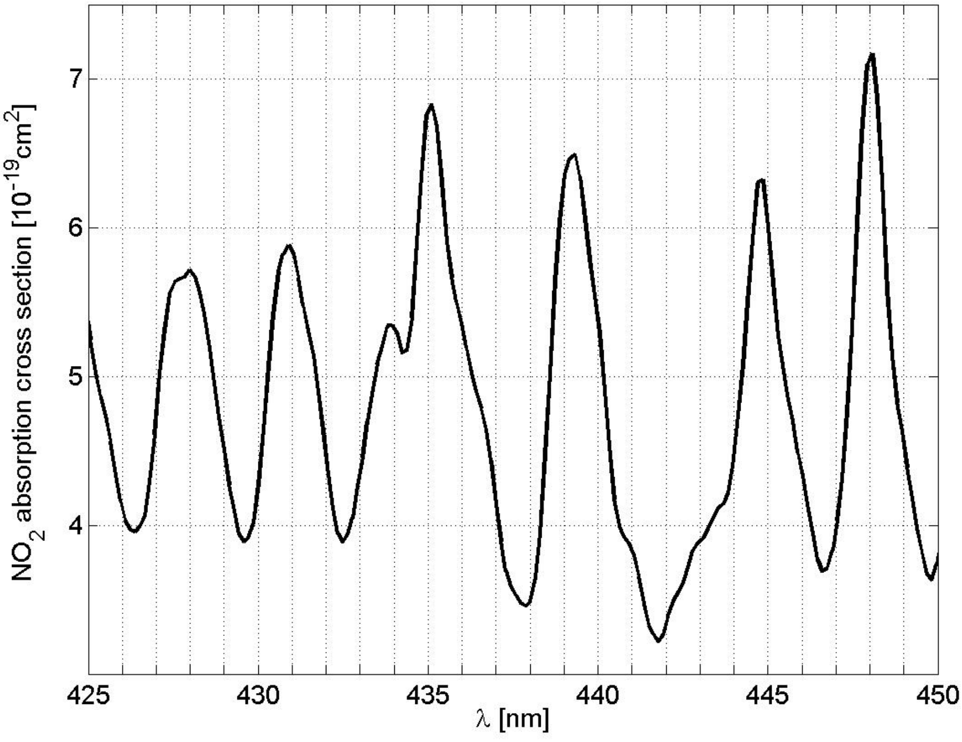

Figure 8.16: NO_2 absorption cross section in the wavelength range between 425 and 450 nm at a temperature of 223 K.

In order to check for any changes with altitude, the irradiance spectrum at 35 km is divided by the spectrum at 15 km. For the wavelength outside the NO_2

absorption line almost no changes should be visible, i.e. the ratio is expected to be around 1. To consider the changes of the sun elevation, the resulting ratio was mulitplied by the reciprocal value of the mean ratio. The negative logarithm of the corrected ratio is shown in Figure 8.18 between 435 and 450 nm. For the wavelengths, where the irradiances spectrum at 35 km altitudes show higher values than in 15 km altitude, the calculated ratio is larger 1 and the logarithm of the ratio is positive. Thus, absorption between this layers results in negative peaks, when plotting the negative logarithms of the ratios. The detected absorption at 439, 444, and 447 nm are very likely caused by the enhanced absorption of NO_2 at 439, 445 and 448 nm (Figure 8.18).

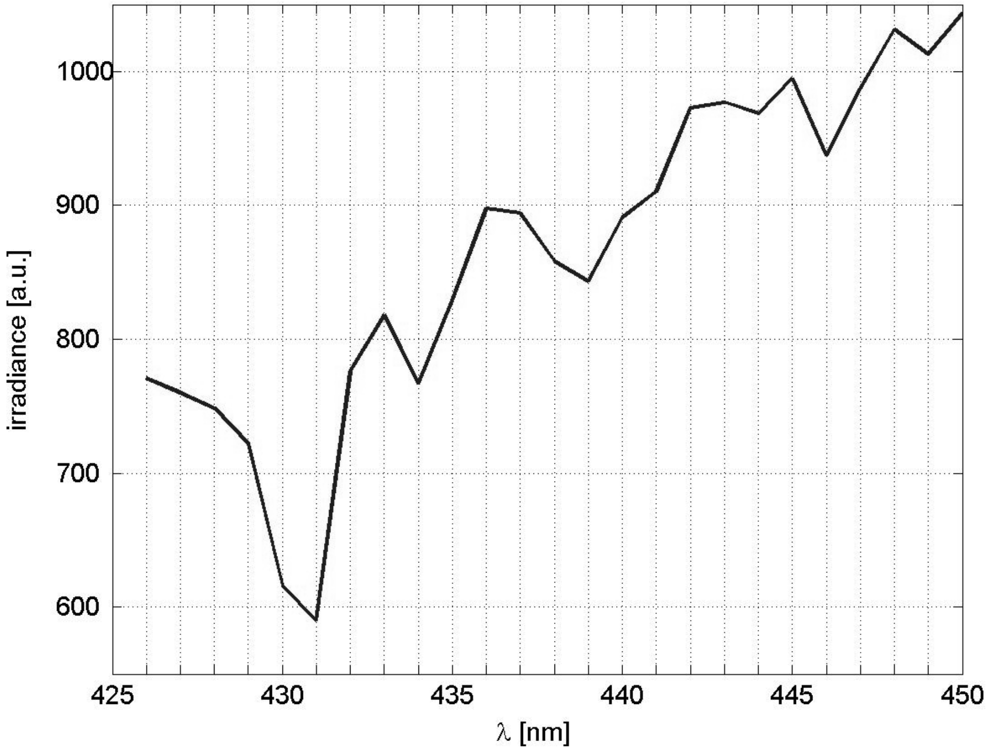

Figure 8.17: Measured spectra in the wavelength range between 425 and 450 nm in 15 km altitude, data are taken from PIOS IV launch, 24.6.2004.

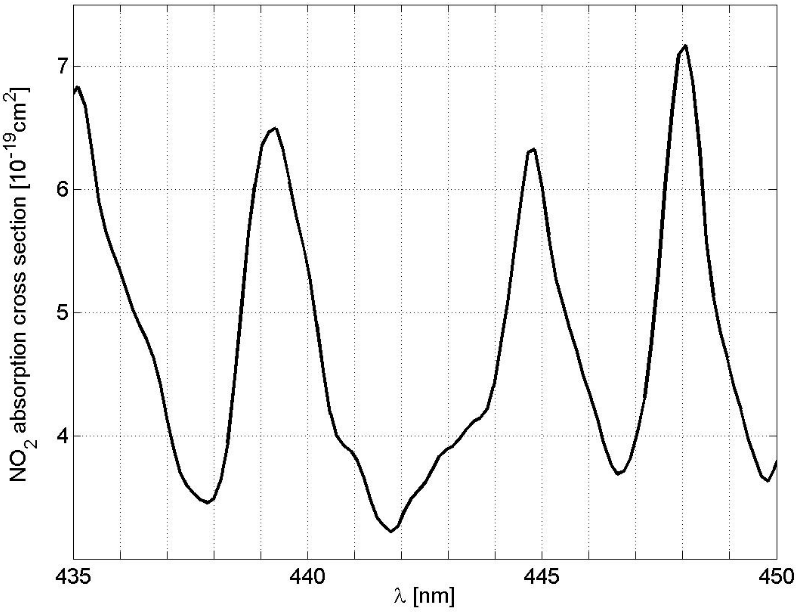

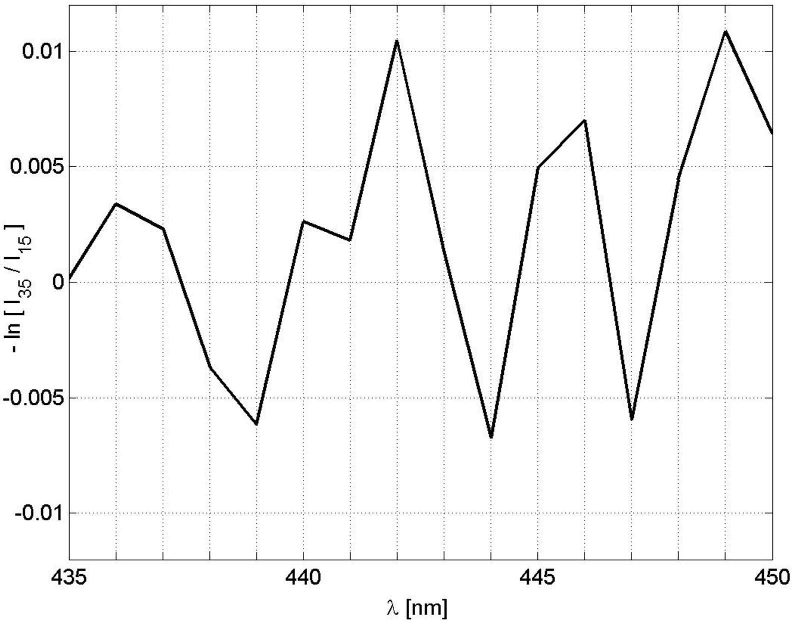

Figure 8.18: Top: NO_2 absorption cross sections in the wavelength range between 435 and 450 nm at a temperature of 223K. Bottom: Negative logarithm of the ratio of the irradiance spectra in 35 and 15 km altitude for the wavelength range between 435 and 450 nm

8.4 Discussion

The new PIOS instrument measures continuously reliable irradiance spectra in a preselected wide wavelength range during the ascent through the atmosphere. The precision of the measured irradiance spectra is sufficiently to observe changes with altidude. These changes are further used to extract the vertical distribution of absorbing trace gases. For example, the decreasing absorption with increasing altitude due to ozone is clearly visible in the spectral measurements in the UV wavelength range.

The flights were divided into three different categories based on the measurement conditions. Category 1 flights were performed at high solar zenith angles with a short integration time, category 2 flights were performed at low solar zenith angles with a short integration time, and category 3 flights were performed at low solar zenith angles with a long integration time.

The ozone profiles for the category 3 flights agree very well with ozone profiles obtained with Brewer-Mast sondes and LIDAR measurements in the stratosphere. All three flights show in the altitude range between 18 and 35 km high vertical resolutions between 200 and 400 m.

The ozone profiles of the category 2 flights show good agreement with the comparison measurements for the altitudes above 15 km. In the lower stratosphere the ozone profiles capture qualitatively the structure in the ozone profiles of the other measurements.

Even the ozone profiles of the category 1 flights show reliable agreement with the ozone profiles of the ECC-sonde for altitudes above 20 km.

As expected, a clear improvement of the obtained ozone profiles was achieved from the category 1 flights to the category 3 flights. The more favourable measurement conditions for category 3 flights allowed the detection of larger irradiance signals, due to the higher sun elevation and the longer integration period of the PIOS sensor. Thus improved the signal to noise ratio for the irradiance measurements and subsequently for the calculated vertical columns, which allows for a more reliable ozone profile retrieval.

However, almost overall the discrepancies between the PIOS ozone profiles and the ozone profiles of the comparison measurements decreased towards higher altitudes. This is due to the fact that the ozone retrieval is based on the assumption that only direct irradiance is detected. This assumption is not valid for lower altitudes. The ozone values calculated at the maximum altitudes show larger discrepancies to the comparison measurements. This is very likely caused by the estimation of the extraterrestrial radiation based on the measurements at the highest altitude and the assumption of a non-varying ozone column above. This estimation considers insufficiently any local and temporal variations. The measurement of the extraterrestrial radiation by the PIOS instrument itself would render the estimation unecessary.

In general, the calculated vertical resolution corresponds with the discrepancies

between the PIOS ozone profiles and the ozone profiles of the comparison measurements. High vertical resolutions ($< 1000\,\mathrm{m}$) of the ozone profile of the PIOS sonde match with small deviations ($< 20\%$) between the ozone profiles of the PIOS and the comparison measurements.
The vertical resolution is a criterion for the reliability of the obtained ozone profiles. It determines the minimum altitude intervall needed to detect signal changes, which are significantly higher then the noise of the vertical columns (chapter 7). The calculation of the vertical resolution is based on the vertical columns determined from the measurements, thus being influenced by the current ozone distribution and also by possibly wrong detected data. Therefore, the determination of the instrument's possible vertical resolution is not a totally independent evaluation tool
Ozone profiles were calculated with the adapted algorithm for Dobson spectrometers, using combinations of wavelength pairs to obtain the vertical column above the instrument. The ozone profiles calculated using the shorter wavelengths (AD) show generally a better agreement with the comparison measurements at higher altitudes. Whereas the use of the longer wavelengths (BD) results in a better agreement between PIOS ozone profile and ozone profile of the comparison measurements at lower altitudes.
That reflects the fact that the relative contribution of the wavelengths absorbing ozone is changing to longer wavelengths towards lower altitudes Brasseur and Solomon (1986), and subsequently the irradiance at shorter wavelengths is decreasing towards lower altitudes as can be seen in the cut-off of the UV spectrum in Figure 8.1.
The longer integration time of the three PIOS sondes in Hohenpeißenberg improved obviously the quality of the ozone profiles because of an increased signal to noise ratio in the irradiance measurements. That results in a smaller noise of the calculated vertical columns and allows to determine the ozone profile more precisely. For example, the ozone profiles of the category 3 flights showed good agreement with the ozone profiles of the comparison measurements for altitudes below 20 km, whereas the category 1 flights could capture the ozone profile in most cases only qualitatively.

In the troposphere all nine flights show a very low vertical resolution of a few thousand meters. In the troposphere the made assumption in the analysis algorithm of only detecting direct light is not valid anymore. Furthermore, the approximation applied for the Rayleigh scattering may not be sufficient for the increased scattering in the troposphere. Therefore, in the troposphere, the PIOS instrument can not detect the changes in the vertical column with a sufficiently high vertical resolution. That is reflected in the determined ozone profiles for that altitude range: differences to the ozone profiles of the electrochemical sondes at 50% or higher. Sometimes the differences are even higher than 100%.

For one flight the irradiance spectra measured at two altitudes in the visible wavelength range between 435 and 450 nm were compared. Absorption structures, which correspond with the known absorption lines of NO_2 could be identified. However, the quantification of the amount of NO_2 from these absorption structures requires the development of an algorithm which allows the retrieval of the abundance of comparable weak absorbers and probably further improvements in the precision of the irradiance measurements.

Chapter 9

Conclusions

A new sounding system based on an optical method was developed for measurements of the distribution of stratospheric trace gases. It contains a small, light-weight balloon-borne optical sonde, which transmits the data to a portable groundstation. The hardware components of the system are commercially available. Currently the total cost of the sonde is in the order of 5000,- €. Due to the design and the setup of the sonde, the handling of the system is rather straightforward. For example the preparation of the sonde before the launch needs less time than the preparation of a standard ECC sonde. Launches independent from special launching sites are possible because of the autonomous telemetry system and the portable groundstation.

The system was intensively tested and continuously optimised. The achieved actual technical status guarantees reliable measurements. The measured solar irradiance spectra and the meteorological data together with the GPS position are transferred with the radio transmitter to the groundstation.

The optical characteristics of the spectrometer are depending on the ambient temperature conditions. Even though the sensor will experience rather large temperature changes during a balloon ascent through the atmosphere, an active temperature control system was abandoned because of the additional weight and power consumption. Extensive laboratory experiments were performed to identify the influence of temperature changes on the spectrometer.

The temperature induced wavelength shift, the signal changes, and the dark current behaviour were quantified. Based on the optical characterisation of the sonde, in-flight corrections methods were developed to compensate for the effects of temperature changes. In future, preflight characterisations of the sensor in the laboratory become therefore obsolete.

The recovery probability of a launched sonde is very high in populated areas. The design and the construction of the sonde make multiple deployment of the same sonde possible. The avoidance of any moving part in the design makes the sonde rather robust. Therefore, the polystyrene box offers sufficient protection to prevent damage of the spectrometer and of the radiosonde. Several sondes were recovered after the flight. In three cases the sondes were again successfully launched. This demonstrates that a reused sonde measures as reliable as a new one.

The hard- and software of the novel sonde is realised in a modular way. Therefore, further optimisation and adaptation of the system to accommodate special requirements or measurements purposes is possible. For example, the approximation of parameters, which are necessary for the retrieval algorithm (e.g. Rayleigh scattering or extraterrestrial radiation) can easily be replaced.

With the actual configuration of the sonde, the retrieval of reliable ozone profiles under different measurement conditions is possible.

The optical characteristics of the sonde can further be optimised using new or additional hardware components. For example, the spectrometer can be equipped with another grating type, thus providing a different wavelength range and/or a different spectral resolution. An additional collecting lens in the optical path of the spectrometer would focus the tall slit image onto the shorter CCD detector array, which would improve the light-collection efficiency. This may result in an improved signal to noise ratio. Moreover, optical filters can be attached to the entrance optics to block undesirable parts of the solar spectrum.

The retrieved ozone profiles of the test flights performed in Hohenpeißenberg under low solar zenith angle conditions showed a good or even very good agreement with two independent comparison measurements (LIDAR and Brewer-Mast sondes) in the stratosphere. The discrepancies further decreased with longer integration times (250 ms) for the detection of the solar spectrum. In particular the ozone profiles in the altitude range between 15 and 20 km are significantly improved. The longer integration time improves the signal to noise ratio, thus resulting in a higher vertical resolution and better data quality. Further optimisation of the signal to noise ratio can be achieved by selecting an integration time, suitable for the most interesting wavelength range for the measurement purpose and depending on the solar zenith angle.

The measurements in the Arctic were performed at high solar zenith angles and with shorter integration times. This combination results in a lower signal to noise ratio. Thus, under these conditions the irradiance measurements in the UV range are less accurate. Nevertheless, the calculated ozone profiles still show a reliable agreement with the ozone profiles obtained with electrochemical sondes for altitudes above 20 km.

The measured data set can also be used to extract a quality criterion. By determining the maximal vertical resolution of the measured ozone profile, an evaluation of the reliability of the profile is possible. This makes the data evaluation independent from the comparison with other measurement systems.

The retrieval of the ozone profiles is based on an adapted method, normally used for the analysis of Dobson spectrometer data sets. It was calculated with two different wavelength pair combinations. The resulting profiles demonstrated that in higher altitudes the shorter wavelength combination and in lower altitudes the longer wavelength combination is more suitable. For further optimisation the ozone retrieval can be based on a higher number of wavelength pair combinations. The best fitting wavelength for each altitude region can be selected using the vertical resolution criterion. This may lead to a more precise ozone profile for an extended altitude region.

For one flight the measured spectra in the visible wavelength range were analysed. Absorption structures due to NO_2 were identified by a comparison of measured spectra in 35 and 15 km altitudes. This demonstrates the capability of the new sonde to detect further trace gases besides ozone.
In order to retrieve the concentration profile of NO_2 and other trace gases (e.g. BrO) an algorithm has to be developed for trace gases showing a weaker absorption than ozone. Such an analysis might demonstrate that a subsequent optimisation of the instrument is necessary.

The current ozone profile retrieval is based on the analysis of four separate wavelengths and does not use the abundance of spectral information offered by the PIOS instrument. By applying another algorithm for the calculation of vertical trace gas columns, which considers all detected wavelengths, an even better ozone profile quality is expected. Furthermore, the possibility to retrieve the abundances of other trace gases by simultaneously analysing their absorption structures within the wavelength range is very likely. For example, the Differential Optical Absorption Spectroscopy is a common method to derive the column amounts of different absorbers using solar spectral measurements (PLATT 1994). Finally, the analysis of the measured solar spectra can be coupled to a full radiation transfer model (RTM). This would allow for an inversion algorithm to retrieve the trace gas concentration profiles. The RTM could be used as the forward model, which calculates irradiance spectra in different altitudes, considering different trace gas- and aerosol concentration profiles. The optimised trace gas profiles are obtained from the measured irradiance spectra with an optimal estimation formalism (RODGERS 2000). The optimal estimation method allows additionally to consider the uncertainties of the experimental setup like the spectral resolution of the spectrometer, the error caused by measurement noise, or by the used approximations for scattering. The resulting possible precision of the obtained profiles can be estimated and would offer a more independent evaluation of the instrument‘s vertical resolution.

The low weight and low power consumption of the sonde and especially the modular design allows the adaptation on board of other measurement platforms.
For example, rocket-borne measurements with the PIOS sensor would allow for trace gas profile measurements up to the upper stratosphere and lower mesosphere region. Furthermore the direct measurement of the extraterrestrial radiation I_0 would be possible and would offer a reference spectrum for all further measurements with the optical sensor, thus improving the trace gas retrieval algorithm.
Also the adaption for an unmanned air vehicle (UAV) is possible. In contrast to balloon-borne measurements, the UAV can be controlled during the flight.

Measurements at exactly determined positions are possible. Accordingly, the flight pattern can be adapted to the requirements. For example, exactly the same profile can be measured several times or spatial variations can be detected. Furthermore, the same PIOS instrument can be used for several missions, thus saving costs.

Bibliography

Anderson, J., W. Burne, M. Proffitt, 1989: Ozone destruction by chlorine radicals within the Antarctic vortex: The spatial and temporal evolution of ClO-O3 anticorrelation based on in situ ER-2 data. — *Journal of Geophysical Research*, **94**, 11465–11479.

Barnes, R. A., P. G. Simeth, 1986: Design of a rocket-borne radiometer for stratospheric ozone measurements. — *Rev. Sci. Instrum.*, **57, 4**, 544–551.

Basher, R. E., 1982: *Review of the Dobson spectrophotometer and its accuracy.* — Global Ozone Research and Monitoring Project, Report 13, WMO Global Ozone Research and Monitoring Project.

Bates, D., M. Nicolet, 1950: Atmospheric hydrogen. — *Publ. Astron.; Soc. Pac.*, **62**, 106–110.

Becker, E., J. Notholt, 2000: Intercomparison and validation of FTIR measurements with the Sun, the Moon and emission in the Arctic. — *Journal of Quantitative Spectroscopy and Radiative Transfer*, **65, 5**, 779–786.

Bernhard, G., G. Seckmeyer, 1997: Technical note: New entrance optics for solar spectral UV measurements. — *Photochemistry and Photobiology*, **65, 6**, 923–930.

Bertaux, J., A. Hauchecorne, et al., **2004:** First results on GOMOS/ENVISAT. — *Adv. Space Res.*, **33**, 1029–1035.

Bethan, S., G. Vaughan, S. Reid, 1996: A comparison of ozone and thermal tropopause heights and the impact of tropopause definition on quantifying the ozone content of the troposphere. — *Quaterly Journal of the Royal Meteorological Society*, **122**, 929–944.

Bovensmann, H., J. P. Burrows, M. Buchwitz, J. Frerick, S. Noel, V. V. Rozanov, K. V. Chance, A. P. H. Goede, 1999: SCIAMACHY: Mission objectives and measurement modes. — *Journal of the Atmospheric Sciences*, **56, 2**, 127–150.

Brasseur, G., S. Solomon, 1986: *Aeronomy of the middle atmosphere.* — Atmospheric science library, Reidel D., Dordrecht, second Ed.

Brewer, A., 1949: Evidence for a world circulation provided by the measurements of helium and water vapour distribution in the stratosphere. — *Quaterly Journal of the Royal Meteorological Society*, **75**, 351–363.

Bucholtz, A., 1995: Rayleigh-scattering calculations for the terrestrial atmosphere. — *Applied Optics*, **34, 15**, 2765–2773.

Burkholder, J. B., K. Talukdar, Ranajit, 1994: Temperature Dependence of the Ozone Absorption Spectrum over the Wavelength Range 410 to 760 nm. — *Geophysical Research Letters*, **21, 7**, 581–584.

Carslaw, K., T. Peter, S. Clegg, 1997: Modeling the composition of liquid stratospheric aerosols. — *Reviews of Geophysics*, **35**, 125–154.

Chance, K. V., R. J. D. Spurr, 1997: Ring effect studies: Rayleigh scattering, including molecular parameters for rotational Raman scattering, and the Fraunhofer spectrum. — *Applied Optics*, **36, 21**, 5224–5230.

Chapman, S., 1930: A theory of upper atmospheric ozone. — *Mem. R. Soc.*, **3**, 103–125.

Chubachi, S., 1984: Preliminary result of ozone observations at Syowa Station from February, 1982 to January, 1983. — *Mem. Natl Inst. Polar Res.*, **34**, 13–20.

Claude, H., R. Hartmannsgruber, U. Köhler, 1987: *Measurement of atmospheric ozone profiles using the Brewer-Mast sonde.* — Global Ozone Research and Monitoring Project, Report 17, World Meteorological Organisation.

Crutzen, P. J., 1970: The influence of nitrogen oxide on the atmospheric ozone content. — *Quaterny Journal of the Royal Meteorological Society*, **96**, 320–327.

Dameris, M., 2005: Klima-Chemie-Wechselwirkung und der stratosphärische Ozonabbau. — *promet*, **31, 1**, 2–11.

De Zafra, R., M. Jaramillo, A. Parrish, P. Solomon, B. Connor, J. Barrett, 1987: High concentrations of chlorine monoxide at low altitudes in the Antarctic spring stratosphere: diurnal variation. — *Nature*, **328, 6129**, 408–411.

Dessler, A., 2000: *The chemistry and physics of stratospheric ozone*, Vol. 74 of *International geophysics series.* — Academic Press.

Dobson, G., 1931: A photoelectric spectrometer for measuring the amount of atmospheric ozone. — *Proc. Phys. Soc. Lond.*, **43**, 324–339.

Dobson, G., 1956: Origin and distribution of the polyatomic molecules in the atmosphere. — *Proc. R. Soc. Lond.*, **A236**, 187–193.

Dobson, G., 1957: Observers handbook for the ozone spectrophotometer. — *Annals of the International Geophysical Year*, **V, Part 1**, 46–89.

European Commission, 2003: *Ozone - climate interactions.* — Air pollution research report 81, European Commission.

Farman, J., C. Toon, P. Shaper, J. Blavier, L. Lowes, 1985: Large losses of total ozone in Antarctica reveal seasonal ClOx/NOx interaction. — *Nature*, **315**, 207–210.

Ferlemann, F., N. Bauer, et al., **2000:** Differential optical absorption spectroscopy instrument for stratospheric balloonborne trace-gas studies. — *Applied Optics*, **39, 15**, 2377–2386.

Fioletov, V. E., 2004: Total ozone variations over midlatitudes and on the global scale. — In: *XX Quadrennial Ozone Symposium, 1.-8. June 2004*, C. S. Zerefos, Ed., International Ozone Commission, Kos, Greece, Vol. I, 25–26.

Fioletov, V. E., G. E. Bodeker, A. J. Miller, R. D. McPeters, R. Stolarski, 2002: Global and zonal total ozone variations estimated from ground-based and satellite measurements: 1964-2000. — *Journal of Geophysical Research*, **107, D22**, doi:10.1029/2001JD001350.

Gleason, J., P. Bhartia, et al., **1993:** Record low global ozone in 1992. — *Science*, **260, 5107**, 523–X8.

Hanson, D., A. Ravishankara, E. Lovejoy, 1996: Reactions of $BrONO_2$ and H_2O on submicron sulfuric acid aeorosol and the implications for the lower stratosphere. — *Journal of Geophysical Research*, **101**, 9063–9069.

Harwood, M., R. L. Jones, 1994: Temperature dependent ultraviolet-visible absorption cross sections of NO_2 and N_2O_4: Low-temperature measurments of the equilibrium constant for $2\ NO_2 \rightleftharpoons N_2O_4$. — *Journal of Geophysical Research*, **99, D11**, 22955–22964.

Hassol, S., 2004: *Impacts of Warming Arctic.* — Cambridge University Press, deutsche ausgabe Ed.

Holland, A. C., R. A. Barnes, H. Lee, 1985: Improved rocket ozonesonde (ROCOZ-A). 1: Demonstration of precision. — *Applied Optics*, **24, 19**, 3286–3295.

Holton, J., P. Haynes, M. McIntyre, A. Douglass, R. Rood, L. Pfister, 1995: Stratosphere-troposphere exchange. — *Reviews of Geophysics*, **33, 4**, 403–439.

Huber, M., M. Blumthaler, W. Ambach, 1993: A method for determining the wavelength shift for measurements of solar UV-radiation. — *SPIE - Atmospheric Radiation*, **2049**, 354–357.

Van de Hulst, H., 1957: *Light scattering by small particles.* — Wiley, New York.

IPCC, 2001: *Climate Change 2001, The Scientific Basis.* — Third assessment report, International Panel of Climate Change.

Jacob, D., 1999: *Introduction to Atmospheric Chemistry.* — Princeton University Press.

Junge, C., C. Changnon, J. Manson, 1961: Stratospheric aerosols. — *J. Meteorol.*, **18**, 81–108.

Kasten, F., A. T. Young, 1989: Revised optical air mass tables and approximation formula. — *Applied Optics*, **28, 22**, 4735–4738.

Keim, E., 1996: Observations of large reductions in the NO/NOx ratio near the mid-latitude tropopause and the role of heterogeneous chemistry. — *Geophysical Research Letters*, **23**, 3223–3226.

Kidder, Q., Stanley, H. Vonder Haar, Thomas, 1995: *Satellite Meteorology, an introduction.* — Academic Press.

Kobayashi, J., Y. Toyama, 1966: On Various Methods of Measuring the Vertical Distribution of Atmospheric Ozone (III). — *Papers in Meteorology and Geophysics*, **17, 2**, 113–125.

Komhyr, W., R. Barnes, G. Brothers, J. Lathrop, D. Opperman, 1995: Electrochemical concentration cell ozonesonde performance evaluation during STOIC 1989. — *Journal of Geophysical Research*, **100, D 05**, 9231–9244.

Komhyr, W. D., 1969: Electrochemical concentration cells for gas analysis. — *Ann. Geophysicae*, **25**, 203–210.

Komhyr, W. D., 1980: *Operations handbook - Ozone observations with a Dobson spectrophotometer.* — Global Ozone Research and Monitoring Project, Report 6, WMO.

Kurucz, R., 1984: *Solar Flux Atlas from 296 to 1300 nm, Sunspot, New Mexico.* — Report, National Solar Observatory.

Labitzke, K., 1999: *Die Stratosphäre: Phänomene, Geschichte, Relevanz.* — Springer-Verlag.

Langer, J., 1999: *Measurements of Arctic stratospheric ozone: Comparison of ozone-measurements at Ny-Aalesund, Spitsbergen, in 1997 and 1998.* — PhD-thesis, Reports on Polar Research 322, Alfred-Wegener-Institute for Polar and Marine Research.

Logan, J., 1999: Trends in the vertical distribution of ozone: A comparison of two analyses of ozone sonde data. — *Journal of Geophysical Research*, **104**, 26373–26399.

Malicet, J., D. Daumont, J. Charbonnier, C. Parisse, A. Chakir, I. Brion, 1995: Ozone UV spectroscopy. II. Absorption cross-sections and temperature dependence. — *Journal of Atmospheric Chemistry*, **21**, 263–273.

Mayer, B., A. Kylling, 2005: Technical note: The libRadtran software package for radiative transfer calculations - description and example for use. — *Atmospheric Chemistry and Physics Discussion*, **5**, 1319–1381.

Molina, L. T., M. J. Molina, 1987: Production of Cl2O2 from the self-reaction of the ClO radical. — *J. Phys. Chem.*, **91**, 433–436.

Molina, M. J., F. Rowland, 1974: Stratospheric sink for chlorofluoromethanes: chlorine atom catalyzed destruction. — *Nature*, **249**, 810–814.

Ocean Optics, 2003: *USB2000 Fiber Optic Spectrometer Operating Instructions.* — www.oceanoptics.com.

Okabayashi, M., 1999: *A study on balloon-borne optical sensors for ozone measurements in the upper stratosphere.* — Phd-thesis, Tohoku University.

Okano, S., M. Okabayashi, H. Gernandt, 1996: Observations of ozone profiles in the upper stratosphere using a UV sensor on board a light-weight high-altitude balloon. — *Memoirs of National Institute of Polar Research*, **51**, 225–231.

Oltmans, S., H. Vömel, D. Hofmann, K. Rosenlof, D. Kley, 1995: The increase of stratospheric water vapor from balloonborne, frospoint hygrometer measurements at Washington D.C., and Boulder, Colorado. — *Geophysical Research Letters*, **27**, 3453–3456.

Penndorf, R., 1957: Tables of refractive index for standard air and the Rayleigh scattering coefficient for the spectral region between 0.2 and 20.0 μm and their application to atmospheric optics. — *J. Opt. Soc. Am*, **47**, 176.

Perner, D., U. Platt, 1980: Absorption of light in the atmosphere by collision pairs of oxygen (O2)2. — *Geophysical Research Letters*, **7**, 1053–105?

Pitari, G., E. Mancini, V. Rizi, D. T. Shindell, 2002: Impact of Future Climate and Emission Changes on Stratospheric Aerosols and Ozone. — *Journal of the Atmospheric Sciences*, **59, 3**, 414–440.

Platt, U., 1994: Differential Optical Absorption Spectroscopy (DOAS). — In: *Monitoring by Spectroscopic Techniques*, M. Sigrist, Ed., John Wiley & Sons, Inc., New York, Vol. 127 of *Chemical Analysis Series*, 27–84.

Polyakov, A., Y. Timofeyev, D. Ionov, Y. Virolainen, H. Steele, M. J. Newchurch, 2005: Retrieval of ozone and nitrogen dioxide concentrations from Stratospheric Aerosol and Gas Experiment III (SAGE III) measurements using a new algorithm. — *Journal of Geophysical Research*, **110, D6**, doi:10.1029/2004JD005060.

Regener, E., V. H. Regener, 1934: Aufnahmen des ultravioletten Sonnenspektrums in der Stratosphre und vertikale Ozonverteilung. — *Physikalische Zeitschrift*, **35**, 788–793.

Reinsel, G. C., A. J. Miller, E. C. Weatherhead, E. Lawrence, R. M. Nagatani, G. C. Tiao, D. J. Wuebbels, 2005: Trend analysis of total ozone data for turnaround and dynamical contributions. — *Journal of Geophysical Research*, **110, D16306**, doi:10.1029/2004JD004662.

Rex, M., P. von der Gathen, et al., **1998:** In situ measurements of stratospheric ozone depletion rates in the Arctic winter 1991/1992: A Lagrangian approach. — *Journal of Geophysical Research*, **103, D5**, 5843–5853.

Rex, M., R. J. Salawitch, et al., **2002:** Chemical depletion of Arctic ozone in winter 1999/2000. — *Journal of Geophysical Research*, **107, D20**.

Rex, M., R. J. Salawitch, P. von der Gathen, N. Harris, M. P. Chipperfield, B. Naujokat, 2004: Arctic ozone loss and climate change. — *Geophysical Research Letters*, **31**, L04116, doi:10.129/2003GL018844.

Richner, H., S. von Hünerbein, 1999: *Grundlagen aerologischer Messungen speziell mittels der Schweizer Sonde SRS 400.* — Veröffentlichungen der SMA-Meteo Schweiz 61, SMA-Meteo Schweiz.

Rodgers, C., 2000: *Inverse methods for atmospheric sounding: theory and practise*, Vol. 2 of *Series on Atmospheric, Oceanic and Planetary Physics.* — World Scientific Publishing Co. Pte. Ltd.

Rohen, G., C. von Savigny, E. Llewellyn, J. Kaiser, K.-U. Eichmann, A. Bracher, H. Bovensmann, J. Burrows, 2005: First results of ozone profiles between 35 and 65 km retrieved from SCIAMACHY limb spectra and observations of ozone depletion during the solar proton events in Oct./Nov. 2003. — *Advances in Space Research*, accepted.

Rosenlof, K., S. Oltmans, D. Kley, J. Russell III, 2001: Stratospheric water vapour increases and the past half-century. — *Geophysical Research Letters*, **28**, 1195–1198.

Sander, S., R. Friedl, et al., **2003:** *Chemical kinetics and photochemical data for use in atmospheric studies.* — JPL Publication 02-25, Jet Propulsion Laboratory, NASA.

Schmidt, M., 1988: *Von Christian Friedrch Schönbein bis zum Ozonloch.* — Katlenburg-Lindau.

Schulz, A., M. Rex, et al., **2001:** Arctic ozone loss in treshold conditions: Match observations in 1997/1998 and 1998/1999. — *Journal of Geophysical Research*, **106, D7**, 7495–7503.

SCOUT project office, 2005: Low temperatures in the Arctic stratosphere have led to severe ozone loss during the spring in 2005. — *the eggs (www.the-eggs.org)*, **12**, European Geophysical Union.

Seinfeld, J., S. N. Pandis, 1998: *Atmospheric chemistry and physics.* — John Wiley and Sons, Inc.

Singh, O. N., P. Fabian, 2003: *Atmospheric ozone: a millenium issue*, Vol. 1 of *Special publication series.* — European geosciences union.

Sioris, C., C. Haley, et al., **2003:** Stratospheric profiles of nitrogen dioxide observed by optical spectrograph and infrared imager system on the Odin satellite. — *Journal of Geophysical Research*, **108, D7**, 4215.

Solomon, S., 1999: Stratospheric ozone depletion: A review of concepts and history. — *Reviews of Geophysics*, **37, 3**, 275–316.

Solomon, S., 2004: The hole truth. — *Nature*, **427**, 289–291.

Steinbrecht, W., H. Claude, U. Köhler, K. Hoinka, 1998: Correlations between tropopause height and total ozone: Implications for longterm changes. — *Journal of Geophysical Research*, **103**, 19183–19192.

Stenke, A., V. Grewe, 2005: Simulation of stratospheric water vapor trends: impact on stratospheric ozone chemistry. — *Atmospheric Chemistry and Physics*, **5**, 1257–1272.

Stolarski, R., A. Krueger, M. Schoeberl, R. D. McPeters, P. Newman, J. Alpert, 1986: Nimbus 7 satellite measurements of the springtime Antarctic ozone decrease. — *Nature*, **322**, 808–811.

Tuck, A., M. Proffitt, 1997: Comments on the magnitude of transport out of the Antarctic polar vortex by W.M.F. Wauben. — *Journal of Geophysical Research*, **102**, 28215–28218.

Wahl, P., 2002: *Observation and Characterization of laminated ozone structures in the polar stratosphere.* — PhD thesis, Reports on Polar and Marine Research 411, Alfred Wegener Institute for Polar and Marine Research.

Wamsley, P., J. Elkins, et al., **1998:** Distribution of halon-1211 in the upper troposphere and lower stratosphere and the 1994 total bromine budget. — *Journal of Geophysical Research*, **103**, 1513–1526.

Wauben, W. M. F., R. Bintanja, P. van Velthoven, H. Kelder, 1997: On the magnitude of the transport out of the Antarctic polar vortex. — *Journal of Geophysical Research*, **102, 1229-1238**.

Weatherhead, E. C., G. C. Reinsel, S. Bech Andersen, 2004: Methods and Results for Detecting Ozone Recovery. — In: *XX Quadrennial Ozone Symposium, 1.- 8. June 2004*, C. S. Zerefos, Ed., International Ozone Commission, Kos, Greece, Vol. I, 83–84.

Weidner, F., H. Bösch, et al., **2005:** Balloon-borne Limb profiling of UV/vis skylight radiances O3, NO2, and BrO: Technical set-up and validation of the method. — *Atmospheric Chemistry and Physics*, **5**, 1409–1422.

WMO, 1957: Meteorology - A three-dimensional science. — *WMO Bulletin*, **6**, 134–138.

WMO, 1986: *Atmospheric Ozone.* — WMO Report 16, World Meteorological Organisation.

WMO, 2003: *Scientific Assessment of Ozone Depletion 2002.* — Global Ozone Research and Monitoring Project, Report 44, World Meteorological Organisation, PomorOrdner.

Wolff, M., W. Ruhe, 2004: *Unbemannte Vorrichtung zur Erfassung von Messdaten in der Erdatmosphäre.* — Gebrauchsmuster 20 2004 005 530.9, Deutsches Patent- und Markenamt.

Wursteisen, P., 2003: The validation of the ENVISAT chemistry instruments by use of stratospheric balloons and aircraft. — In: *16th ESA Symposium on European Rocken and Balloon Programmes*, B. Warmbein, Ed., ESA, St. Gallen, Switzerland, Vol. SP-530, 407–413.

Zerefos, C., 2004: OZONE, Proceedings Quadrennial Ozone Symposium 2004. — Kos, Greece, Vol. I+II.

List of Figures

List of Tables

Symbols and Abbreviations

AMF	air mass factor
CFC	chloroflourocarbon
DOAS	differential optical absorption spectroscopy
ECC	electrochemical concentration cell
FTIR	Fourier-transform infrared spectrometer
GHG	greenhouse gas
GPS	global positioning system
$h = 6.6256 \cdot 10^{-34}$ Js	Planck's constant
I	irradiance
I_0	extraterrestrial irradiance
IPCC	Intergovernmental Panel on Climate Change
IR	infrared
λ	wavelength of a photon
LIDAR	light detection and ranging
MOHp	Meteorological Observatory Hohenpeißenberg
MOL	Meteorological Observatory Lindenberg
ν	frequency of a photon
NDSC	Network for the Detection of Stratospheric Change
OMI	ozone monitoring instrument
PSC	polar stratospheric cloud
RH	relative humidity
RTM	radiation transfer model
σ_{O_3}	absorption cross section for ozone
σ_{Ray}	Rayleigh scattering cross section
SC	slant column

SAGE	Stratospheric Aerosol and Gas Experiment
SCIAMACHY	Scanning Imaging Absorption Spectrometer for Atmospheric Chartography
STOIC	Stratospheric Ozone Intercomparison Campaign
SZA	solar zenith angle
τ	optical depth
TOMS	total ozone mapping spectrometer
UNEP	United Nations Environmental Programme
UV	ultraviolet
VC	vertical column
vis	visible
WMO	World Meteorological Organisation

Danksagung

Meinem Betreuer Prof. Dr. Otto Schrems am Alfred-Wegener-Institut für Polar- und Meeresforschung danke ich für die Bereitstellung des Themas und das Interesse mit dem er das Fortschreiten der Arbeit verfolgt hat.

Prof. Dr. John Burrows an der Universität Bremen bin ich sehr dankbar für die bereitwillige Übernahme des Koreferats und für die sehr inhaltsreiche und konstruktive Diskussion.

Herrn Dr. Andreas Herber danke ich für die durchgängige Begleitung der Arbeit und für die wohlwollende Unterstützung all meiner Ideen und Pläne.

Herrn Dr. Hartwig Gernandt und Prof. Dr. Shoichi Okano danke ich dafür, dass sie mich als Pioniere der deutsch-japanischen optischen Ozonsondenentwicklung schon vor 9 Jahren für die experimentelle Forschung begeistert haben und dafür, dass sie mir voller Vertrauen diese neue Sondenentwicklung überlassen haben.

Ich möchte mich stellvertretend bei Herrn Dr. Leiterer (MO Lindenberg) und Herrn Dr. Claude (MO Hohenpeißenberg) dafür bedanken, dass wir an ihren Observatorien so freundlich aufgenommen wurden und für die Unterstützung, die wir durch sie und ihre Mitarbeiter erfahren haben.

Ein herzlichen Dankeschön an Dr. Jens Kube, Thorsten Wilhelm und Konni Piel, die mich als Gast an der Koldewey-Station empfangen haben und die mit dafür gesorgt haben, dass ich mich schnell wieder wie zu Hause fühlte. Danke an die Gäste der Koldewey-Station, die sich im Sommer 2004 so bereitwillig zum Plastikballon-Start-Team zusammengefunden haben.

Dr. Christian von Savigny danke ich für seine Zeit und die sehr hilfreichen Diskussionen in den letzten Wochen dieser Arbeit.

Viele Anregung habe ich aus den interessanten Gesprächen mit Dr. Vladimir Rozanov, Dr. Markus Rex, Dr. Peter von der Gathen, Dr. Roland Neuber, Dr. Ralph Lehmann, Dr. Marion Maturilli, Dr. Renate Treffeisen, Hilke Oetjen, Folkard Wittrock und Dr. Astrid Schulz erhalten. Vielen Dank für Eure Gesprächsbereitschaft.

Ein riesiges Dankeschön an Dr. Hans Werner Jacobi für seine Fähigkeit immer irgendwie genau zu wissen, wie mir gerade am besten weiter zu helfen war und dafür, dass ich immer, wirklich immer mit einem herzlichen Lächeln empfangen wurde.

Vielen Dank fürs Korrekturlesen an Dr. Sigrid Wuttke, Dr. Jens Kube, Dr. Hans Werner Jacobi, Dr. Andreas Herber, Dr. Renate Treffeisen und Hans Jakob Engel.

Danke an Wilfried Ruhe und Ingo Beninga von impres, Heiko Lilienthal und Jan Hoops von isitec und Rolf Maag von Meteolabor ohne deren versammeltes Ingenieur Know-How diese Sonde sicher nicht fliegen gelernt hätte.
Ein ganz besonderer Dank gilt allen, die mich in den letzten 5 anstrengenden Wochen immer wieder aufgemuntert und ermutigt haben und mit viel Freundschaft, Tee, Sport und Schokolade meine Arbeitskraft erhalten haben. Danke Maren, Stephanie, Siggi, Jana, Lena, Sven, Achim, Jens, Astrid, Titti, Jockel, Stefan, Jan, noch ne Siggi, Willi, Hans Werner, Ingo, Tine, Tom, Merle, Michael, Hilke, Kirsten, Dorothee, Janina.
Meiner Familie gilt mein Dank dafür, dass sie immer noch mit ausgesprochenen Interesse meine Arbeit verfolgen, sich über kleine und große Erfolge freuen und bei kleinen und großen Problemen mitleiden und einfach dafür, dass es sie gibt.
Danke an Robert, der mich immer wieder mit großen Portionen Gelassenheit ausgerüstet und für ein ausgefülltes Leben neben der Doktorarbeit gesorgt hat.